



The SOFIA Massive (SOMA) Star Formation Survey. III. From Intermediate- to High-mass Protostars

Mengyao Liu¹ , Jonathan C. Tan^{1,2} , James M. De Buizer³, Yichen Zhang⁴ , Emily Moser⁵, Maria T. Beltrán⁶, Jan E. Staff⁷ , Kei E. I. Tanaka⁸ , Barbara Whitney⁹, Viviana Rosero¹⁰ , Yao-Lun Yang¹ , and Rubén Fedriani²

¹Dept. of Astronomy, University of Virginia, Charlottesville, Virginia 22904, USA

²Dept. of Space, Earth & Environment, Chalmers University of Technology, SE-41293 Gothenburg, Sweden

³SOFIA-USRA, NASA Ames Research Center, MS 232-12, Moffett Field, CA 94035, USA

⁴Star and Planet Formation Laboratory, RIKEN Cluster for Pioneering Research, Wako, Saitama 351-0198, Japan

⁵Dept. of Astronomy, Cornell University, Ithaca, NY 14853, USA

⁶INAF-Osservatorio Astrofisico di Arcetri, Largo E. Fermi 5, I-50125 Firenze, Italy

⁷College of Science and Math, University of Virgin Islands, St. Thomas, United States Virgin Islands 00802, USA

⁸ALMA Project, National Astronomical Observatory of Japan, Mitaka, Tokyo 181-8588, Japan

⁹Dept. of Astronomy, University of Wisconsin-Madison, 475 N. Charter St., Madison, WI 53706, USA

¹⁰National Radio Astronomy Observatory, 1003 Lópezville Rd., Socorro, NM 87801, USA

Received 2020 June 11; revised 2020 September 15; accepted 2020 September 15; published 2020 November 23

Abstract

We present $\sim 10\text{--}40\ \mu\text{m}$ SOFIA-FORCAST images of 14 intermediate-mass protostar candidates as part of the SOFIA Massive (SOMA) Star Formation Survey. We build spectral energy distributions, also using archival Spitzer, Herschel, and IRAS data. We then fit the spectral energy distributions with radiative transfer models of Zhang & Tan, based on turbulent core accretion theory, to estimate key protostellar properties. With the addition of these intermediate-mass sources, based on average properties derived from SED fitting, SOMA protostars span luminosities from $\sim 10^2$ to $10^6\ L_\odot$, current protostellar masses from ~ 0.5 to $35\ M_\odot$, and ambient clump mass surface densities, Σ_{cl} , from 0.1 to $3\ \text{g cm}^{-2}$. A wide range of evolutionary states of the individual protostars and of the protocluster environments is also probed. We have also considered about 50 protostars identified in infrared dark clouds that are expected to be at the earliest stages of their evolution. With this global sample, most of the evolutionary stages of high- and intermediate-mass protostars are probed. The best-fitting models show no evidence that a threshold value of the protocluster clump mass surface density is required to form protostars up to $\sim 25\ M_\odot$. However, to form more massive protostars, there is tentative evidence that Σ_{cl} needs to be $\gtrsim 1\ \text{g cm}^{-2}$. We discuss how this is consistent with expectations from core accretion models that include internal feedback from the forming massive star.

Unified Astronomy Thesaurus concepts: Massive stars (732); Star formation (1569); Interstellar medium (847); Jets (870); Infrared sources (793)

Supporting material: data behind figures, machine-readable tables

1. Introduction

Intermediate-mass (IM) protostars are important as representatives of the transition between the extremes of low-mass (i.e., $\lesssim 2\ M_\odot$) and high-mass (i.e., $\gtrsim 8\ M_\odot$) star formation. These objects are relatively rare compared to their low-mass counterparts and tend to be located at greater distances. They are precursors of Herbig Ae and Be stars. The immediate environments of IM protostars can appear to be quite complex, with extended emission often resolved into multiple sources when observed at high resolution (e.g., G173.58+2.45, Shepherd & Watson 2002). However, there are also examples with relatively simpler, more isolated morphologies (e.g., Cep E, Moro-Martín et al. 2001). Observations of IM protostars indicate that they share some physical properties with low-mass protostars, such as circumstellar disks (e.g., Zapata et al. 2007; Sánchez-Monge et al. 2010; van Kempen et al. 2012; Takahashi et al. 2012) and collimated molecular outflows (e.g., Gueth et al. 2001; Beltrán et al. 2008, 2009; Palau et al. 2010; Velusamy et al. 2011), but collimated molecular outflows are more powerful when driven by IM protostars. Furthermore, IM protostars also share many characteristics with their higher mass counterparts, such as correlations between the outflow kinematics and the properties of their driving sources (e.g., Cabrit & Bertout 1992; Bontemps et al. 1996; Wu et al. 2004; Hatchell et al. 2007;

Beltrán et al. 2008), and hot core chemistry (e.g., Fuente et al. 2005; Neri et al. 2007; Sánchez-Monge et al. 2010). Thus, observational evidence suggests that IM protostars form in a similar way as low-mass protostars, and this formation mechanism is also shared with at least early B-type or late O-type protostars (Beltrán 2015).

In this paper, we study a sample of 14 IM protostars selected from the SOFIA Massive (SOMA) Star Formation Survey (PI: Tan), which aims to characterize a sample of $\gtrsim 50$ high- and IM protostars over a range of evolutionary stages and environments with their ~ 10 to $40\ \mu\text{m}$ images observed with the SOFIA-Faint Object infraRed CAmera for the SOFIA Telescope (FORCAST) instrument. In Paper I of the survey (De Buizer et al. 2017), the first eight sources were presented, which were mostly massive protostars. In Paper II (Liu et al. 2019), seven especially luminous sources were presented, corresponding to some of the most massive protostars in the survey. The IM sample presented here consists of seven new target regions in which 12 protostars have been studied plus 2 additional protostars that were extracted as secondary sources from the target regions in Papers I and II. It thus serves to extend the luminosity and mass range of the survey sample down to lower values.

Our approach is to follow the same methods as we developed in Papers I and II to build the spectral energy distributions

Table 1
SOFIA FORCAST Observations: Observation Dates and Exposure Times (seconds)

Source	R.A.(J2000)	Decl.(J2000)	d (kpc)	Obs. Date	7.7 μm	19.7 μm	31.5 μm	37.1 μm
Sh 2-235	05 ^h 40 ^m 52. ^s 4	+35°41'30"	1.8	2016 Sep 20	404	779	642	1504
IRAS 22198+6336	22 ^h 21 ^m 26. ^s 68	+63°51'38".2	0.764	2015 Jun 05	278	701	482	743
NGC 2071	05 ^h 47 ^m 04. ^s 741	+00°21'42".96	0.39	2018 Sep 08	492	1319	825	2020
Cepheus E	23 ^h 03 ^m 12. ^s 8	+61°42'26"	0.73	2015 Nov 04	281	899	818	281
LDN 1206	22 ^h 28 ^m 51. ^s 41	+64°13'41".1	0.776	2015 Nov 20	116	308	162	630
IRAS 22172+5549	22 ^h 19 ^m 09. ^s 478	+56°05'00".370	2.4	2015 Jun 03	337	664	386	466
IRAS 21391+5802	21 ^h 40 ^m 41. ^s 90	+58°16'12".3	0.75	2015 Nov 06	334	806	488	1512

Note. The source positions listed here are the same as the positions of the black crosses denoting the radio continuum peak (millimeter continuum peak in Cep E and L1206 A, and MIR peak in IRAS22172 MIR2) in each source in Figures 1–7. Source distances are from the literature, as discussed below.

(SEDs) of the sources. As before, we then fit these SEDs with the Zhang & Tan (2018, hereafter ZT18) protostellar radiative transfer (RT) models to estimate intrinsic source properties. In this way, all the protostars are analyzed in a uniform way. Finally, we search for trends in the source properties in the entire SOMA sample of 29 sources that have been analyzed so far in Papers I, II, and III.

The observations and data used in this paper are described in Section 2. The analysis methods are summarized in Section 3. We present the mid-infrared (MIR) imaging and SED fitting results in Section 4 and discuss these results and their implications in Section 5. A summary is given in Section 6.

2. Observations

The following seven target regions were observed by SOFIA¹¹ (Young et al. 2012) with the FORCAST instrument (Herter et al. 2013; see Table 1): Sh 2-235 (hereafter S235), IRAS 22198+6336, NGC 2071, Cepheus E (hereafter, Cep E), L1206 (A and B), IRAS 22172+5549 (MIR 1, MIR 2, and MIR 3), and IRAS 21391+5802 (BIMA 2, BIMA 3, and MIR 48). The angular resolutions of the SOFIA–FORCAST images are 2.7'' at 7 μm , 2.9'' at 11 μm , 3.3'' at 19 μm , 3.4'' at 31 μm , and 3.5'' at 37 μm . We also fit the SEDs of two more sources, G305.20+0.21 A (hereafter, G305 A) and IRAS 16562-3959 N (hereafter, IRAS 16562 N), which are secondary sources near primary targets of Paper II. Thus a total of 14 protostars will be analyzed here for the first time as SOMA Survey sources.

In addition to SOFIA observations, for all objects, we also retrieve publicly available images of Spitzer/IRAC (Fazio et al. 2004) at 3.6, 4.5, 5.8 and 8.0 μm from the Spitzer Heritage Archive, Herschel/PACS, and SPIRE (Griffin et al. 2010) at 70, 160, 250, 350 and 500 μm from the Herschel Science Archive, and Higher Resolution IRAS Images (HIRES¹²; Neugebauer et al. 1984) at 60, 100 μm from the NASA/IPAC Infrared Science Archive.

The calibration and astrometry methods are the same as in Paper II, except that for Cep E and IRAS 21391 we use the SOFIA 19 μm image instead of the 7 μm image to calibrate the other SOFIA images and the Herschel images given the high noise level in their 7 μm images. For SOFIA observations the calibration error is estimated to be in the range $\sim 3\%$ – 7% . The astrometric precision is about 0.1'' for the SOFIA 7 μm image, 0.4'' for longer wavelength SOFIA images, and 1'' for Herschel images. Note that

we use HIRES results of the IRAS data to achieve a resolution of $\sim 1'$. The astrometric precision is about 20–30''. Fluxes measured from HIRES agree with those of the Point Source Catalog (PSC2) to within 20%, and ringing (a ring of lower level flux may appear around a point source) can contribute another 10% uncertainty at most in the measurement of the background-subtracted flux of the source. Thus the total uncertainty, summed in quadrature, is 23%. Near-infrared (NIR) images from the Wide Field Camera (WFC)/UKIRT InfraRed Deep Sky Survey (UKIDSS; Lawrence et al. 2007) surveys and the Two Micron All Sky Survey (2MASS) Atlas images (Skrutskie et al. 2006) are also used to investigate the environments of the protostellar sources and search for association with the MIR counterparts.

3. Methods

We follow the methods described in Papers I and II to construct the SEDs (see Section 3 of Papers I and II for a more detailed discussion). In summary, fixed circular-aperture background-subtracted photometry is estimated from MIR to far-infrared (FIR) wavelengths for the sources. The aperture radius is chosen with reference to the 70 μm Herschel-PACS source morphology, when available (else the 37 μm SOFIA–FORCAST source morphology), with the goal of enclosing the majority of the flux while avoiding contamination from surrounding sources.

We also follow the methods of Papers I and II to fit the SEDs with ZT18 protostellar RT models. For IRAS 22198, NGC 2071, Cep E, G305 A, and IRAS 16562 N, which have Herschel data, we do not use IRAS data for the SED fitting. For L1206, our SOFIA images show that L1206 A is much brighter than L1206 B at long wavelengths: e.g., at 37 μm L1206 A contributes 96% of the total flux. Thus we assume that L1206 A is the main source at wavelengths longer than 37 μm and use the IRAS flux densities at 60 μm and 100 μm as a normal data point for the SED fitting of L1206 A and upper limits for the SED fitting of L1206 B. For the other sources, IRAS data are used as upper limits given its resolution and aperture size.

There are a few special cases for the SED fitting. For G305 A, there is hardly any emission at wavelengths shorter than 8 μm , and the local noise leads to a negative flux measurement at 7 μm . Thus we use the non-background-subtracted fluxes as upper limits at 3.6, 4.5, 5.8, and 8.0 μm . In the IRAS 16562 region, the flux densities at wavelengths longer than 250 μm are dominated by the main source in Paper II, thus the background-subtracted flux for IRAS 16562 N is negative at these wavelengths because of the contamination of the main source. Thus we use the non-background-subtracted fluxes as upper limits at 250, 350, and 500 μm .

¹¹ SOFIA is jointly operated by the Universities Space Research Association, Inc. (USRA), under NASA contract NAS2-97001, and the Deutsches SOFIA Institute (DSI) under DLR contract 50 OK 0901 to the University of Stuttgart.

¹² <https://irsa.ipac.caltech.edu/applications/Hires/>

4. Results

Table 2 lists the types of multiwavelength data available for each source, the flux densities derived, and the aperture sizes adopted. $F_{\lambda, \text{fix}}$ is the flux density derived with a fixed aperture size, and $F_{\lambda, \text{var}}$ is the flux density derived with a variable aperture size. The value of the flux density listed in the upper row of each source is derived with background subtraction, while the flux density derived without background subtraction is listed in parentheses in the lower row. The SOFIA images for each source are presented in Section 4.1. General results of the SOFIA imaging are summarized in Section 4.2. The SEDs and fitting results are presented in Section 4.3.

4.1. Description of Individual Sources.

4.1.1. S235

Estimates of the distance to the S235 A-B region vary from 1.6–2.5 kpc (e.g., Israel & Felli 1978; Burns et al. 2015). We adopt 1.8 kpc, following Evans & Blair (1981), Dewangan et al. (2016), and Shimoikura et al. (2016). High-resolution millimeter (mm) line and continuum and radio continuum observations toward S235 A-B were reported by Felli et al. (2004, 2006). Shimoikura et al. (2016) carried out observations of the C^{18}O emission toward S235 A-B and revealed that the clump has an elliptical shape, with a mass of $\sim 1000 M_{\odot}$ and an average radius of ~ 0.5 pc. Two compact HII regions, called S235 A and S235 B (e.g., Felli et al. 1997; Klein et al. 2005; Saito et al. 2007), are located in this clump, along with a mm continuum core with $\text{HCO}^+(1-0)$ outflows in between, which is thought to be an embedded earlier-stage YSO (Felli et al. 2004). The mm core has an MIR counterpart, S235 AB-MIR, and several water masers and methanol masers are located nearby (Kurtz et al. 2004). From their estimate of a luminosity of $\sim 10^3 L_{\odot}$ of the source, Felli et al. (2004) suggested that S235 AB-MIR is an IM young stellar object (YSO) driving the molecular outflows and supplying the energy for the -60 km s^{-1} water maser nearby. On the other hand, Dewangan & Anandarao (2011) concluded from SED fitting that S235 AB-MIR is the most massive protostar in the region with $m_{*} \sim 11 M_{\odot}$ and is still actively accreting, and so it is not yet able to excite an HII region. However, they were cautious about the reliability of these results due to the limited number of data points (three in the MIR from IRAC bands and two in the submm continuum from Felli et al. 2004).

Another NIR K-band source with the highest infrared excess, M1, is reported to be associated with the radio source VLA-1 by Felli et al. (2006), and the authors suggested that it could be a B2-B3 star with an UCHII region, while Dewangan & Anandarao (2011) suggested that it is a low-mass star, relatively young in its evolution. Both S235 AB-MIR (counterpart of the 1.2 mm core) and M1 can be seen in our SOFIA images in Figure 1. However, due to their weak MIR emission, we do not focus on them in this paper.

Our analysis is focused on the MIR source S235 B, which is associated with the radio source VLA-2 (Felli et al. 2006). S235 B is the brightest object in the S235 A-B cluster in all broadbands from U to K, and thus may be a massive YSO (Boley et al. 2009). Krassner et al. (1982) detected hydrogen recombination lines and polycyclic aromatic hydrocarbon (PAH) emission features at 3.3, 8.7, and $11.3 \mu\text{m}$. However, no 3.3 mm or 1.2 mm continuum or molecular lines are detected associated with S235 B (Felli et al. 2004). While there

is large-scale ^{12}CO , ^{13}CO , and C^{18}O emission in the whole S235 region (Shimoikura et al. 2016; Dewangan & Ojha 2017), smaller scale outflows specifically associated with S235 B have not yet been reported. For example, even in the high-resolution $\text{HCO}^+(1-0)$ map of Felli et al. (2004), whose field of view covers S235 B, there is no sign of $\text{HCO}^+(1-0)$ outflows emerging from S235 B. Boley et al. (2009) classified the central star of S235 B as an early-type (B1V) Herbig Be star surrounded by an accretion disk based on its spectrum from 3800–7200 Å, its location in a region of active star formation, the presence of the nearby nebulosity, the Balmer emission lines in the stellar spectrum, and the high H-K excess. Furthermore, its spectrum shows that the S235 B nebulosity is reflective in nature, with the central YSO in S235 B as the illuminating source. Given the mass inferred from the spectral type ($> 10 M_{\odot}$), Boley et al. suggested that S235 B is likely to already be on the main sequence.

In our SOFIA images as shown in Figure 1, S235 B is much brighter than S235 AB-MIR and M1. The weak second component to the north of the radio source in the Spitzer 8 μm image is likely to be produced by a ghosting effect of the primary source because it is not seen in the other IRAC images, the SOFIA images, or the UKIDSS *JHK* band images.

4.1.2. IRAS 22198+6336

IRAS 22198+6336 was previously considered to be a massive YSO (Palla et al. 1991; Molinari et al. 1996; Sánchez-Monge et al. 2008) until an accurate distance of 764 ± 27 pc was derived from the parallax measurements of 22 GHz associated water masers (Hirota et al. 2008). Hirota et al. reanalyzed the protostellar SED and then proposed that IRAS 22198+6336 might be an IM deeply embedded YSO with a spectral type of late-B, equivalent to a Class 0 object in low-mass star formation. Sánchez-Monge et al. (2010) detected a compact source at 3.5, 2.7, and 1.3 mm coincident with the centimeter source reported by Sánchez-Monge et al. (2008) and surrounded by a faint structure extended toward the southwest. The high rotational temperature (100–150 K) derived from CH_3CN and CH_3OH , together with the chemically rich spectrum, is clear evidence that IRAS 22198 is an IM hot core. The $\text{CO}(1-0)$ emission in Sánchez-Monge et al. (2010) reveals an outflow with a quadrupolar morphology clearly centered on the position of the main dust condensation. Observations of the high-velocity emission of different outflow tracers $\text{HCO}^+(1-0)$, $\text{HCN}(1-0)$ and $\text{SiO}(2-1)$ seem to favor the superposition of two bipolar outflows. Higher angular resolution observations at 1.3 mm by Palau et al. (2013) reveal a counterpart of the centimeter (cm) source (MM2 in their nomenclature) and a faint extension to its south (MM2-S). Palau et al. suggest that MM2 is likely driving the southwest-northeast outflow, while an unresolved close companion of MM2 or MM2-S, which is only detected at $3.6 \mu\text{m}$, could be the driving source of the northwest-southeast outflow. Periodic flares of the 6.7-GHz methanol maser have been detected in IRAS 22198, and their characteristics can be explained by a colliding-wind binary model (Fujisawa et al. 2014).

Our SOFIA images (see Figure 2) reveal the MIR counterpart of the cm/mm source. Extended emission is seen toward the blueshifted outflow in the southwest at 19 and $31 \mu\text{m}$. In contrast, the extended emission at μm directly points to the south. Faint extended emission is also seen along the axes of the two outflows at $70 \mu\text{m}$.

Table 2
Integrated Flux Densities

Facility	λ (μm)	$F_{\lambda, \text{fix}}^a$ (Jy)	$F_{\lambda, \text{var}}^b$ (Jy)	R_{ap}^c ($''$)	$F_{\lambda, \text{fix}}^d$ (Jy)	$F_{\lambda, \text{var}}^e$ (Jy)	R_{ap}^f ($''$)	$F_{\lambda, \text{fix}}^g$ (Jy)	$F_{\lambda, \text{var}}^h$ (Jy)	R_{ap}^i ($''$)	$F_{\lambda, \text{fix}}^j$ (Jy)	$F_{\lambda, \text{var}}^k$ (Jy)	R_{ap}^l ($''$)
Spitzer/IRAC	3.6	0.50 (0.54)	S225 (0.51)	9.0	0.05 (0.08)	0.01 (0.01)	6.6	0.34 (0.38)	0.12 (0.14)	NGC2071	0.05 (0.06)	0.11 (0.12)	12.0
Spitzer/IRAC	4.5	0.46 (0.51)	0.44 (0.47)	9.0	0.13 (0.15)	0.03 (0.04)	4.8	1.24 (1.32)	0.54 (0.63)	Cap E	0.17 (0.18)	0.25 (0.27)	12.0
Spitzer/IRAC	5.8	1.99 (2.24)	1.90 (2.06)	9.0	0.20 (0.43)	0.08 (0.10)	5.4	2.54 (2.78)	1.59 (1.71)		0.23 (0.31)	0.27 (0.38)	12.0
SOFIA/FORCAST	7.7	6.39 (6.24)	6.22 (6.13)	9.0	0.85 (1.41)	0.20 (0.29)	5.4	5.58 (5.53)	4.04 (4.32)		0.17 (0.19)	0.23 (0.20)	4.6
Spitzer/IRAC	8.0	6.12 (6.76)	5.83 (6.25)	9.0	0.23 (0.84)	0.15 (0.20)	6.6	6.08 (6.48)	4.09 (4.34)		0.31 (0.56)	0.34 (0.70)	12.0
SOFIA/FORCAST	19.7	33.66 (34.25)	32.64 (33.28)	9.0	10.35 (15.13)	5.40 (6.17)	7.0	86.65 (86.97)	63.79 (66.50)		1.41 (1.43)	1.69 (1.56)	6.2
SOFIA/FORCAST	31.5	70.87 (72.92)	70.87 (72.92)	12.0	91.08 (90.51)	77.83 (80.47)	9.2	310 (318)	169 (190)		20.50 (21.61)	16.73 (17.47)	7.7
SOFIA/FORCAST	37.1	84.95 (88.39)	84.95 (88.39)	12.0	132 (130)	111 (115)	9.2	375 (382)	176 (205)		23.56 (25.40)	23.56 (24.02)	9.0
IRAS	60.0	...	2281 (2386)	186.6	...	224 (235)	109.2	...	1146 (1213)		66.13 (63.58)	432 (445)	125.2
Herschel/PACS	70.0	449 (471)	449 (471)	25.6	694 (753)	694 (753)		99 (103)	99 (947)	23.0
IRAS	100.0	...	2897 (3255)	244.5	...	525 (666)	180.0	...	2559 (2879)		152 (137)	177.5 (177)	215.7
Herschel/PACS	160.0	360 (401)	360 (401)	25.6	421 (572)	421 (572)		127 (143)	127 (143)	23.0
Herschel/SPIRE	250.0	190 (217)	190 (217)	25.6		71.43 (87.60)	71.43 (87.60)	23.0
Herschel/SPIRE	350.0	93 (107)	93 (107)	25.6	...	29.35 (38.37)		29.35 (38.37)	29.35 (38.37)	23.0
Herschel/SPIRE	500.0	35.06 (40.65)	35.06 (40.65)	25.6	...	7.61 (12.45)		7.61 (12.45)	7.61 (12.45)	23.0
Facility	λ (μm)	$F_{\lambda, \text{fix}}$ (Jy)	$F_{\lambda, \text{var}}$ (Jy)	R_{ap} ($''$)	$F_{\lambda, \text{fix}}$ (Jy)	$F_{\lambda, \text{var}}$ (Jy)	R_{ap} ($''$)	$F_{\lambda, \text{fix}}$ (Jy)	$F_{\lambda, \text{var}}$ (Jy)	R_{ap} ($''$)	$F_{\lambda, \text{fix}}$ (Jy)	$F_{\lambda, \text{var}}$ (Jy)	R_{ap} ($''$)
Spitzer/IRAC	3.6	0.15 (0.17)	0.09 (0.11)	2.4	0.07 (0.09)	0.07 (0.03)	3.6	0.01 (0.02)	0.01 (0.01)	IRAS21391 MIR3	0.02 (0.03)	0.01 (0.03)	4.6
Spitzer/IRAC	4.5	0.43 (0.46)	0.29 (0.31)	2.4	0.07 (0.09)	0.05 (0.06)	2.4	0.07 (0.09)	0.05 (0.06)	IRAS21391 BMA2	0.06 (0.08)	0.05 (0.06)	4.6
Spitzer/IRAC	5.8	0.71 (0.77)	0.43 (0.50)	2.4	0.17 (0.25)	0.16 (0.20)	3.6	0.11 (0.17)	0.10 (0.12)	IRAS21391 BMA3	0.10 (0.15)	0.09 (0.11)	4.6
SOFIA/FORCAST	7.7	0.95 (1.10)	0.69 (0.85)	2.7	0.43 (0.71)	0.58 (0.88)	5.4	0.29 (0.39)	0.13 (0.22)	IRAS21391 MIR48	0.17 (0.37)	0.10 (0.24)	6.4
Spitzer/IRAC	8.0	1.03 (1.18)	0.66 (0.83)	2.7	0.38 (0.60)	0.40 (0.53)	4.8	0.12 (0.21)	0.11 (0.14)	IRAS21391 MIR48	0.11 (0.20)	0.11 (0.16)	6.4
SOFIA/FORCAST	19.7	3.64 (3.83)	3.49 (3.70)	3.6	0.64 (0.72)	0.26 (0.38)	2.3	0.45 (0.52)	0.46 (0.49)	IRAS21391 MIR48	0.28 (0.30)	0.49 (0.52)	5.4
SOFIA/FORCAST	31.5	4.99 (5.76)	4.99 (5.76)	3.8	1.96 (2.47)	1.63 (2.08)	3.8	6.81 (7.09)	6.26 (6.63)	IRAS21391 MIR48	8.30 (8.77)	8.26 (8.69)	8.1
SOFIA/FORCAST	37.1	6.15 (7.10)	6.15 (7.10)	3.8	3.18 (4.25)	3.18 (4.25)	4.6	11.27 (11.83)	11.27 (11.83)	IRAS21391 MIR48	12.94 (13.76)	12.94 (13.76)	8.5
IRAS	60.0	...	134 (220)	94.7	...	134 (220)	94.7	...	163 (178)		163 (178)	77.0	77.0
Herschel/PACS	70.0
IRAS	100.0	...	501 (937)	...	180.9 (180.9)	180.9 (180.9)	501	180.9 (180.9)	...	IRAS16562 N ^d	100.0 (100.0)	100.0 (100.0)	363
...	IRAS16562 N ^d

Table 2
(Continued)

Facility	λ (μm)	$F_{\lambda,\text{fix}}$ (Jy)	$F_{\lambda,\text{var}}$ (Jy)	R_{ap} ($''$)	$F_{\lambda,\text{fix}}$ (Jy)	$F_{\lambda,\text{var}}$ (Jy)	R_{ap} ($''$)	$F_{\lambda,\text{fix}}$ (Jy)	$F_{\lambda,\text{var}}$ (Jy)	R_{ap} ($''$)	$F_{\lambda,\text{fix}}$ (Jy)	$F_{\lambda,\text{var}}$ (Jy)	R_{ap} ($''$)	$F_{\lambda,\text{fix}}$ (Jy)	$F_{\lambda,\text{var}}$ (Jy)	R_{ap} ($''$)
Herschel/PACS	160.0	668 (1160)	668 (1160)	12.0
Herschel/SPIRE	250.0
Herschel/SPIRE	350.0
Herschel/SPIRE	500.0

Notes. The value of the flux density in the upper row is derived with background subtraction. The value in parentheses in the lower line is the flux density derived without background subtraction. The center of the aperture used for photometry of the IRAS images is not the same as the centers used at other wavelengths, but is determined based on the emission of the image alone. See more details in Papers I and II. The background-subtracted flux density of IRAS16562 N at 250, 350, and 500 μm is negative due to contamination of the IRAS 16562 main source presented in Paper II. So we use the non-background-subtracted flux density at these wavelengths as upper limits for the SED fitting of IRAS16562 N. There is no emission at wavelengths shorter than 8 μm from G305 A. So we use the non-background-subtracted flux density at these wavelengths as upper limits for the SED fitting of G305 A.

a Flux density derived with a fixed aperture size of the 70 μm data.

b Flux density derived with various aperture sizes.

c Aperture radius.

d Aperture is centered at the 37 μm peak at R.A. (J2000) = $16^{\text{h}}59^{\text{m}}43^{\text{s}}.010$, decl.(J2000) = $-40^{\circ}03'11''560$.

e Aperture is centered at the position of the 6.7 GHz methanol maser at R.A. (J2000) = $13^{\text{h}}11^{\text{m}}13^{\text{s}}.795$, decl.(J2000) = $-62^{\circ}54'41''741$ (Norris et al. 1993).

(This table is available in machine-readable form.)

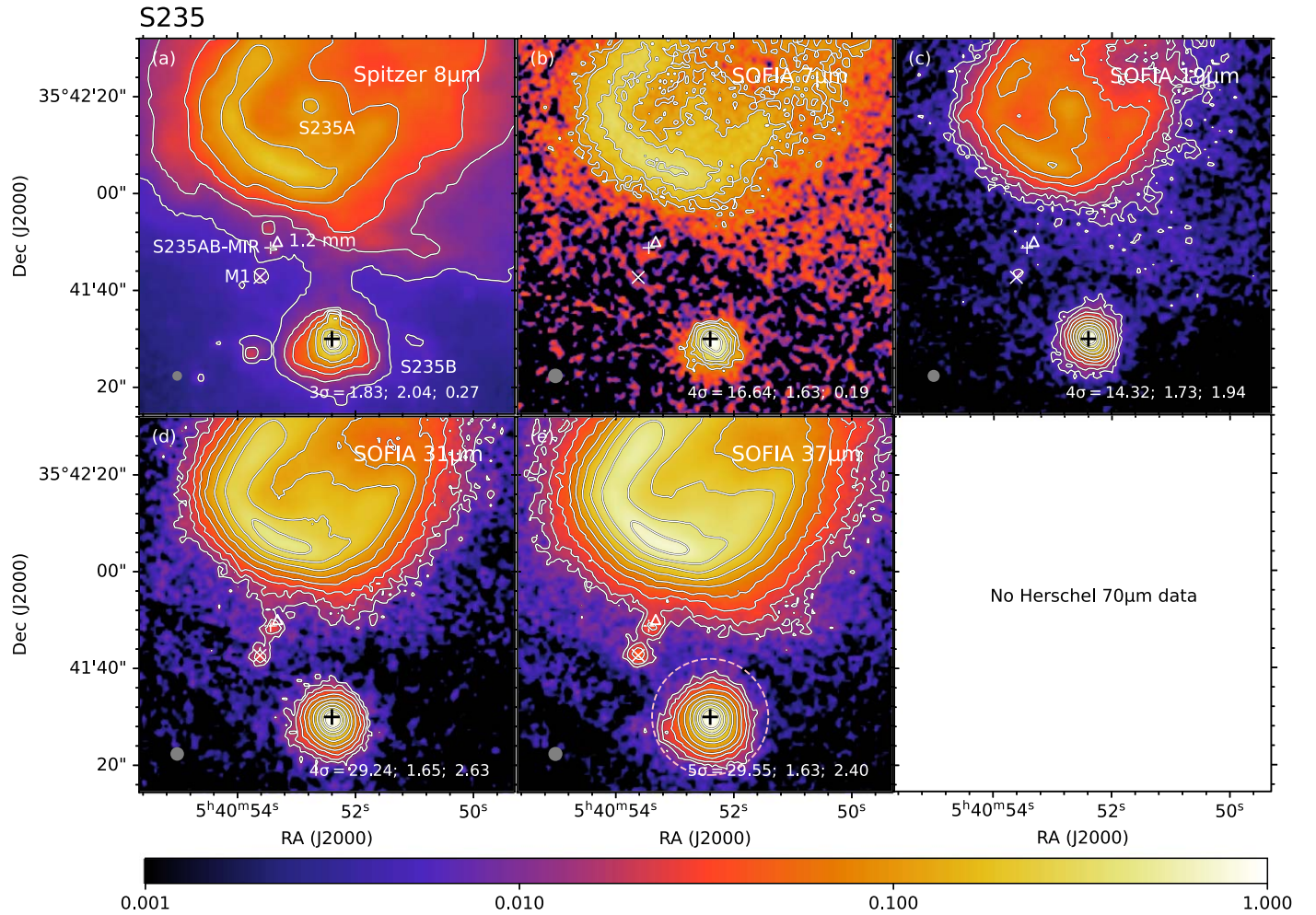


Figure 1. Multiwavelength images of S235 with the facility and wavelength given in the upper right corner of each panel. Contour level information is given in the lower right corner: the lowest contour level in number of σ above the background noise and the corresponding value in mJy per square arcsec; then the step size between each contour in \log_{10} mJy per square arcsec, then the peak flux in Jy per square arcsec. The color map indicates the relative flux intensity compared to that of the peak flux in each image panel. The pink dashed circle shown in panel (e) denotes the aperture used for the fiducial photometry. Gray circles in the lower left corner show the resolution of each image. The black cross in all panels denotes the position of the radio source VLA-2 of Felli et al. (2006) at R.A.(J2000) = $05^{\text{h}}40^{\text{m}}52^{\text{s}}.40$, decl.(J2000) = $+35^{\circ}41'30''$. The triangle marks the position of the 1.2 mm core. The small white cross marks the position of S235AB-MIR. The cross marks the position of the NIR K-band source M1 as well as VLA-1.

(The data used to create this figure are available.)

4.1.3. NGC 2071

NGC 2071 is a reflection nebula located at a distance of 390 pc in the L1630 molecular cloud of Orion B (Anthony-Twarog 1982). The three brightest members of the infrared cluster at $10\mu\text{m}$, IRS1, IRS2, and IRS3, are each associated with compact radio sources at 5 GHz (Snell & Bally 1986). The radio continuum emission of IRS1 and IRS3 and the water masers associated with them suggest that both sources are associated with thermal jets (Smith & Beck 1994; Torrelles et al. 1998; Seth et al. 2002). Higher resolution VLA observations (Trinidad et al. 2009) break IRS1 into three continuum peaks (IRS1E, 1C, and 1W), aligned in the east-west direction. Both the morphology and spectral index suggest that IRS1C is a thermal radio jet, while IRS1E and IRS1W could be condensations ejected by IRS1C. An energetic bipolar CO outflow has been observed toward NGC 2071, extending in the northeast-southwest direction and reaching $\sim 15'$ in length (Bally 1982). In addition, shock-excited molecular hydrogen

emission at $2.12\mu\text{m}$ has also been reported, showing a spatial extent similar to that of the CO outflow and revealing several H_2 outflows in the field, including one (flow II) perpendicular to the main outflow (flow I; Eislöffel 2000). Stojimirović et al. (2008) also detected CO(1–0) emission in the direction of flow II. Trinidad et al. (2009) tried to identify individual driving sources for each outflow based on the observations of Eislöffel (2000) and the elongation of the IRS3 jet. However, we note that higher resolution observations of the outflows are needed to better distinguish the driving sources in this region.

Based on radio continuum emission indicating the presence of thermal jets and water masers that are tracing disk-YSO outflow systems, it has been proposed that IRS1 and IRS3 are intermediate- and low-mass YSOs, respectively (Smith & Beck 1994; Torrelles et al. 1998; Seth et al. 2002; Trinidad et al. 2009). In our SOFIA images, the three sources IRS1, IRS2, and IRS3 are revealed at all wavelengths (see Figure 3). Here, we focus on the SED of the IRS1 source, but the aperture we adopt also includes IRS3.

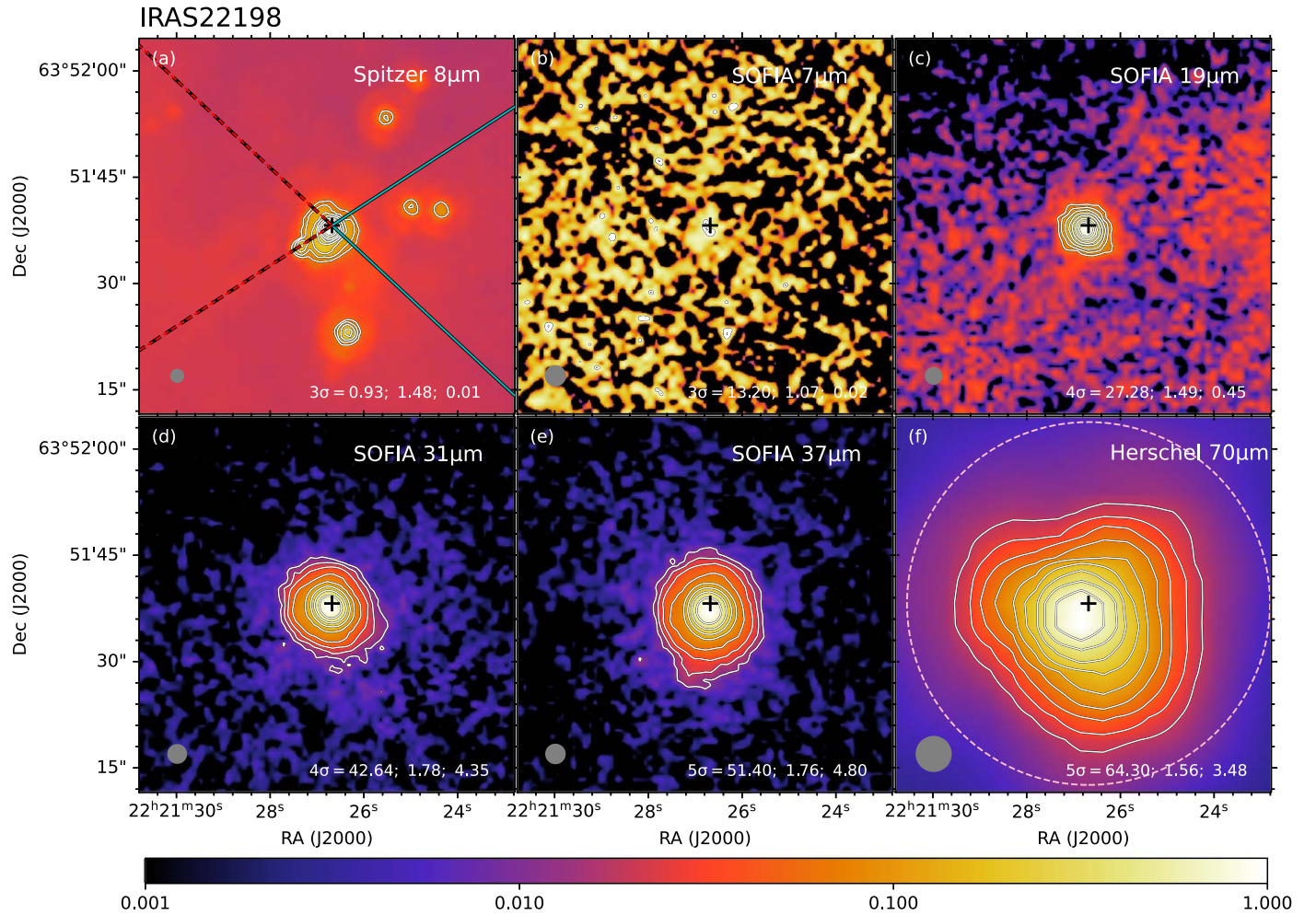


Figure 2. Multiwavelength images of IRAS 22198+6336, following the format of Figure 1. The black cross in all panels denotes the position of the 3.6 cm source in Sánchez-Monge et al. (2008) at R.A.(J2000) = $22^{\text{h}}21^{\text{m}}26^{\text{s}}.68$, decl.(J2000) = $+63^{\circ}51'38''.2$. The lines in panel (a) show the orientation of outflow axes, with the solid spans tracing blueshifted direction and the dashed spans redshifted direction. The outflow axis angles are from the CO(1–0) outflow emission of Sánchez-Monge et al. (2010).

(The data used to create this figure are available.)

4.1.4. Cepheus E

The Cepheus E (Cep E) molecular cloud is located at a distance of 730 pc (Sargent 1977). Since its early discovery by Wouterloot & Walmsley (1986) and Palla et al. (1993), subsequent studies have confirmed the central source Cep E-mm to be an isolated IM protostar in the Class 0 stage (Lefloch et al. 1996; Moro-Martín et al. 2001). The source drives a very luminous molecular outflow and jet (Lefloch et al. 2011, 2015), terminated by the bright Herbig-Haro (HH) object HH377 in the south (Ayala et al. 2000). The $21''$ long jet, the HH 377 terminal bow-shock, and the outflow cavity are clearly revealed in multiple CO transitions and the [OI] $63\ \mu\text{m}$ line (Gusdorf et al. 2017). The observations are interpreted by means of time-dependent magnetohydrodynamics (MHD) shock models by Lefloch et al. (2015). Ospina-Zamudio et al. (2018) reveal Cep E-mm as a binary protostellar system with NOEMA observations. They identified two components from a two-component fit to the visibilities, Cep E-A and Cep E-B, which are separated by $\sim 1.7''$. Ospina-Zamudio et al. argued that Cep E-A dominates the core continuum emission and

powers the well-known high-velocity jet associated with HH 377, while the lower flux source Cep E-B powers another high-velocity molecular jet revealed in SiO(5–4) propagating in a direction close to perpendicular with respect to the Cep E-A jet. The spectra of molecular lines observed by NOEMA show bright emission of O- and N-bearing complex organic molecules (COMs) around Cep E-A and no COM emission toward Cep E-B.

From our SOFIA images (Figure 4), we are not able to resolve the potential binary system, so our modeling is an approximation of the properties of Cep E-A, assuming it dominates the system. The IR emission along the main jet is clearly seen in the Spitzer $8\ \mu\text{m}$ image and also in the Herschel $70\ \mu\text{m}$ image because these space-based observations are more sensitive to fainter emission features.

4.1.5. L1206

L1206, also known as IRAS 22272+6358, is located at a distance of 776 pc from the trigonometric parallaxes of 6.7 GHz methanol masers (Rygl et al. 2010). Two MIR sources

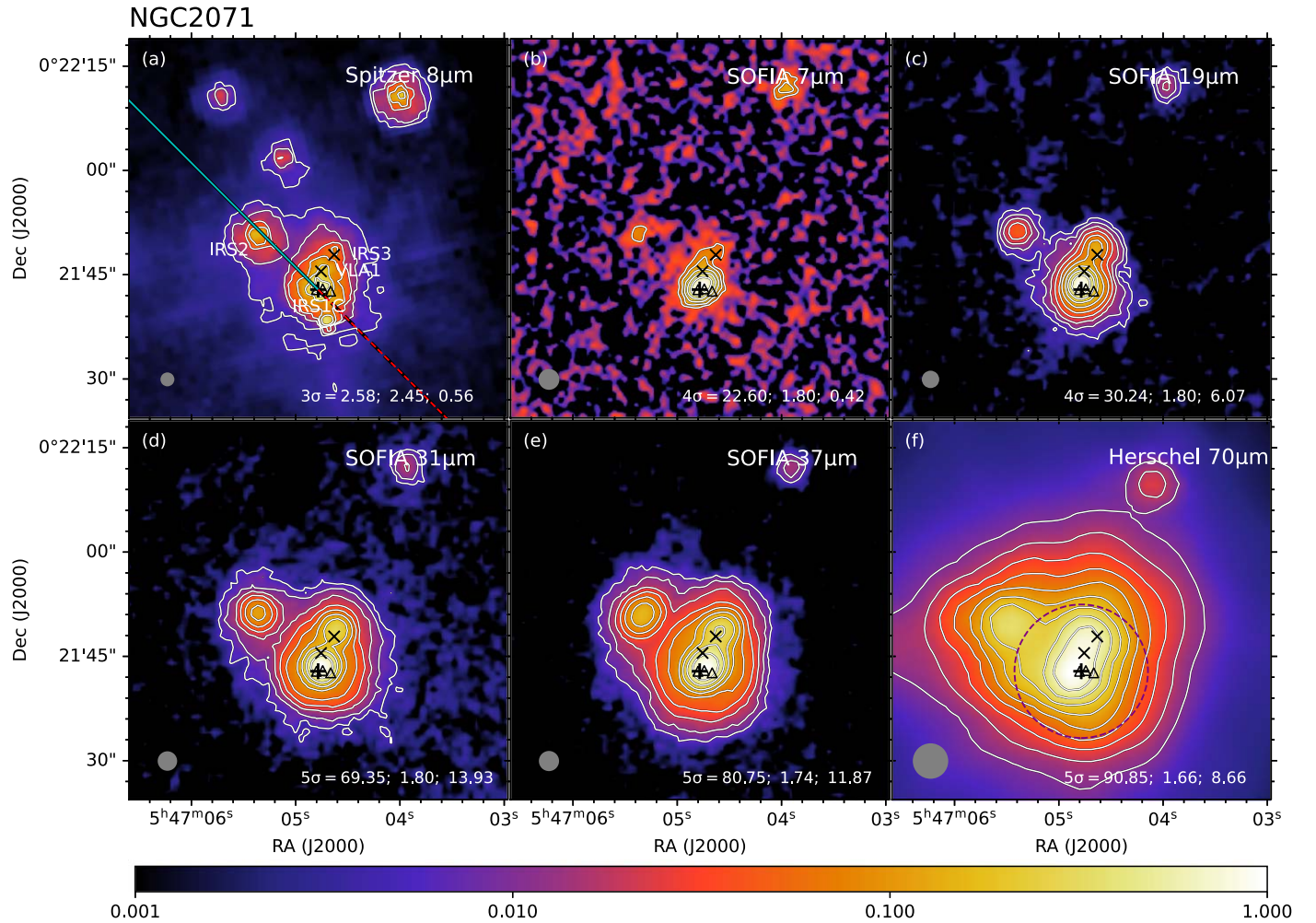


Figure 3. Multiwavelength images of NGC 2071. The black cross in all panels denotes the position of the 1.3 cm source IRS 1C in Trinidad et al. (2009) at R.A. (J2000) = $05^{\text{h}}47^{\text{m}}04^{\text{s}}.741$, decl.(J2000) = $+00^{\circ}21'42''.96$. The crosses from north to south mark the positions of the 1.3 cm sources IRS 3 and VLA1, respectively. The triangles from east to west mark the positions of the 1.3 cm sources IRS 1E, IRS 1W, and IRS 1Wb, respectively. The lines in panel (a) show the orientation of the outflow axis (flow I), with the solid span tracing the blueshifted direction and the dashed span the redshifted direction. The outflow axis angle is from the high-velocity CO(1–0) main outflow emission of Stojimirović et al. (2008). Note that the center of the outflow has an uncertainty of $\sim 5''$ and is not necessarily at IRS 1C.

(The data used to create this figure are available.)

lie in our field of view. The western source IRAS 22272+6358 A (hereafter referred to as L1206 A) has no optical counterpart, and at NIR wavelengths, it has only been seen in scattered light (Ressler & Shure 1991). Given its extremely low 60/100 μm color temperature, L1206 A is believed to be deeply embedded, cold, and young (Ressler & Shure 1991; Beltrán et al. 2006). It has been detected at 2.7 and 2 mm, but not at 2 or 6 cm (Wilking et al. 1989; McCutcheon et al. 1991; Sugitani et al. 2000; Beltrán et al. 2006). The 2.7 mm continuum observations by Beltrán et al. (2006) revealed four sources, OVRO 1, OVRO 2, OVRO 3, and OVRO 4, in a $12''$ vicinity of L1206 A. The strongest mm source, OVRO 2, is most likely the YSO associated with L1206 A, and is probably the driving source of the CO molecular outflow detected in the region. The dust emission morphology and properties of OVRO 2 suggest that this IM protostar is probably in transition between Class 0 and I.

The K , L , L' , and M filter images of L1206 A clearly reveal lobes in a bipolar system (Ressler & Shure 1991). There is a distinct $3''$ – $4''$ gap between the two lobes at the K , L , and L' bands. Because the proposed illuminating source lies within

this gap, it was suggested by Ressler & Shure (1991) that this gap is produced by the extreme extinction of a thick circumstellar disk. We also see such a gap in the 3.6, 4.5, and 5.8 μm images. The CO(1–0) observations of Beltrán et al. (2006) reveal a very collimated outflow driven by OVRO 2 with a very weak southeastern red lobe and a much stronger northwestern blue lobe. The relative brightness of the red lobe also decreases monotonically at the K , L , and L' bands (Ressler & Shure 1991). Beltrán et al. (2006) suggested a scenario in which photodissociation produced by the ionization front coming from the bright-rimmed diffuse H II region in the south could be responsible for the weakness of the redshifted lobe and its overall morphology.

The elongation along the outflow direction of L1206 A is clearly revealed at 8 μm . We see a slight extension along the outflow direction in our SOFIA images, especially at 31 μm and 37 μm (see Figure 5).

IRAS 22272+6358 B (hereafter referred to as L1206 B) is a bluer but less luminous object, which lies approximately $40''$ to the east of L1206 A. Because L1206 B is directly visible in the NIR and is likely to be a less obscured young stellar object,

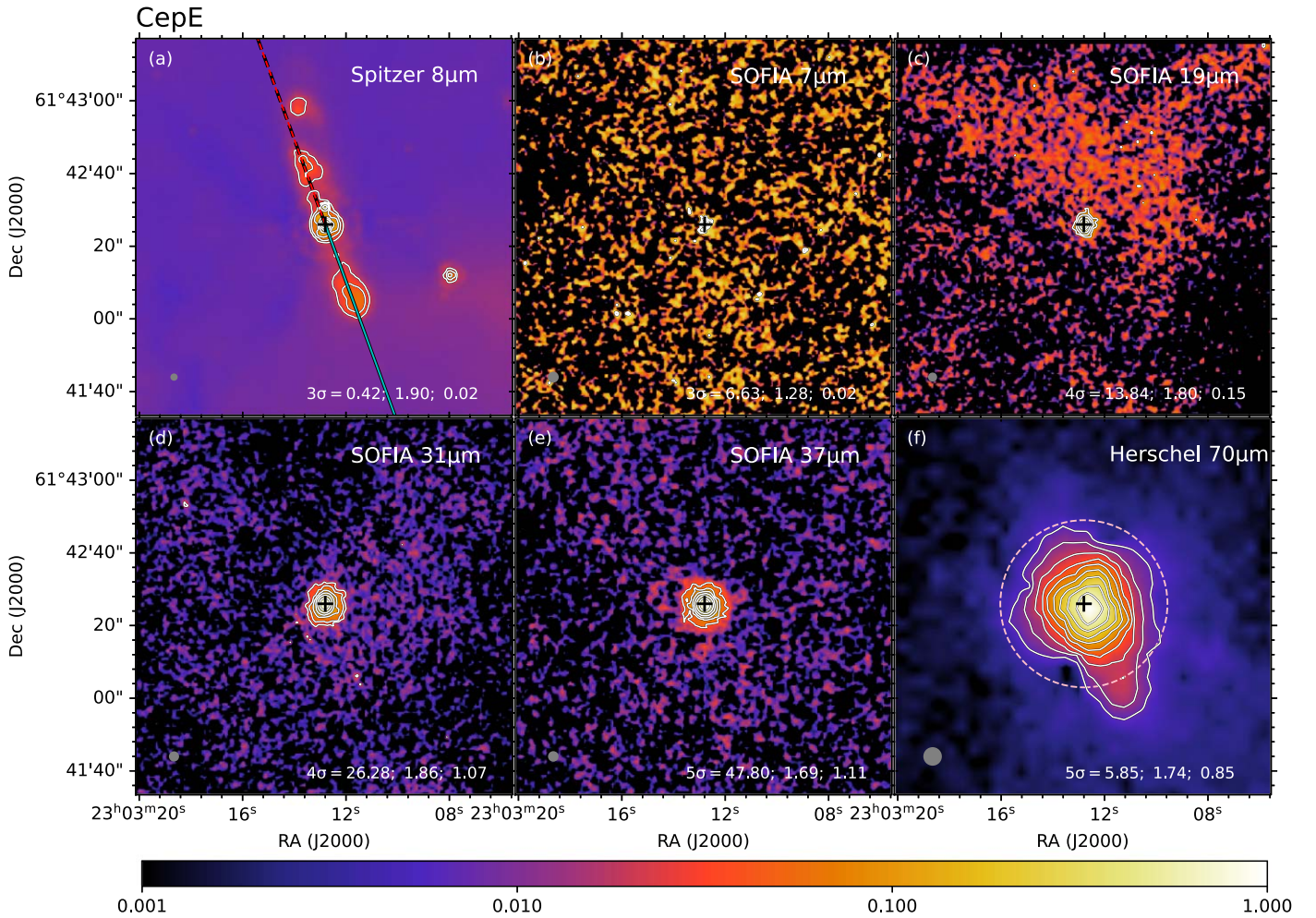


Figure 4. Multiwavelength images of Cep E. The black cross in all panels denotes the position of the 1.3 mm source CepE-A in Ospina-Zamudio et al. (2018) at R.A. (J2000) = $23^{\text{h}}03^{\text{m}}12^{\text{s}}.8$, decl.(J2000) = $+61^{\circ}42'26''$. The lines in panel (a) show the orientation of the outflow axis, with the solid span tracing the blueshifted direction and the dashed span the redshifted direction. The outflow axis angle is defined by the CO(2–1) outflow emission of Lefloch et al. (2015).

(The data used to create this figure are available.)

Ressler & Shure (1991) suggested that L1206 B is most likely a late Class I object or perhaps an early Class II object, whose photospheric spectrum is heavily extinguished by the parent cloud and is also affected by emission from a circumstellar disk.

From our SOFIA images, it can be seen that the emission of L1206 B becomes weaker at longer wavelengths, which also indicates that L1206 B may be more evolved than L1206 A.

4.1.6. IRAS 22172+5549

IRAS 22172+5549 is located at a kinematic distance of 2.4 kpc (Molinari et al. 2002). As a luminous IRAS source in the survey of Molinari et al. (2002), IRAS 22172 shows the presence of a compact dusty core without cm continuum emission, with prominent wings in the $\text{HCO}^+(1-0)$ line. Fontani et al. (2004) studied the 3 mm continuum and CO(1–0) emission in this region, finding a CO bipolar outflow centered at MIR2 (IRS1 in their nomenclature), which is offset by $\sim 7''.5$ from the 3.4 mm peak. They suggested that the dusty core might host a source in a very early evolutionary stage prior to the formation of an outflow. From the outflow parameters, they proposed that MIR2, as the driving source, must be

relatively massive. Palau et al. (2013) carried out higher angular resolution 1.3 mm and CO(2–1) observations. They detected more mm sources, including one confirmed protostar with no IR emission that is driving a small outflow (MM2), two protostellar candidates detected only in the mm range (MM3 and MM4), and one protostellar object detected in the mm and IR, with no outflow (MM1). MIR2 is still detected only in the IR and is driving the larger CO(1–0) outflow. No mm emission or molecular outflows are detected toward MIR1 or MIR3. It is clear that IRAS 22172 harbors a rich variety of YSOs at different evolutionary stages.

Our SOFIA images (see Figure 6) reveal extended emission along the blueshifted outflow from MIR2, which could come from the outflow cavity.

4.1.7. IRAS 21391+5802

IRAS 21391+5802 is deeply embedded in the bright-rimmed globule IC 1396N located at a distance of 750 pc (Matthews 1979). This region exhibits all of the signposts of an extremely young object, such as strong submm and mm dust continuum emission (Wilking et al. 1993; Sugitani et al. 2000; Codella et al. 2001), line emission from high-density gas

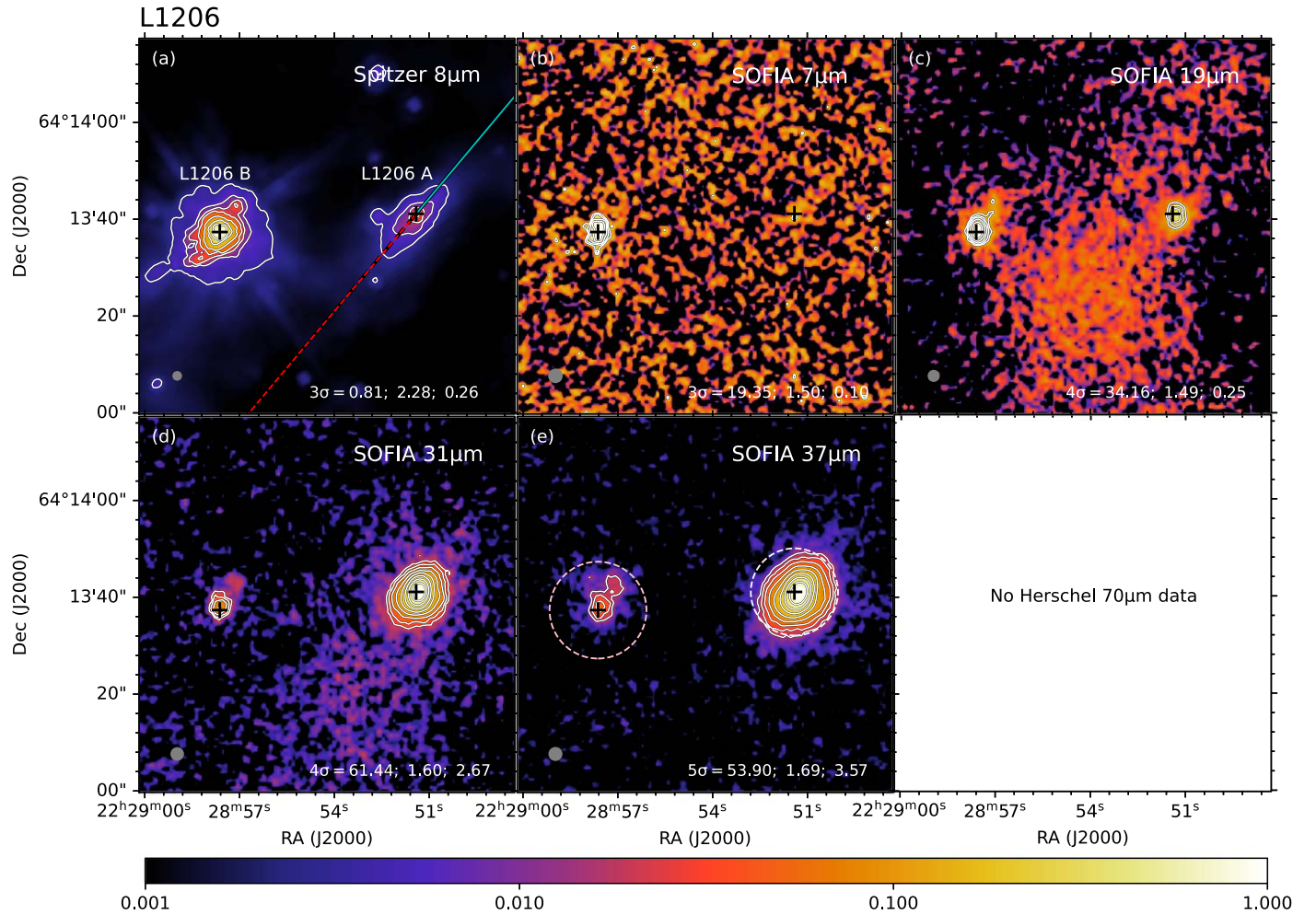


Figure 5. Multiwavelength images of L1206. The black crosses in all panels from east to west denote the position of the 8 μm peak of L1206 B at R.A. (J2000) = 22^h28^m57^s.626, decl.(J2000) = +64°13′37″.348 and the position of L1206 A coincident with that of the 2.7 mm source OVRO 2 in Beltrán et al. (2006) at R.A.(J2000) = 22^h28^m51^s.41, decl.(J2000) = +64°13′41″.1, respectively. The lines in panel (a) show the orientation of the outflow axis from L1206 A, with the solid span traces the blueshifted direction and the dashed span the redshifted direction. The outflow axis angle is given by the CO(1–0) outflow emission of Beltrán et al. (2006).

(The data used to create this figure are available.)

tracers (Serabyn et al. 1993; Cesaroni et al. 1999; Codella et al. 2001), and water maser emission (Felli et al. 1992; Tofani et al. 1995; Patel et al. 2000; Valdetaro et al. 2005). Sugitani et al. (1989) discovered an extended CO bipolar outflow, which was later also mapped by Codella et al. (2001). NIR images of the region have revealed a collimated 2.12 μm H₂ jet driven by IRAS 21391 (Nisini et al. 2001; Beltrán et al. 2009). Based on mm observations, Beltrán et al. (2002) resolved IRAS 21391 into an IM source called BIMA 2, surrounded by two less massive and smaller objects, BIMA 1 and BIMA 3. Choudhury et al. (2010) identified MIR-50 and 54 as the MIR counterparts of BIMA 2 and BIMA 3 and did not detect any source associated with BIMA 1. The source located ~25″ to the north of BIMA 2 was identified as MIR-48. BIMA 1, BIMA 2, and BIMA 3 are all associated with 3.6 cm continuum emission (Beltrán et al. 2002). Figure 7 shows the region as seen by Spitzer at 8 μm and by SOFIA-FORCAST. Our analysis focusses on the MIR-48, BIMA 2 and BIMA3 sources.

A strong CO(1–0) outflow along the east–west direction is centered at the position of BIMA 2, and other collimated,

weaker, and smaller bipolar outflows, elongated along the north–south direction, are associated with BIMA 1, which is only detected at low velocities (see Figure 4 in Beltrán et al. 2002). At the position of MIR-48, we see weak overlapping blue- and redshifted CO(1–0) emission, which is also only detected at low velocities. There is no molecular emission detected toward BIMA 3. The east–west outflow driven by BIMA 2 is highly collimated, and the collimation remains even at low outflow velocities. Beltrán et al. (2002) interpreted the complex morphology of the outflows as being the result of the interaction of the high-velocity gas with dense clumps surrounding the protostar. They also suggested that BIMA 2 fits correlations between source and outflow properties for low-mass Class 0 objects given by Bontemps et al. (1996) very well.

Neri et al. (2007) used still higher angular resolution millimeter interferometric observations to reveal that BIMA 2 is a cluster of multiple compact sources; the primary source is called IRAM 2A. The detection of warm CH₃CN in IRAM 2A implies that this is the most massive protostar and could be the driving source of this energetic outflow. This interpretation is

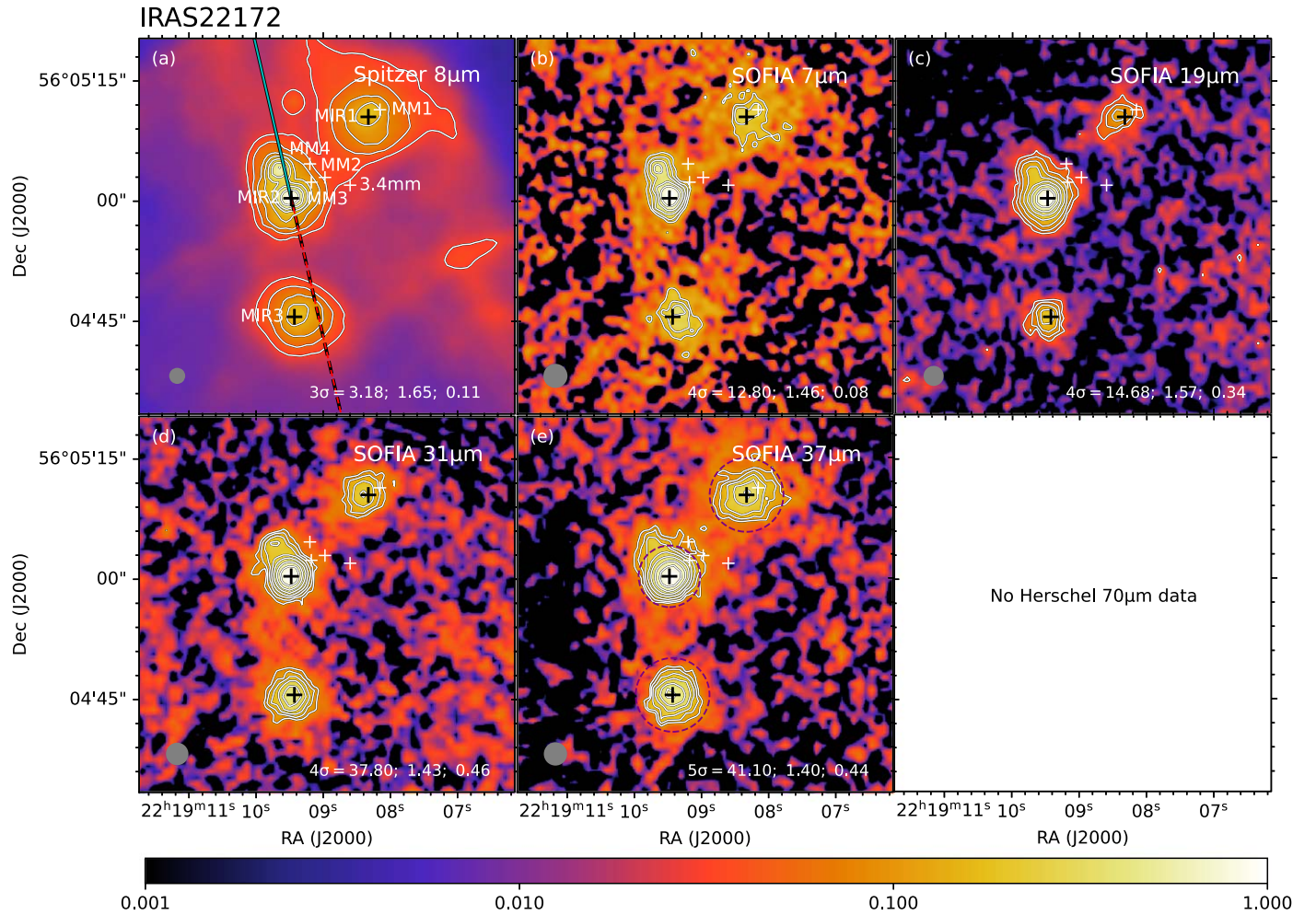


Figure 6. Multiwavelength images of IRAS 22172. The black crosses in all panels from north to south denote the positions of the MIR peaks at $37\ \mu\text{m}$ MIR1 at R.A. (J2000) = $22^{\text{h}}19^{\text{m}}08^{\text{s}}.328$, decl.(J2000) = $+56^{\circ}05'10''.522$, MIR2 at R.A.(J2000) = $22^{\text{h}}19^{\text{m}}09^{\text{s}}.478$, decl.(J2000) = $+56^{\circ}05'00''.370$, and MIR3 at R.A. (J2000) = $22^{\text{h}}19^{\text{m}}09^{\text{s}}.430$, decl.(J2000) = $+56^{\circ}04'45''.581$, respectively. The white crosses from north to south mark the positions of the 1.3 mm sources MM1, MM4, MM2, and MM3 in Palau et al. (2013) and the 3.4 mm source in Molinari et al. (2002; also the mm core I22172-C in Fontani et al. 2004). The lines in panel (a) show the orientation of the outflow axis from MIR2, with the solid span tracing blueshifted direction and the dashed span tracing redshifted direction. The outflow axis angle is from the CO(1–0) outflow emission of Fontani et al. (2004).

(The data used to create this figure are available.)

also supported by the morphology of the 1.2 mm and 3.1 mm continuum emission, which is extended along the outflow axis tracing the warm walls of the biconical cavity (Fuente et al. 2009). The CH_3CN abundance toward IRAM 2A is similar to that found in low-mass hot corinos and lower than that expected toward IM and high-mass hot cores. Based on the low CH_3CN abundance, Fuente et al. (2009) suggested that IRAM 2A is a low-mass or a Herbig Ae star and not the precursor of a massive Be star, or alternatively, that IRAM 2A is a Class 0/I transition object that has already formed a small photodissociation region (PDR).

For BIMA 1 and BIMA 3, Beltrán et al. (2002) suggested that they are more evolved low-mass objects given their low dust emissivity index and the more compact appearance of their dust emission.

While extended morphologies of the three sources are revealed in our SOFIA images (see Figure 7), the extension of BIMA 2 does not follow the northeast-southwest direction of the major outflow or the north–south direction of the weak low-velocity outflow.

4.2. General Results from the SOFIA Imaging

Most of the sources presented in this paper are associated with outflows. In a few cases, such as IRAS 22198, L1206 A and IRAS 22172 MIR2, the SOFIA 20 to $40\ \mu\text{m}$ images show modest extensions in the directions of the outflow axes, which was a common feature of the high-mass protostars in Papers I and II. However, the appearance of most of the IM protostars in the SOFIA images is quite compact, i.e., only a few beams across, and relatively round. In some of these cases, such as IRAS 22198, Cep E, and IRAS 21391 (BIMA 2) Spitzer $8\ \mu\text{m}$ images, which are sensitive to lower levels of diffuse emission, do reveal outflow axis elongation, which the SOFIA images are not able to detect. One contributing factor here is likely to be that the IM protostars are intrinsically less luminous than high-mass protostars and so produce less extended MIR emission. Another factor may be that the mass surface densities of their clump environments are lower than those of high-mass protostars (this is revealed in the derived values of Σ_{cl} from the SED fitting; see Section 4.3.2) and thus their MIR to FIR emission can appear more compact and more apparently

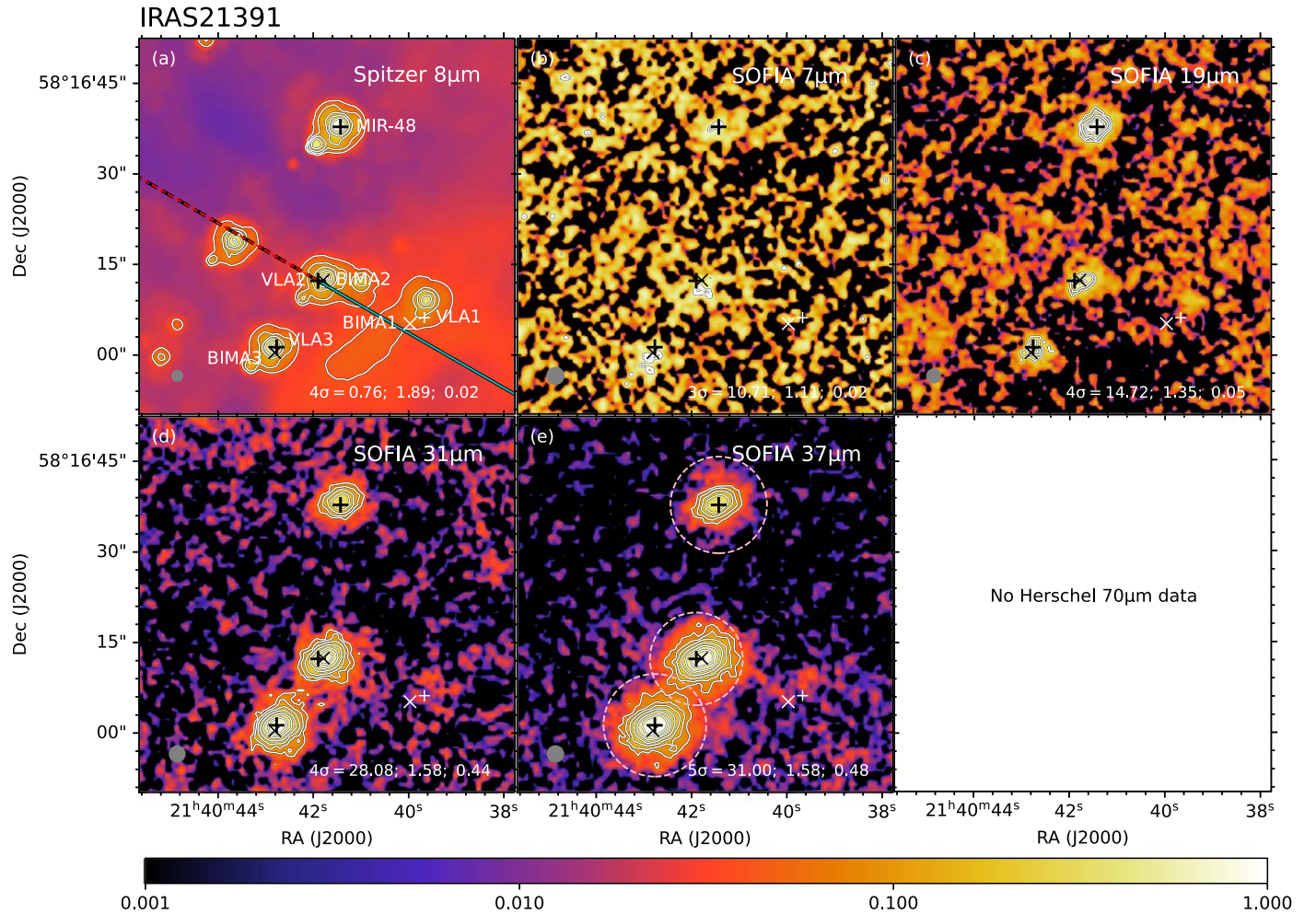


Figure 7. Multiwavelength images of IRAS 21391. The black crosses in all panels from north to south denote the positions of the MIR source MIR-48 at R.A. (J2000) = $21^{\text{h}}40^{\text{m}}41^{\text{s}}.43$, decl.(J2000) = $+58^{\circ}16'37''.8$ in Choudhury et al. (2010) and 3.6 cm sources VLA2 at R.A.(J2000) = $21^{\text{h}}40^{\text{m}}41^{\text{s}}.90$, decl.(J2000) = $+58^{\circ}16'12''.3$ and VLA3 at R.A.(J2000) = $21^{\text{h}}40^{\text{m}}42^{\text{s}}.77$, decl.(J2000) = $+58^{\circ}16'01''.3$ in Beltrán et al. (2002). The white crosses marks the position of the 3.6 cm source VLA1. The crosses from east to west mark the positions of the 3.1 mm sources BIMA3, BIMA2, and BIMA1. The lines in panel (a) show the orientation of the outflow axis from VLA2/BIMA2, with the solid span tracing blueshifted direction and the dashed span tracing redshifted direction. The outflow axis angle is given by the high-velocity CO(1–0) main outflow emission of Beltrán et al. (2002).

(The data used to create this figure are available.)

symmetric. Three-color images of all the sources are presented together in Figure 8.

We note that three of our sources are resolved into at least two components by higher angular resolution mm observations (within ~ 0.01 pc), including IRAS 22198, Cep E, and IRAS 21391 BIMA2. A few mm sources are detected close to the main MIR source in IRAS 22172 located $3''$ – $8''$ (0.03–0.09 pc) away, and a few mm sources are detected close to L1206 A located $\sim 12''$ (0.04 pc) away. Several jet-like condensations are revealed by radio observations in NGC 2071 IRS1 (within ~ 0.01 pc). This indicates that at least some of the protostars in our sample may have nearby companions.

From Figure 9, we see that three of the sources have high-resolution UKIDSS NIR imaging: S235, IRAS 22172, and IRAS 21391. These images show the presence of a number of NIR sources in the vicinities of the protostars, especially for S235 and IRAS 22172, which may be associated clusters of YSOs. On the other hand, IRAS 22198, NGC 2071, Cep E, and L1206 appear more isolated in their NIR images, although is

must be noted that these images have lower resolution and higher noise levels. We also note that S235 B is located (in projection) near the center of its cluster, while IRAS22172 MIR2 is closer to the eastern edge of its cluster.

4.3. Results of SED Model Fitting

4.3.1. The SEDs

Figure 10 shows the SEDs of the 14 sources presented in this paper. Ten sources lack Herschel 70 and 160 μm observations, which makes it difficult to determine the location of the peak of their SEDs. Of the remaining four sources, NGC 2071 has an SED that peaks between 37 and 70 μm , while IRAS 22198, Cep E, and G305 A have their peaks around 70 μm . It is noticeable that L1206 B, IRAS22172 MIR2, IRAS22172 MIR1, IRAS21391 MIR48, and IRAS16562 N have very flat MIR SEDs, and especially L1206 B even shows decreasing flux densities as the wavelength increases.

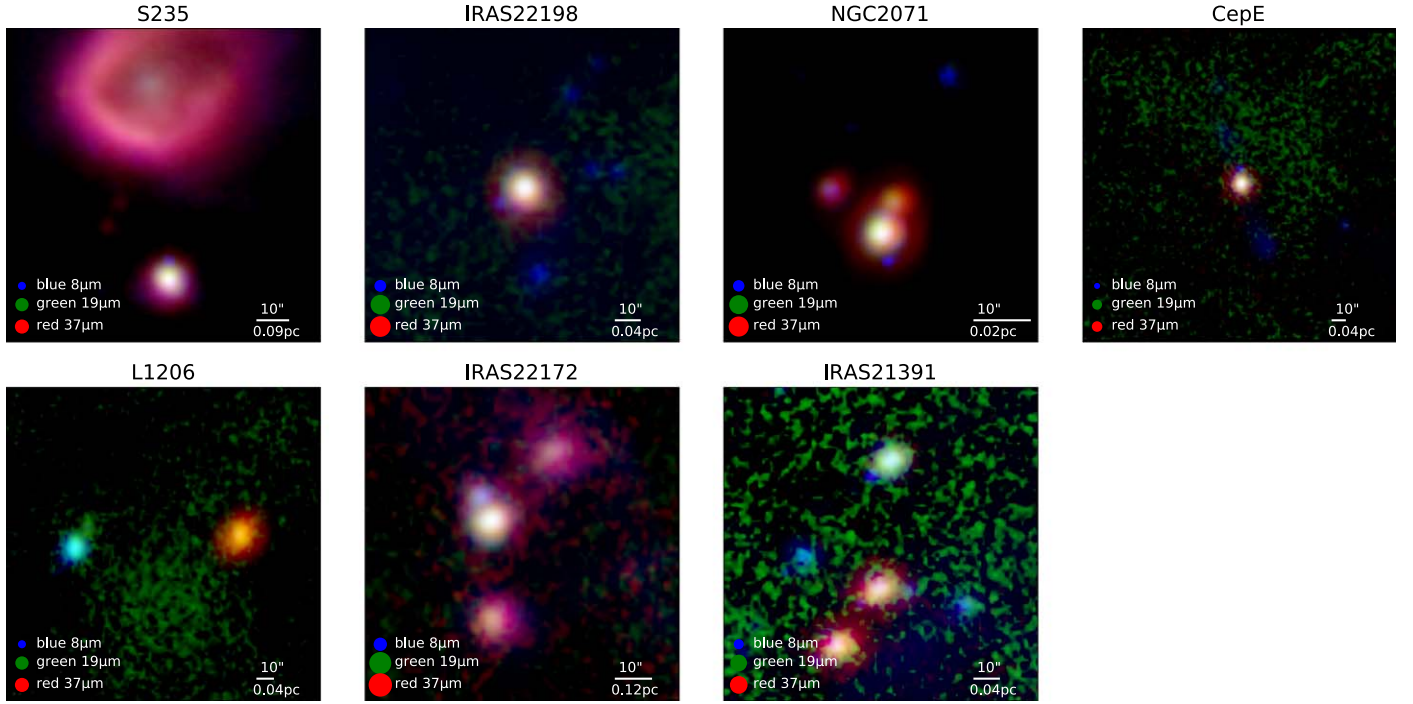


Figure 8. Gallery of RGB images of the seven new regions analyzed in this paper, as labeled. The color intensity scales are stretched as arcsinh and show a dynamic range of 100 from the peak emission at each wavelength. The legend shows the wavelengths used and the beam sizes at these wavelengths. SOFIA–FORCAST $37\ \mu\text{m}$ is shown in red. SOFIA–FORCAST $19\ \mu\text{m}$ is shown in green. Spitzer $8\ \mu\text{m}$ is shown in blue.

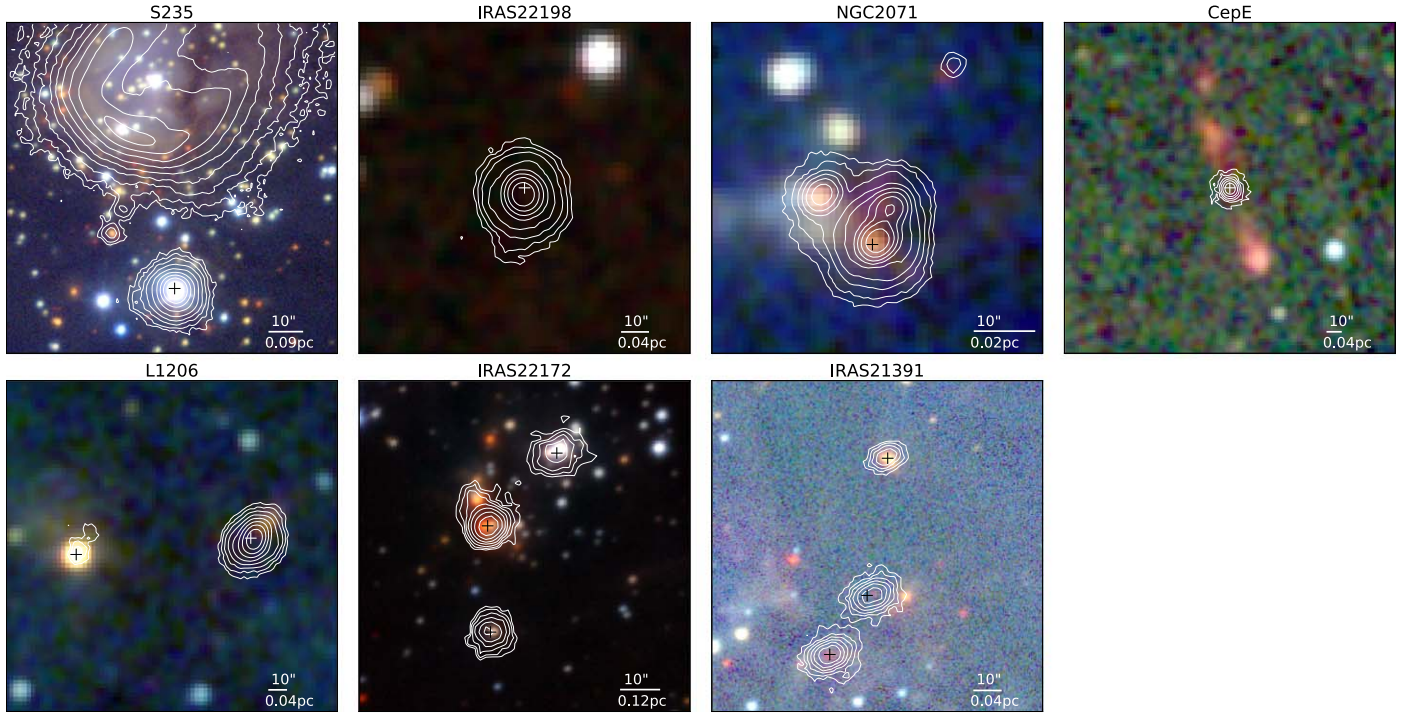


Figure 9. NIR RGB images of the seven new regions analyzed in this paper, as labeled. The data of S235, IRAS 22172, and IRAS 21391 are from the UKIDSS survey (Lawrence et al. 2007). The data of IRAS 22198, NGC 2071, Cep E and L1206 are from the 2MASS survey (Skrutskie et al. 2006). K-band data are shown in red, H band data in green, and J band data in blue. The white contours are the SOFIA $37\ \mu\text{m}$ emission, with the same levels as displayed in the previous individual figures for each source. The crosses in each panel are the same as those in the previous individual figures. The scale bar is shown in the right corner of each panel.

4.3.2. ZT Model Fitting Results

We now consider the results of fitting the ZT protostellar RT models to the SEDs. Note that a general comparison of differences in results when the Robitaille et al. (2007) RT

models were used was carried out in Paper I, with some of the main results being that the Robitaille et al. models often give solutions with very low accretion rates, which are not allowed in the context of the ZT models. As discussed in Paper I, our preference is to use the ZT models for the analysis of the

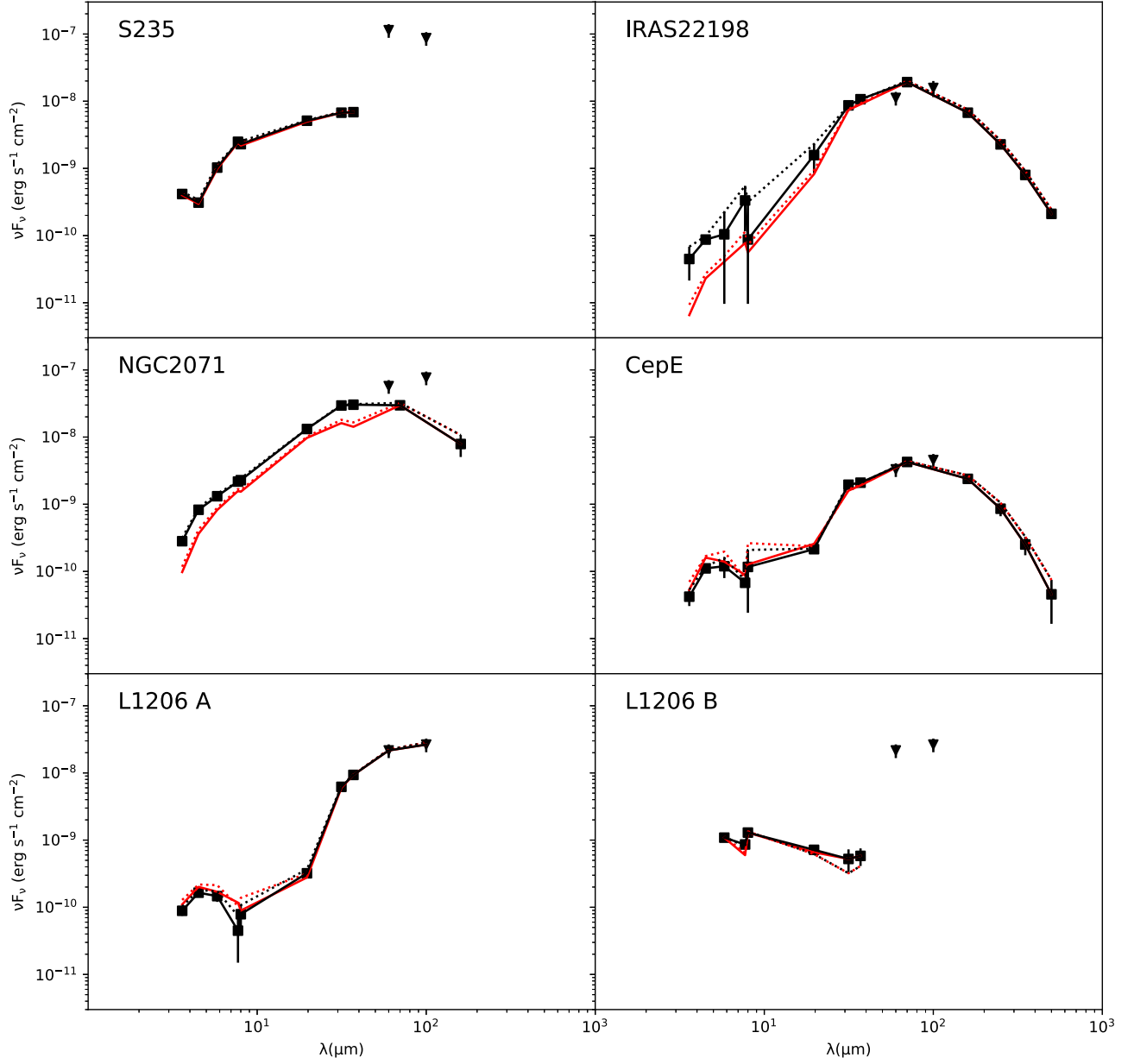


Figure 10. SEDs of the 14 presented sources. Total fluxes without background subtraction are shown with dotted lines. The fixed-aperture case is shown by the dotted black line, and the variable aperture (at $<70 \mu\text{m}$) case is shown with the dotted red line. The background-subtracted SEDs are shown with solid lines: black for fixed aperture (the fiducial case), and red for variable aperture. Solid black squares indicate the actual measured values that sample the fiducial SED. Black triangles denote the flux densities measured with IRAS. The down arrows in G305 A and IRAS16562 N denote that those data points are fluxes without background subtraction and are treated as upper limits.

SOMA sources because these models have been developed specifically for massive star formation under a physically self-consistent scenario, including full protostellar evolution, and with relatively few free parameters. Figure 11 shows the results of fitting the ZT protostellar RT models to the fixed-aperture background-subtracted SEDs, which is the fiducial analysis method presented in Papers I and II. In general, reasonable fits can be found to the observed SEDs, i.e., with relatively low values of reduced χ^2 .

A summary of the fitted parameter results in the $\Sigma_{\text{cl}} - M_c - m_*$ parameter space is shown for each source in Figure 12. Note that the clump environment mass surface density, Σ_{cl} (ranging from 0.1 to 3 g cm^{-2}), and initial core mass, M_c (ranging from 10 to $480 M_\odot$), are the primary physical

parameters of the initial conditions of the ZT models, while the current protostellar mass, m_* (ranging from $0.5 M_\odot$ up to about 50% of M_c , with this efficiency set by disk-wind-driven outflow feedback), describes the evolutionary state of stars forming from such cores. The two other independent parameters of the models are the angle of the line of sight to the outflow axis, θ_{view} , and the amount of foreground extinction, A_V , with all other model parameters being completely specified by Σ_{cl} , M_c , and m_* . Note that $L_{\text{bol,iso}}$ represents the isotropic bolometric luminosity, i.e., without correction for the inclination, and L_{bol} represents the intrinsic bolometric luminosity. The best five model fits for each source are listed in Table 3. Note that χ^2 listed in this table is the reduced χ^2 , i.e., already normalized by the number of data

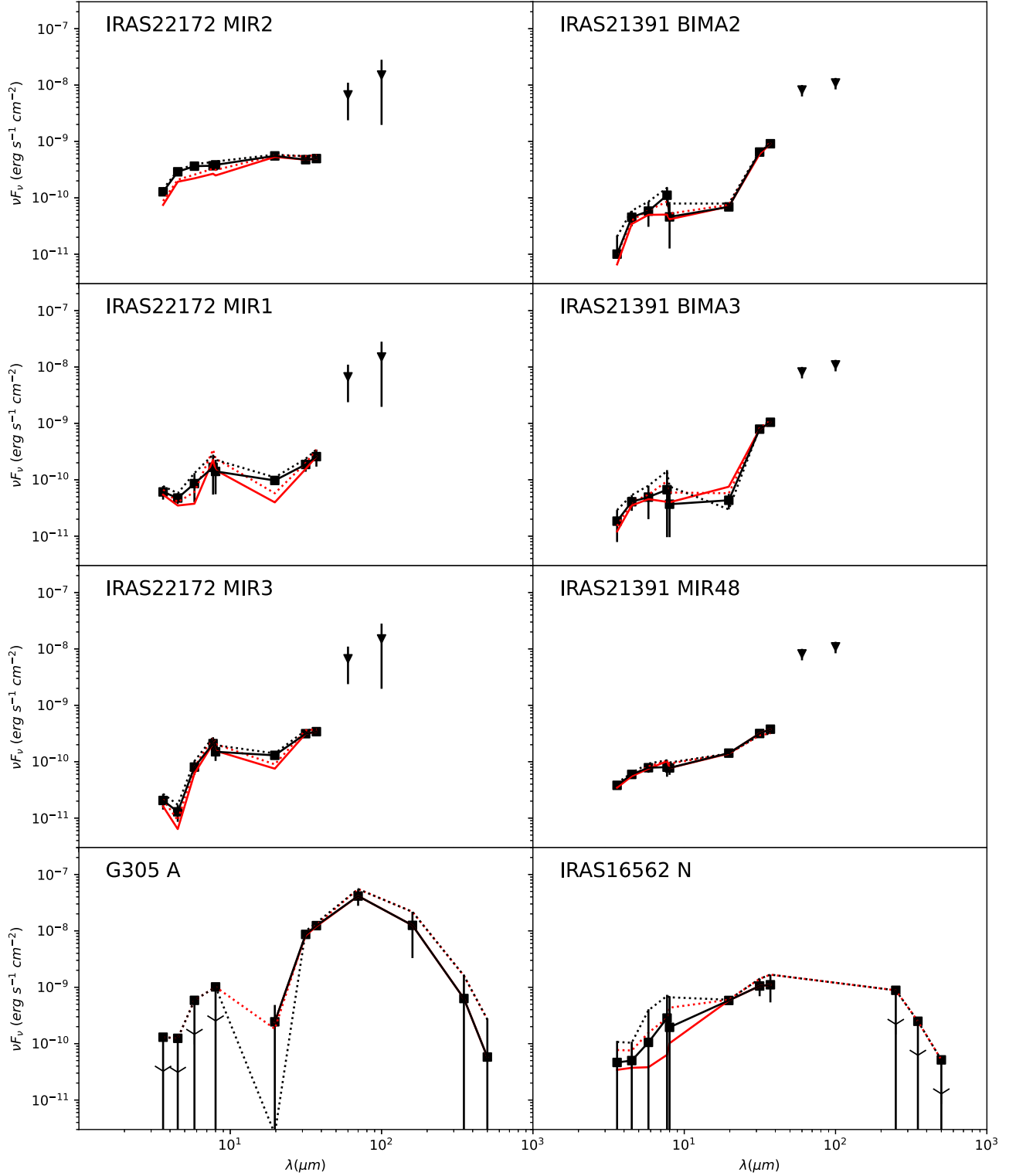


Figure 10. (Continued.)

points used in the fitting. Note also that Table 4 of Paper II incorrectly listed this as quantity as χ^2/N , rather than as χ^2 used here and in Paper I.

The best-fit models indicate that S235 and G305 A are more likely to be high-mass protostars, with most of the models (except for the best model for S235) returning protostellar masses $m_* \geq 12 M_\odot$, accretion rates $\dot{m}_* \sim 10^{-5}$ – a few \times

$10^{-4} M_\odot \text{ yr}^{-1}$, initial core masses $M_c \sim 50\text{--}400 M_\odot$, clump mass surface densities $\Sigma_{\text{cl}} \sim 0.1\text{--}1 \text{ g cm}^{-2}$, and isotropic luminosities $L_{\text{bol,iso}} \sim 10^3\text{--}a \text{ few} \times 10^4 L_\odot$.

We find that IRAS 22198, NGC 2071, L1206 A, L1206 B, IRAS22172 MIR2, IRAS22172 MIR3, IRAS21391 MIR48, and IRAS16562 N are likely to currently be IM protostars, with most models returning protostellar masses $m_* \sim 2\text{--}8 M_\odot$,

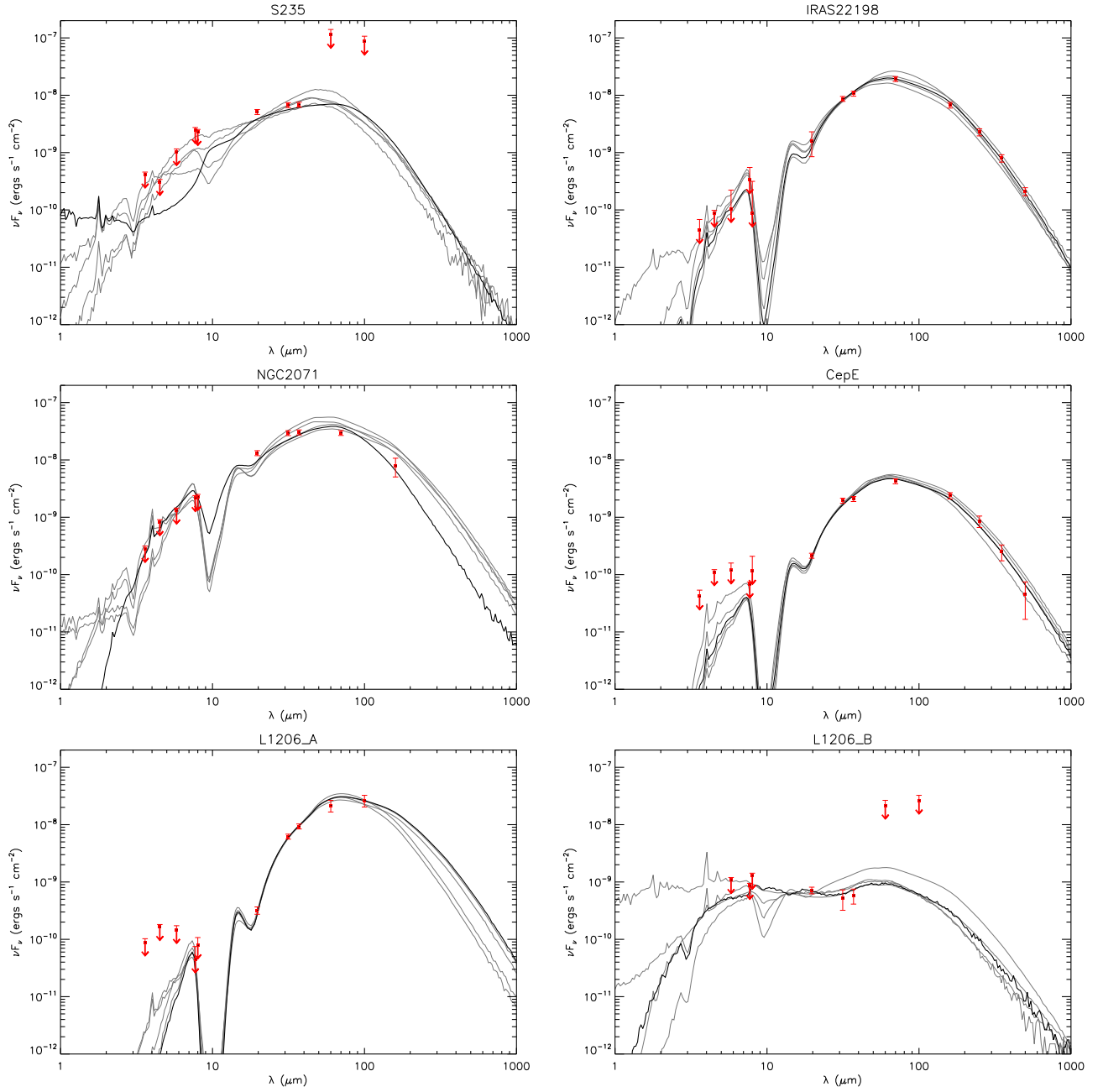


Figure 11. Protostar model fitting to the fixed-aperture background-subtracted SED data using the ZT model grid. For each source, the best-fit model is shown with a solid black line and the next four best models are shown with solid gray lines. The flux values are those from Table 2. Note that the data at $\lesssim 8 \mu\text{m}$ are treated as upper limits (see text). The resulting model parameter results are listed in Table 3.

accretion rates $\dot{m}_* \sim 10^{-5}$ – $10^{-4} M_\odot \text{ yr}^{-1}$, initial core masses M_c ranging from 10 to $480 M_\odot$, clump mass surface densities Σ_{cl} ranging from 0.1 to 3.2 g cm^{-2} , and isotropic luminosities $L_{\text{bol,iso}} \sim 10$ – a few $\times 10^2 L_\odot$. However, given the estimated remaining envelope masses around these protostars, for many models the final outcome would be a massive star because star formation efficiencies are typically $\sim 50\%$ in the models (see also Tanaka et al. 2017; Staff et al. 2019).

Considering the remaining sources, we see that Cep E, IRAS22172 MIR1, IRAS21391 BIMA2, and IRAS21391 BIMA3 are likely to currently be low-mass protostars, with most models returning protostellar masses $m_* \sim 0.5 - 2 M_\odot$, accretion rates $\dot{m}_* \sim 10^{-5}$ – $10^{-4} M_\odot \text{ yr}^{-1}$, initial core masses

M_c ranging from 10 to $160 M_\odot$, clump mass surface densities Σ_{cl} ranging from 0.1 to 0.3 g cm^{-2} , and isotropic luminosities $L_{\text{bol,iso}} \sim 10^2 L_\odot$. Given that the models used for the fitting all have initial core masses of $10 M_\odot$ or greater, then the outcome of the evolution would always be formation of at least IM stars. However, within the degeneracies of the model fits, there are some solutions that would imply that we are catching a massive star at the very earliest stages of its formation.

Below we describe the fitting results of each individual source and then compare them with previous estimates from the literature.

S235: From the best five model fits, this source has an estimated isotropic bolometric luminosity of ~ 1 to

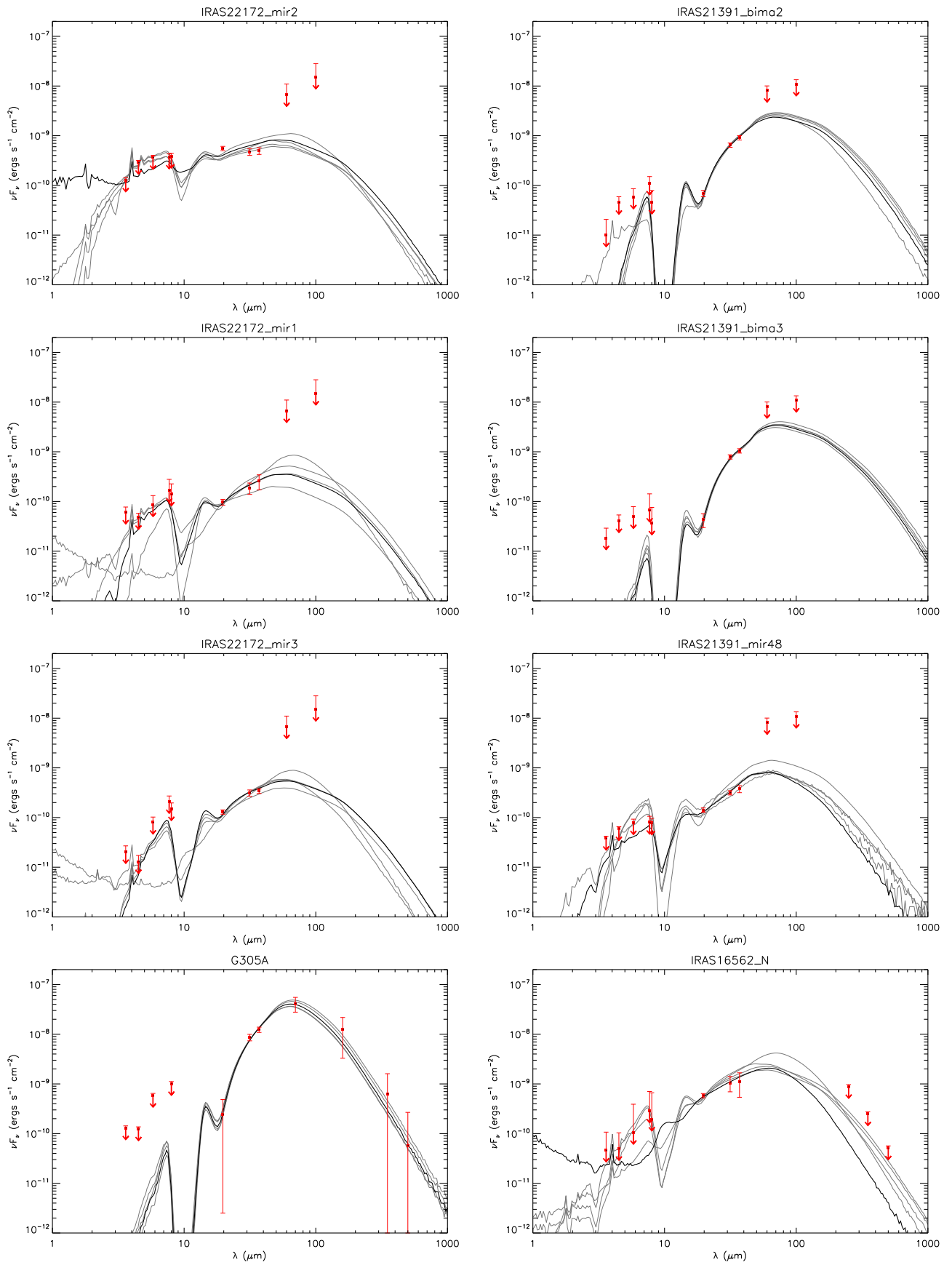


Figure 11. (Continued.)

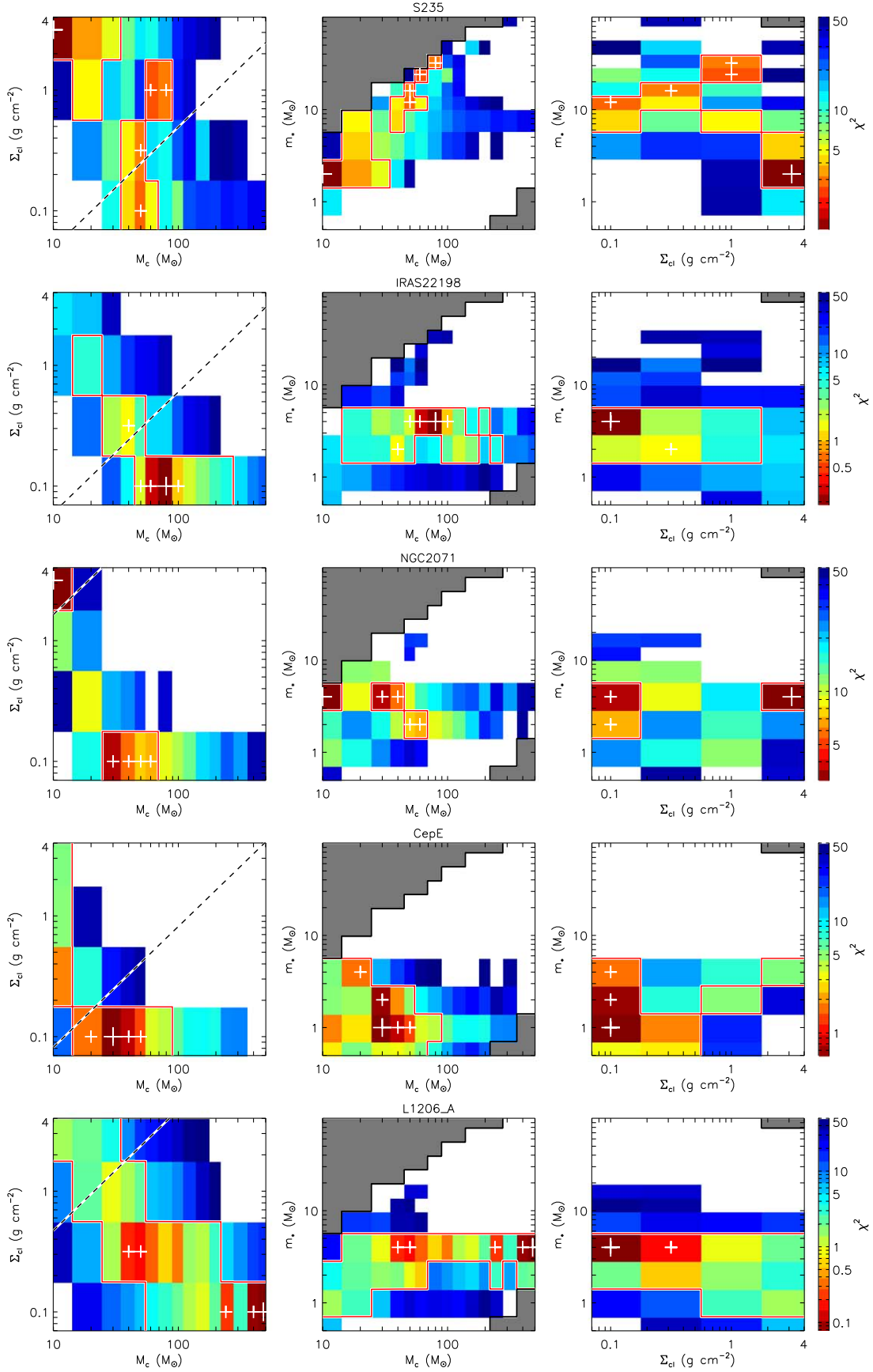


Figure 12. Diagrams of χ^2 distribution in $\Sigma_{\text{cl}} - M_c$ space, $m_* - M_c$ space, and $m_* - \Sigma_{\text{cl}}$ space. The white crosses mark the locations of the five best models, and the large cross is the best model. The gray regions are not covered by the model grid, and the white regions are where the χ^2 is larger than 50. The red contours are at the level of $\chi^2 = \chi^2_{\text{min}} + 5$. The dashed line denotes when $R_c = R_{\text{ap}}$.

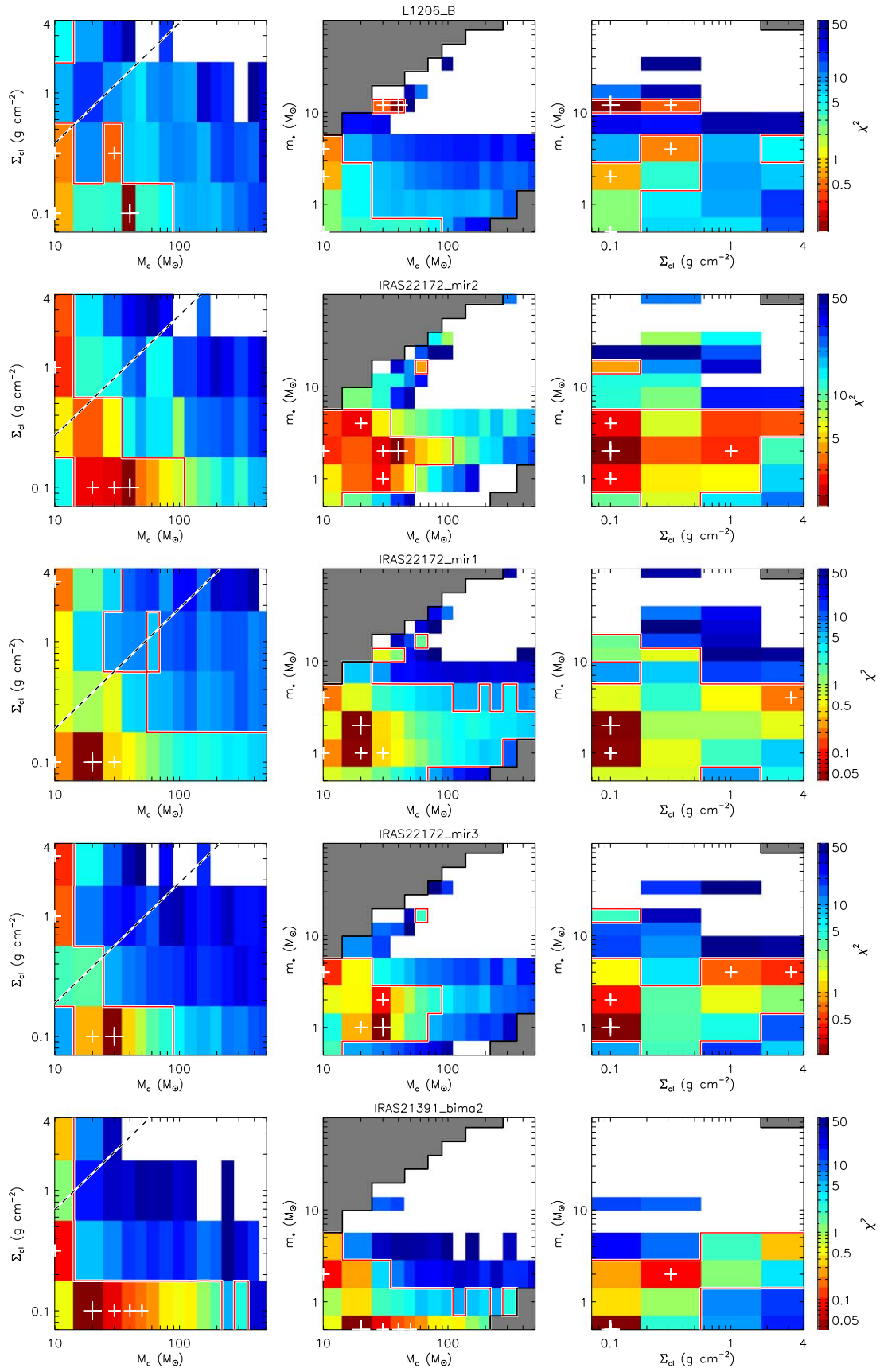


Figure 12. (Continued.)

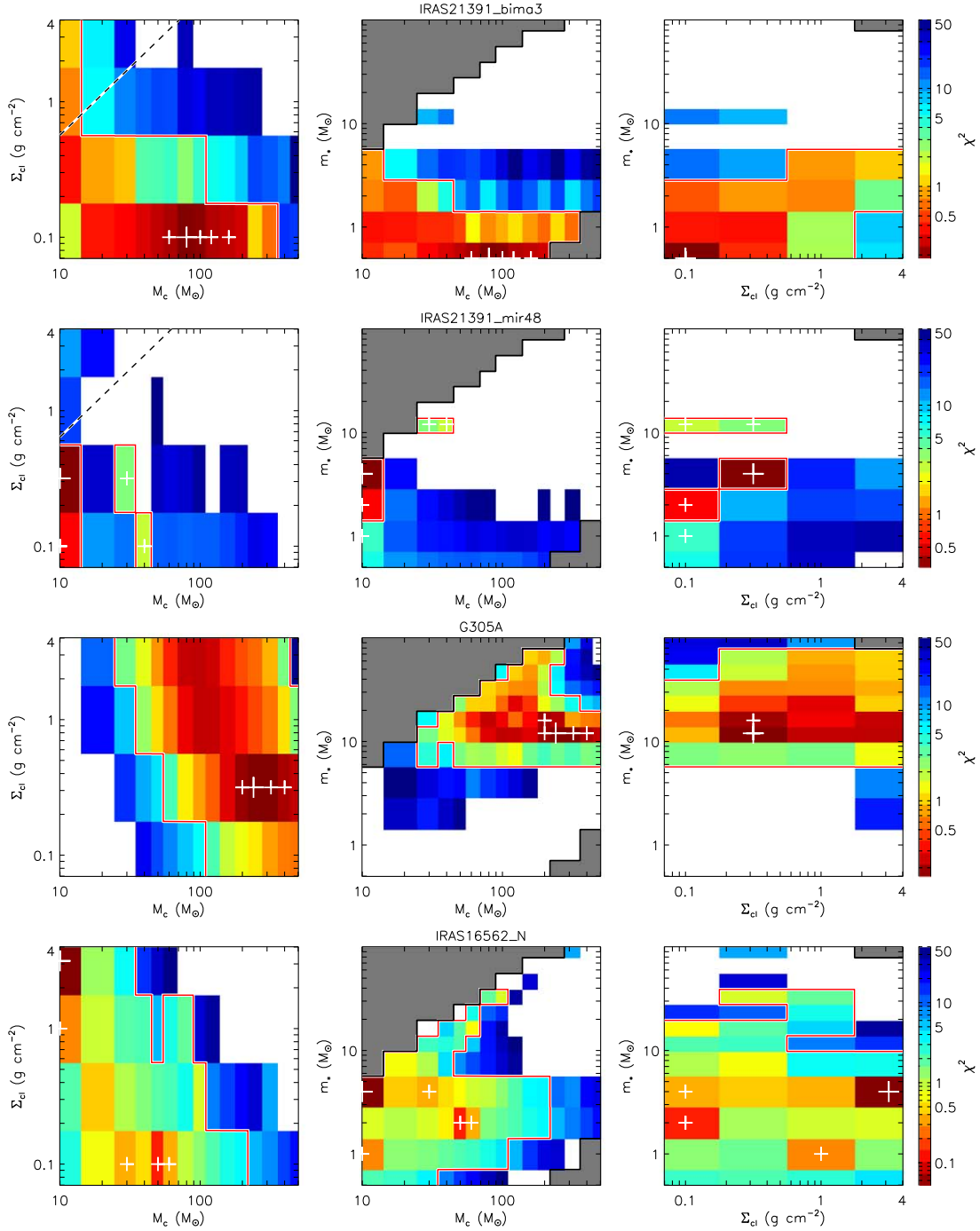


Figure 12. (Continued.)

$2 \times 10^3 L_{\odot}$. However, the intrinsic bolometric luminosity of these models spans a much wider range from 3×10^3 to $2 \times 10^5 L_{\odot}$. We note that for this source there are effectively only three measurements of the SED, all from the SOFIA FORCAST data, with observations at other wavelengths being used as upper limits. The high intrinsic luminosities for this source are possible because of the “flashlight effect,” i.e., most of the flux is not directed toward us due to high local extinction in the core. This range of intrinsic luminosities means that there is a wide range of protostellar properties that are consistent with the observed SED, i.e., there are significant degeneracies in the derived protostellar parameters (see Figure 12). In

particular, while the best-fit model has a low initial core mass ($10 M_{\odot}$) and current protostellar mass ($2 M_{\odot}$) forming from a high Σ_{cl} environment (3 g cm^{-2}) that is viewed at a relatively small angle to the outflow axis, the next four best models are all with larger core and protostellar masses in lower density environments viewed at angles nearly orthogonal to the outflow axis, i.e., close to the equatorial plane where there would be the highest line-of-sight extinction.

In previous studies of S235, Felli et al. (2006) used *JHK* band images and MSX fluxes and derived a luminosity of $410 L_{\odot}$, which they claimed must be considered to be a lower limit because the FIR part of the spectrum is not taken into

Table 3
Parameters of the Best Five Fitted Models

Source	χ^2	M_c (M_\odot)	Σ_{cl} ($g\ cm^{-2}$)	R_{core} (pc) ($''$)	m_* (M_\odot)	θ_{view} ($^\circ$)	A_V (mag)	M_{env} (M_\odot)	$\theta_{w,esc}$ (deg)	\dot{M}_{disk} (M_\odot/yr)	$L_{bol,iso}$ (L_\odot)	L_{bol} (L_\odot)
S235	1.26	10	3.2	0.013 (2)	2.0	39	0.0	6	35	1.8×10^{-4}	1.4×10^3	2.6×10^3
$d = 1.8\ kpc$	2.55	60	1.0	0.057 (7)	24.0	89	11.1	5	71	1.9×10^{-4}	2.1×10^3	9.3×10^4
$R_{ap} = 12''$	2.74	50	0.1	0.165 (19)	12.0	89	4.0	15	59	3.4×10^{-5}	1.4×10^3	1.4×10^4
$=0.10\ pc$	3.00	80	1.0	0.066 (8)	32.0	89	15.2	3	79	1.4×10^{-4}	1.6×10^3	1.6×10^5
	3.02	50	0.3	0.093 (11)	16.0	80	0.0	8	68	7.1×10^{-5}	1.4×10^3	3.1×10^4
IRAS22198	0.18	80	0.1	0.208 (56)	4.0	89	29.3	71	18	3.7×10^{-5}	6.0×10^2	8.5×10^2
$d = 0.8\ kpc$	0.27	60	0.1	0.180 (49)	4.0	62	41.4	51	21	3.4×10^{-5}	6.1×10^2	8.9×10^2
$R_{ap} = 26''$	1.08	100	0.1	0.233 (63)	4.0	89	35.4	91	15	4.0×10^{-5}	6.5×10^2	8.8×10^2
$=0.09\ pc$	1.47	40	0.3	0.083 (22)	2.0	22	9.1	35	17	5.3×10^{-5}	6.5×10^2	7.5×10^2
	1.78	50	0.1	0.165 (44)	4.0	62	25.3	41	24	3.2×10^{-5}	5.1×10^2	7.9×10^2
NGC2071	3.14	10	3.2	0.013 (7)	4.0	58	57.6	2	56	1.9×10^{-4}	5.0×10^2	1.9×10^3
$d = 0.4\ kpc$	3.59	30	0.1	0.127 (67)	4.0	65	12.1	21	33	2.7×10^{-5}	3.6×10^2	7.7×10^2
$R_{ap} = 10''$	5.79	40	0.1	0.147 (78)	4.0	62	11.1	30	27	3.0×10^{-5}	4.4×10^2	7.5×10^2
$=0.02\ pc$	7.06	60	0.1	0.180 (95)	2.0	29	0.0	55	15	2.5×10^{-5}	3.2×10^2	3.5×10^2
	7.57	50	0.1	0.165 (87)	2.0	29	0.0	46	16	2.4×10^{-5}	2.8×10^2	3.1×10^2
CepE	0.63	30	0.1	0.127 (36)	1.0	83	29.3	27	15	1.5×10^{-5}	1.3×10^2	1.7×10^2
$d = 0.7\ kpc$	0.70	30	0.1	0.127 (36)	2.0	65	60.6	25	23	2.0×10^{-5}	1.5×10^2	2.4×10^2
$R_{ap} = 23''$	0.80	40	0.1	0.147 (42)	1.0	89	21.2	38	12	1.6×10^{-5}	1.3×10^2	1.7×10^2
$=0.08\ pc$	1.40	50	0.1	0.165 (46)	1.0	89	19.2	48	11	1.7×10^{-5}	1.4×10^2	1.7×10^2
	1.67	20	0.1	0.104 (29)	4.0	71	100.0	10	43	2.1×10^{-5}	1.9×10^2	6.8×10^2
L1206 A	0.08	480	0.1	0.510 (136)	4.0	89	45.5	474	6	6.1×10^{-5}	9.2×10^2	1.0×10^3
$d = 0.8\ kpc$	0.09	400	0.1	0.465 (124)	4.0	83	56.6	390	7	5.8×10^{-5}	9.4×10^2	1.0×10^3
$R_{ap} = 9''$	0.17	50	0.3	0.093 (25)	4.0	55	41.4	41	22	7.7×10^{-5}	8.8×10^2	1.4×10^3
$=0.03\ pc$	0.21	40	0.3	0.083 (22)	4.0	89	28.3	31	25	7.2×10^{-5}	7.3×10^2	1.4×10^3
	0.23	240	0.1	0.360 (96)	4.0	89	74.7	229	9	5.1×10^{-5}	9.0×10^2	1.0×10^3
L1206 B	0.13	40	0.1	0.147 (39)	12.0	89	8.1	2	82	9.5×10^{-6}	5.7×10^1	1.1×10^4
$d = 0.8\ kpc$	0.45	30	0.3	0.072 (19)	12.0	89	30.3	1	81	2.2×10^{-5}	7.0×10^1	1.2×10^4
$R_{ap} = 10''$	0.55	10	0.3	0.041 (11)	4.0	77	0.0	1	68	2.4×10^{-5}	4.9×10^1	6.7×10^2
$=0.04\ pc$	0.71	10	0.1	0.074 (20)	2.0	51	0.0	4	50	1.1×10^{-5}	8.1×10^1	1.3×10^2
	2.26	10	0.1	0.074 (20)	0.5	22	34.3	9	20	7.8×10^{-6}	1.5×10^2	7.5×10^1
IRAS22172 MIR2	1.67	40	0.1	0.147 (13)	2.0	22	0.0	36	19	2.2×10^{-5}	3.9×10^2	2.7×10^2
$d = 2.4\ kpc$	2.27	30	0.1	0.127 (11)	2.0	22	32.3	25	23	2.0×10^{-5}	8.0×10^2	2.4×10^2
$R_{ap} = 4''$	2.39	20	0.1	0.104 (9)	4.0	48	6.1	10	43	2.1×10^{-5}	3.4×10^2	6.8×10^2
$=0.04\ pc$	2.51	30	0.1	0.127 (11)	1.0	13	37.4	27	15	1.5×10^{-5}	8.7×10^2	1.7×10^2
	2.81	10	1.0	0.023 (2)	2.0	39	50.5	5	39	7.5×10^{-5}	1.0×10^3	7.6×10^2
IRAS22172 MIR1	0.04	20	0.1	0.104 (9)	2.0	34	25.3	15	30	1.7×10^{-5}	1.4×10^2	1.9×10^2
$d = 2.4\ kpc$	0.04	20	0.1	0.104 (9)	1.0	22	50.5	17	20	1.3×10^{-5}	2.7×10^2	1.5×10^2
$R_{ap} = 5''$	0.20	10	3.2	0.013 (1)	4.0	71	0.0	2	56	1.9×10^{-4}	1.9×10^2	1.9×10^3
$=0.05\ pc$	0.23	10	0.1	0.074 (6)	1.0	34	1.0	7	31	1.0×10^{-5}	8.1×10^1	1.1×10^2
	0.40	30	0.1	0.127 (11)	1.0	22	16.2	27	15	1.5×10^{-5}	1.7×10^2	1.7×10^2
IRAS22172 MIR3	0.19	30	0.1	0.127 (11)	1.0	22	0.0	27	15	1.5×10^{-5}	1.7×10^2	1.7×10^2
$d = 2.4\ kpc$	0.39	30	0.1	0.127 (11)	2.0	34	13.1	25	23	2.0×10^{-5}	1.9×10^2	2.4×10^2
$R_{ap} = 5''$	0.45	10	3.2	0.013 (1)	4.0	68	0.0	2	56	1.9×10^{-4}	2.1×10^2	1.9×10^3
$=0.05\ pc$	0.61	10	1.0	0.023 (2)	4.0	68	0.0	1	59	7.7×10^{-5}	1.5×10^2	1.1×10^3
	0.97	20	0.1	0.104 (9)	1.0	29	0.0	17	20	1.3×10^{-5}	1.2×10^2	1.5×10^2
IRAS21391 BIMA2	0.04	20	0.1	0.104 (29)	0.5	34	74.7	19	13	9.6×10^{-6}	8.0×10^1	9.0×10^1
$d = 0.8\ kpc$	0.07	30	0.1	0.127 (35)	0.5	22	74.7	29	10	1.1×10^{-5}	8.8×10^1	9.0×10^1
$R_{ap} = 8''$	0.08	10	0.3	0.041 (11)	2.0	71	19.2	5	43	3.0×10^{-5}	6.2×10^1	2.8×10^2
$=0.03\ pc$	0.14	40	0.1	0.147 (40)	0.5	22	59.6	39	8	1.1×10^{-5}	8.7×10^1	8.8×10^1
	0.18	50	0.1	0.165 (45)	0.5	22	48.5	49	7	1.2×10^{-5}	8.7×10^1	8.7×10^1
IRAS21391 BIMA3	0.18	80	0.1	0.208 (57)	0.5	86	2.0	79	5	1.4×10^{-5}	8.6×10^1	9.2×10^1
$d = 0.8\ kpc$	0.20	100	0.1	0.233 (64)	0.5	55	0.0	99	4	1.5×10^{-5}	8.9×10^1	9.1×10^1
$R_{ap} = 8''$	0.23	60	0.1	0.180 (50)	0.5	83	9.1	59	6	1.3×10^{-5}	8.0×10^1	8.7×10^1
$=0.03\ pc$	0.24	120	0.1	0.255 (70)	0.5	22	0.0	118	4	1.5×10^{-5}	9.0×10^1	8.8×10^1
	0.26	160	0.1	0.294 (81)	0.5	22	0.0	158	3	1.6×10^{-5}	1.0×10^2	9.8×10^1

Table 3
(Continued)

Source	χ^2	M_c (M_\odot)	Σ_{cl} (g cm^{-2})	R_{core} (pc) ($''$)	m_* (M_\odot)	θ_{view} ($^\circ$)	A_V (mag)	M_{env} (M_\odot)	$\theta_{w,esc}$ (deg)	\dot{M}_{disk} (M_\odot/yr)	$L_{bol,iso}$ (L_\odot)	L_{bol} (L_\odot)
IRAS21391 MIR48	0.33	10	0.3	0.041 (11)	4.0	89	43.4	1	68	2.4×10^{-5}	2.9×10^1	6.7×10^2
$d = 0.8$ kpc	0.58	10	0.1	0.074 (20)	2.0	68	13.1	4	50	1.1×10^{-5}	2.5×10^1	1.3×10^2
$R_{ap} = 8''$	2.70	40	0.1	0.147 (40)	12.0	89	98.0	2	82	9.5×10^{-6}	5.7×10^1	1.1×10^4
$=0.03$ pc	3.75	30	0.3	0.072 (20)	12.0	89	100.0	1	81	2.2×10^{-5}	7.0×10^1	1.2×10^4
	5.51	10	0.1	0.074 (20)	1.0	39	92.9	7	31	1.0×10^{-5}	6.4×10^1	1.1×10^2
G305 A	0.16	240	0.3	0.203 (10)	12.0	83	85.9	216	15	2.0×10^{-4}	3.1×10^4	4.1×10^4
$d = 4.1$ kpc	0.17	320	0.3	0.234 (12)	12.0	71	79.8	293	13	2.2×10^{-4}	3.3×10^4	4.0×10^4
$R_{ap} = 12''$	0.19	200	0.3	0.185 (9)	12.0	80	81.8	173	17	1.9×10^{-4}	2.8×10^4	4.0×10^4
$=0.24$ pc	0.20	200	0.3	0.185 (9)	16.0	83	97.0	162	22	2.2×10^{-4}	3.0×10^4	5.3×10^4
	0.20	400	0.3	0.262 (13)	12.0	22	90.9	373	11	2.3×10^{-4}	3.7×10^4	4.0×10^4
IRAS16562 N	0.05	10	3.2	0.013 (2)	4.0	62	0.0	2	56	1.9×10^{-4}	2.9×10^2	1.9×10^3
$d = 1.7$ kpc	0.14	50	0.1	0.165 (20)	2.0	22	0.0	46	16	2.4×10^{-5}	3.1×10^2	3.1×10^2
$R_{ap} = 8''$	0.28	10	1.0	0.023 (3)	1.0	29	17.2	8	25	6.0×10^{-5}	5.6×10^2	7.7×10^2
$=0.06$ pc	0.37	60	0.1	0.180 (22)	2.0	22	0.0	55	15	2.5×10^{-5}	3.5×10^2	3.5×10^2
	0.38	30	0.1	0.127 (15)	4.0	62	7.1	21	33	2.7×10^{-5}	3.8×10^2	7.7×10^2

(This table is available in machine-readable form.)

account in their calculation. Dewangan & Anandarao (2011) used *JHK* band images and 2MASS and IRAC fluxes to do SED fitting with models from Robitaille et al. (2006, 2007). They derived $m_* \sim 6.5 M_\odot$, $L_{bol} \sim 575 L_\odot$, and $M_{env} \sim 9 M_\odot$. The stellar source itself has been classified as a B1V star by Boley et al. (2009), with emission-line profiles indicative of an accretion disk. Based on the intensity of the reflected component, it was concluded that the accretion disk must be viewed nearly edge-on, which agrees with four of our best models and explains the discrepancy between $L_{bol,iso}$ and L_{bol} . Boley et al. (2009) estimated a mass accretion rate of $2\text{--}6 \times 10^{-6} M_\odot \text{yr}^{-1}$ for a B1V star with a mass of $13 M_\odot$ using the $\text{Br}\gamma$ luminosity, which is comparable with the mass-loss rate of $4 \times 10^{-6} M_\odot \text{yr}^{-1}$ derived by Felli et al. (2006) from the radio flux density. However, our best models have disk accretion rates more than 10 times higher. It should be noted that the accretion rate is not a free parameter in the ZT models and that the range of accretion rates is generally relatively high, being set by the properties of the initial cores and the mass surface density of their clump environments.

IRAS 22198: The best models are those with a protostar with current mass of $2\text{--}4 M_\odot$, forming in a low-mass surface density clump ($0.1\text{--}0.3 \text{ g cm}^{-2}$). Our estimate of the isotropic luminosity is about $600 L_\odot$, with the intrinsic luminosity being about $800 L_\odot$. Sánchez-Monge et al. (2010) fit the SED of IRAS 22198 from NIR to cm wavelengths with a modified blackbody plus a thermal ionized wind and derived a bolometric luminosity of $\sim 370 L_\odot$ and an envelope mass of $\sim 5 M_\odot$, remarking that the SED of IRAS 22198 resembles that of Class 0 objects (Andre et al. 1993). Our derived isotropic luminosity is slightly higher, while our envelope mass is much higher, $\sim 50 M_\odot$, than their results. However, their M_{env} was derived from interferometric flux measurements and thus should be treated as a lower limit. The single-dish measurement at mm wavelengths of the dense core mass is $17 M_\odot$ within a radius of $2,650 \text{ au}$ ($3.5''$) (Palau et al. 2013). Thus the reason for our higher mass estimate is likely due to our analysis applying to a much larger scale, i.e., within a radius of 0.089 pc ($26''$).

NGC 2071: The best models suggest a currently IM protostar with a mass of $2\text{--}4 M_\odot$ forming within a core with

initial mass of $10\text{--}60 M_\odot$. Trinidad et al. (2009) estimated a central mass of $\sim 5 \pm 3 M_\odot$ for IRS1 and $\sim 1.2 \pm 0.4 M_\odot$ for IRS3 based on the observed velocity gradient of the water masers, which is consistent with our estimate. The single-dish measurement at mm wavelength of the dense core mass is $39 M_\odot$ within a radius of $4,700 \text{ au}$ ($11''$) (Palau et al. 2013), which is similar to the M_{env} returned by most of our best-fit models inside $10''$.

Cep E: The best five models all return a Σ_{cl} of 0.1 g cm^{-2} , and most models have m_* as low as $1\text{--}2 M_\odot$. Crimier et al. (2010) modeled the MIR to mm SED with the 1D RT code DUSTY and derived a luminosity of $\sim 100 L_\odot$ and an envelope mass of $35 M_\odot$, which are similar to our results.

L1206: The best models of L1206 A involve a protostar forming inside a relatively massive initial core ($40\text{--}480 M_\odot$) with low clump mass surface density ($0.1\text{--}0.3 \text{ g cm}^{-2}$). All the best five models give a value of $m_* = 4 M_\odot$. Ressler & Shure (1991) found a total luminosity of $1100 L_\odot$ by fitting four IRAS fluxes plus the 2.7 mm data of Wilking et al. (1989) with a single-temperature dust spectrum at 1 kpc , which is similar to our result. Beltrán et al. (2006) estimated the core mass of OVRO 2 to be $14.2 M_\odot$ from the 2.7 mm dust continuum emission at a distance of 910 pc . This core mass estimate is derived from interferometric observations that may be missing flux, and indeed, three of our best-fit models give a much higher value of M_{env} . Ressler & Shure (1991) suggested that L1206 A is seen only in scattered light because of heavy obscuration by an almost edge-on circumstellar disk. Four of the best five models return a nearly edge-on line of sight.

L1206 B has a very flat and slightly decreasing SED at short wavelengths. A circumstellar disk could explain the IR excess, as suggested by Ressler & Shure (1991), and the protostar may have already cleared a significant portion of its envelope, thus explaining the decreasing spectrum between 10 and $30 \mu\text{m}$. The favored ZT models have a wide range of stellar mass $m_* \sim 0.5\text{--}12 M_\odot$, but low initial core mass $M_c \sim 10\text{--}40 M_\odot$, low current envelope mass of 1 to $9 M_\odot$, and low-mass surface density $\Sigma_{cl} \sim 0.1\text{--}0.3 \text{ g cm}^{-2}$ of the clump environment.

IRAS 22172: The models for the three MIR sources all involve protostars with masses $\sim 1\text{--}4 M_\odot$ forming in relatively

low-mass initial cores of $10\text{--}40 M_{\odot}$. Fontani et al. (2004) divided the SED between the NIR cluster and the cold 3.4 mm core (their I22172-C) and performed two graybody fits to the SED. The graybody fit to the *MSX* and *IRAS* data with $\lambda \leq 25 \mu\text{m}$, which represent the emission due to the cluster of stars surrounding the mm core I22172-C, yields a luminosity of $2.2 \times 10^2 L_{\odot}$. Based on the beam size and the *MSX* 21 μm emission, their photometry should cover the whole field, i.e., all the three MIR sources. However, in our analysis we derive a much higher combined luminosity from the region, with contributions from the three MIR sources analyzed. The single-dish measurement at mm wavelengths of the dense core mass of MIR2 is $150 M_{\odot}$ (Palau et al. 2013), much higher than the M_{env} given by our models. However, their core radius, represented by the deconvolved half-width at half maximum, is about $10''$, while our mass estimate is based on an aperture radius of $4''$.

IRAS 21391: Previous SED fitting with low-resolution data estimated the bolometric luminosity of IRAS 21391 to range from $235 L_{\odot}$ (Saraceno et al. 1996) to $440 L_{\odot}$ (Sugitani et al. 2000). Our fitting results for the three sources BIMA 2, BIMA 3 and MIR 48¹³ all return isotropic luminosities $\lesssim 100 L_{\odot}$. Using the relationship between the momentum rate and the bolometric luminosity (Cabrit & Bertout 1992), Beltrán et al. (2002) inferred a bolometric luminosity of $150 L_{\odot}$ for BIMA 2.

Choudhury et al. (2010) fit the $1\text{--}24 \mu\text{m}$ SED derived from optical BVRI, Spitzer IRAC, and MIPS observations with Robitaille et al. (2007) models and derived a luminosity of $197 L_{\odot}$ and a stellar mass of $6 M_{\odot}$ for BIMA 2 (their MIR-50), which are both higher than our results. As indicated by Figure 17, ZT models with m_* higher than $5 M_{\odot}$ have a very large χ^2 . The envelope mass of Choudhury et al. (2010) of $41 M_{\odot}$ is also slightly higher than the M_c and M_{env} in our first three best models. However, their disk accretion rate is about 1000 times lower than that in our best models, which is a known issue when comparing Robitaille et al. (2007) and ZT models (see the discussion in De Buizer et al. 2017). Beltrán et al. (2002) estimated the circumstellar mass to be $5.1 M_{\odot}$ based on BIMA 3.1 mm continuum observations, which should be treated as a lower limit of M_{env} given that it is an interferometric measurement subject to missing flux. Beltrán et al. (2002) suggested that the axis of the outflow should be close to the plane of the sky, given the morphology of the CO(1–0) outflows at low velocities with blueshifted and redshifted gas in both lobes. However, in our best five models, only the third model has a more edge-on inclination.

Our best models for IRAS 21391 BIMA3 involve a protostar with a current stellar mass of $0.5 M_{\odot}$ with a bolometric luminosity $\sim 100 L_{\odot}$. The best-fit model in Choudhury et al. (2010) for BIMA 3 (their MIR-54) yields a luminosity of $33.4 L_{\odot}$ and a stellar mass of $1.5 M_{\odot}$. Beltrán et al. (2002) derived a circumstellar mass of $0.07 M_{\odot}$ for BIMA 3, which is much lower than the predicted M_{env} by our best models.

Our best models for IRAS 21391 MIR48 involve a protostar with a mass ranging from 1 to $12 M_{\odot}$. The best-fit model in Choudhury et al. (2010) for MIR-48 yields a luminosity of $280 L_{\odot}$ and a stellar mass of $5 M_{\odot}$, which is similar to the isotropic luminosity and the stellar mass in our best two models.

G305 A: The best models are those with a high-mass protostar with a current mass of $12\text{--}16 M_{\odot}$ forming from a core with initial mass of $200\text{--}400 M_{\odot}$ and initial clump mass surface density of 0.3 g cm^{-2} . In Paper II we mentioned that G305A is likely to be much younger and more embedded than G305B and in a hot core phase, prior to the onset of a UC H II region.

IRAS16562 N: The best models involve a low-mass protostar with current mass of $1\text{--}4 M_{\odot}$ forming from a core with an initial mass of $10\text{--}60 M_{\odot}$. Σ_{cl} is not well constrained; it varies from 0.1 to 3.2 g cm^{-2} .

Figure 12 shows the χ^2 distribution in $\Sigma_{\text{cl}} - M_c$ space, $m_* - M_c$ space, and $m_* - \Sigma_{\text{cl}}$ space for the 14 sources. As also discussed in Paper II, these diagrams illustrate the full constraints in the primary parameter space derived by fitting the SED data, and the possible degeneracies. In general, all the three parameters span a larger range compared with the sources of Papers I and II.

Follow-up observations and analysis of SOMA sources can be helpful in breaking degeneracies that arise from simple SED fitting. One example of such follow-up work is that of Rosero et al. (2019), who examined cm radio continuum data of the SOMA sources presented in Paper I. Radio free-free emission from photoionized gas, first expected to be present in the outflow cavity, is particularly useful for constraining the mass of the protostar once it reaches $\gtrsim 10 M_{\odot}$ and begins to contract to the zero-age main sequence. However, at lower masses, most of the ionization associated with the source is expected to be due to shock ionization, e.g., due to internal shocks in the outflow (see also Fedriani et al. 2019). Quantitative models for the amount of shock ionization and associated radio emission have not yet been developed for the ZT protostellar models. For the mainly IM sources presented in this paper, we anticipate that cm radio emission will mainly be due to shock ionization, so such observations may be more challenging to interpret to help break SED fit degeneracies. On the other hand, measurements of protostellar outflow properties, including cavity opening angle and mass and momentum fluxes, may provide more diagnostic power.

In contrast with the high-mass protostars in Papers I and II, the best models ($\chi^2 - \chi_{\text{min}}^2 < 5$, within the red contours shown in Figure 12) of the IM protostars also occupy the region with lower M_c at lower Σ_{cl} . Another striking feature is that most sources have best models with a core size larger than the aperture size, i.e., they appear below the dashed line that denotes when $R_c = R_{\text{ap}}$ in Figure 12. To examine this matter further, we analyzed the image profiles of the best five models of the sources and found that the flux density at $37 \mu\text{m}$ usually decays to 10^{-3} of the peak flux density within $5''$ from the center and the flux density at $70 \mu\text{m}$ usually decays to 10^{-3} of the peak flux density within $15''$ from the center. The typical aperture radius is $\sim 10''$ (except for the three sources in IRAS 22172, where it is $\sim 5''$, but in their best models the flux density decays to 10^{-3} of the peak within $2''$ and $5''$ at 37 and $70 \mu\text{m}$, respectively). This indicates that when the models have a core size larger than the aperture used for measuring the SED, only a small amount of the total flux from the model is being missed (however, the proportion of missed flux would be larger at longer wavelengths). Nevertheless, to better illustrate the importance of this effect, in the following discussion we present two cases, i.e., with and without the constraint that the model core size needs to be within a factor of two of the aperture size.

¹³ Note that we follow the nomenclature in Beltrán et al. (2002), but the photometry centers of IRAS 21391 BIMA2 and IRAS 21391 BIMA3 are VLA2 and VLA3, respectively.

Table 4
Average Parameters of SOMA Protostars

Source	M_c	Σ_{cl}	m_*	m_*/M_c	M_{env}	$L_{bol,iso}$	L_{bol}	θ_{view}	$\theta_{w,esc}$	$\theta_{view}/\theta_{w,esc}$	α_{19-37}
	(M_\odot)	($g\ cm^{-2}$)	(M_\odot)		(M_\odot)	(L_\odot)	(L_\odot)	($^\circ$)	($^\circ$)		
G45.12+0.13	403	2.0	35.5	0.09	319	7.2e+05	4.6e+05	24	21	1.12	1.05
	403	2.0	35.5	0.09	319	7.2e+05	4.6e+05	24	21	1.12	1.05
G309.92+0.48	323	2.0	33.5	0.10	251	3.3e+05	4.2e+05	30	22	1.37	2.04
	323	2.0	33.5	0.10	251	3.3e+05	4.2e+05	30	22	1.37	2.04
G35.58-0.03	427	2.0	33.5	0.08	350	3.1e+05	4.2e+05	29	19	1.63	4.03
	427	2.0	33.5	0.08	350	3.1e+05	4.2e+05	29	19	1.63	4.03
IRAS16562	323	0.3	22.9	0.07	263	7.7e+04	1.1e+05	43	23	1.90	2.91
	323	0.3	22.9	0.07	263	7.7e+04	1.1e+05	43	23	1.90	2.91
G305.20+0.21	110	2.5	28.5	0.26	51	7.9e+04	2.7e+05	47	38	1.24	0.82
	110	2.5	28.5	0.26	51	7.9e+04	2.7e+05	47	38	1.24	0.82
G49.27-0.34	197	3.2	12.0	0.06	174	4.4e+04	5.1e+04	26	14	1.92	4.38
	197	3.2	12.0	0.06	174	4.4e+04	5.1e+04	26	14	1.92	4.38
G339.88-1.26	298	0.5	12.7	0.04	269	3.8e+04	4.6e+04	36	14	2.70	5.00
	298	0.5	12.7	0.04	269	3.8e+04	4.6e+04	36	14	2.70	5.00
G45.47+0.05	260	1.3	32.8	0.13	187	1.0e+05	3.1e+05	77	27	2.80	3.01
	260	1.3	32.8	0.13	187	1.0e+05	3.1e+05	77	27	2.80	3.01
CepA	188	0.3	14.6	0.08	148	2.4e+04	4.4e+04	62	24	3.05	5.03
	132	0.5	14.6	0.11	98	2.6e+04	5.1e+04	52	26	1.96	5.03
IRAS20126	109	0.3	15.5	0.14	67	1.3e+04	4.1e+04	67	35	2.14	2.54
	95	0.3	17.8	0.19	49	1.2e+04	5.5e+04	67	42	1.60	2.54
AFGL4029	65	0.3	16.8	0.26	17	5.4e+03	4.5e+04	70	54	1.35	2.09
	65	0.3	16.8	0.26	17	5.4e+03	4.5e+04	70	54	1.35	2.09
NGC7538_IRS9	245	0.2	16.4	0.07	196	3.6e+04	4.7e+04	31	22	1.44	1.52
	245	0.2	16.4	0.07	196	3.6e+04	4.7e+04	31	22	1.44	1.52
G35.20-0.74	190	0.5	14.6	0.08	154	3.5e+04	5.1e+04	42	20	2.07	3.53
	190	0.5	14.6	0.08	154	3.5e+04	5.1e+04	42	20	2.07	3.53
AFGL437	133	0.2	16.4	0.12	80	1.7e+04	4.2e+04	60	36	1.64	0.86
	133	0.2	16.4	0.12	80	1.7e+04	4.2e+04	60	36	1.64	0.86
IRAS07299	206	0.1	10.8	0.05	168	1.0e+04	1.8e+04	83	21	4.85	2.51
	71	0.8	11.7	0.16	44	1.2e+04	3.2e+04	57	32	1.77	2.51
S235	41	0.6	12.4	0.30	6	1.5e+03	2.8e+04	77	62	1.23	0.46
	41	0.6	12.4	0.30	6	1.5e+03	2.8e+04	77	62	1.23	0.46
IRAS22198	63	0.1	3.5	0.06	55	6.0e+02	8.3e+02	65	19	3.52	3.03
	43	0.2	3.5	0.08	34	6.7e+02	9.7e+02	43	23	1.86	3.03
NGC2071	32	0.2	3.0	0.09	19	3.7e+02	6.5e+02	49	29	1.80	1.32
	10	3.2	4.0	0.40	2	5.0e+02	1.9e+03	58	56	1.04	1.32
CepE	32	0.1	1.5	0.05	26	1.5e+02	2.4e+02	79	21	5.05	3.60
	24	0.1	1.5	0.06	18	1.4e+02	2.6e+02	70	24	3.70	3.60
L1206_A	156	0.2	4.0	0.03	140	8.7e+02	1.1e+03	81	14	8.64	5.33
	24	1.6	2.6	0.11	17	1.2e+03	2.2e+03	35	25	1.40	5.33
L1206_B	16	0.2	3.6	0.22	2	7.5e+01	9.7e+02	66	60	1.09	-0.33
	12	0.2	2.2	0.17	3	8.0e+01	3.9e+02	55	50	1.09	-0.33
IRAS22172_mir2	24	0.2	2.0	0.09	17	6.3e+02	3.6e+02	29	28	1.02	-0.17
	11	0.8	2.3	0.20	4	6.7e+02	7.3e+02	40	42	0.92	-0.17
IRAS22172_mir3	18	0.3	2.0	0.11	8	1.6e+02	4.2e+02	44	35	1.35	1.53
	15	0.3	2.6	0.17	6	1.6e+02	5.3e+02	54	42	1.34	1.53
IRAS22172_mir1	16	0.2	1.5	0.09	10	1.6e+02	2.5e+02	37	31	1.22	1.54
	13	0.3	2.0	0.15	5	1.7e+02	3.7e+02	45	39	1.13	1.54

Table 4
(Continued)

Source	M_c	Σ_{cl}	m_*	m_*/M_c	M_{env}	$L_{bol,iso}$	L_{bol}	θ_{view}	$\theta_{w,esc}$	$\theta_{view}/\theta_{w,esc}$	α_{19-37}
IRAS21391_bima2	26	0.1	0.7	0.03	22	8.0e+01	1.1e+02	34	16	2.52	4.07
	10	0.8	2.3	0.23	3	1.2e+02	6.6e+02	73	45	1.64	4.07
IRAS21391_bima3	98	0.1	0.5	0.01	97	8.9e+01	9.1e+01	54	5	11.10	5.03
	10	0.5	1.5	0.15	5	1.1e+02	4.2e+02	62	38	1.68	5.03
IRAS21391_mir48	16	0.2	4.1	0.25	2	4.5e+01	1.0e+03	75	63	1.22	1.54
	10	0.3	4.0	0.40	1	2.9e+01	6.7e+02	89	68	1.30	1.54
G305A	262	0.3	12.7	0.05	231	3.1e+04	4.3e+04	68	16	4.26	6.20
	262	0.3	12.7	0.05	231	3.1e+04	4.3e+04	68	16	4.26	6.20
IRAS16562_N	25	0.3	2.3	0.09	15	3.7e+02	6.5e+02	39	29	1.40	1.01
	13	0.8	3.5	0.26	3	4.1e+02	1.8e+03	57	49	1.15	1.01

Note. The first line of each source shows the average (geometric mean, except for θ_{view} , $\theta_{w,esc}$, and $\theta_{view}/\theta_{w,esc}$, for which arithmetic means are evaluated) of the values of the best five models without any core size versus aperture constraint applied. The second line shows the results of the best five or fewer models with $R_c \leq 2R_{ap}$ and $\chi^2 \leq \chi^2_{min} + 5$.

(This table is available in machine-readable form.)

5. Discussion

We now discuss the results of the global sample of 29 protostars that have been derived from a uniform SED fitting analysis that always includes SOFIA-FORCAST data, as presented in Papers I, II, and III.

In general, we select the best five or fewer models that satisfy $\chi^2 < \chi^2_{min} + 5$, where χ^2_{min} is the value of χ^2 of the best model, and then present averages of the model properties. However, for G45.12+0.13, which was discussed in Paper II as not being especially well fit by the ZT models because of its high luminosity (it is likely to be multiple sources), there is only one model with $\chi^2 < \chi^2_{min} + 5$. Thus for this source we average all the best five models. The model properties are averaged in log space, i.e., geometric averages, except for A_V , θ_{view} , and $\theta_{w,esc}$, which are evaluated as arithmetic means.

Then, as explained at the end of the last section, we also consider two cases, i.e., with and without the constraint that the best-fit models have core sizes that are within a factor of two of the aperture size. Without the core size constraint, the best five models of all sources automatically satisfy $\chi^2 < \chi^2_{min} + 5$, except for G45.12+0.13. With the core size constraint (which we regard as our best fiducial method), there can be cases, especially of IM sources from Paper III (i.e., this work), where there are fewer than five models with $\chi^2 < \chi^2_{min} + 5$. Still, G45.12+0.13 is kept as a special case, as above. The key average source properties are listed in Table 4.

5.1. The SOMA Sample Space

Figure 13(a) shows $L_{bol,iso}$ versus M_{env} for the SOMA protostar sample from Papers I, II, and this work, i.e., Paper III. Figure 13(b) shows L_{bol} versus M_{env} of the same sample. This is the more fundamental property of the protostar because $L_{bol,iso}$ is affected by the orientation of protostellar geometry to our line of sight and the flashlight effect. Compared with the sources presented in Papers I and II, which were exclusively high-mass protostars, $L_{bol,iso}$, L_{bol} , and M_{env} all extend down to lower values. When we apply the constraint on model core sizes, i.e., radii of the models must be no larger than twice the radius of the aperture used to define the SED, then we see from Figure 13 panels (c) and d that there is an apparent tightening

of the correlations between $L_{bol,iso}$ or L_{bol} with M_{env} . Note that YSOs with the highest mass and highest luminosity usually have the best models with $R_c \lesssim R_{ap}$ and are thus less affected by this constraint.

Figure 13 panels (e) and f show the sample distribution in the context of the whole ZT model grid, where lines indicate evolutionary tracks, i.e., from low luminosity and high envelope mass to high luminosity and low envelope mass, for different clump environment mass surface densities, Σ_{cl} .

The SOMA sample spans a relatively broad range of evolutionary stages with L_{bol}/M_{env} extending from $\sim 10 L_{\odot}/M_{\odot}$ up to almost $10^4 L_{\odot}/M_{\odot}$, indicated by the dashed lines in Figure 13 panel (f). As a result of this broad range and given the even wider range that is expected from the theoretical models, we do not fit the observed L_{bol} versus M_{env} distribution with a power-law relation (see Molinari et al. 2008 Urquhart et al. 2018). Rather, we simply note that the sources that have so far been analyzed in the SOMA sample span this wide range of evolutionary stages, but the expected very late stages and very early stages are not especially well represented.

To further explore the evolutionary context of the SOMA protostars, in Figure 14 we show the SOMA sample in the luminosity versus envelope mass plane, together with protostellar sources identified in Infrared Dark Clouds (IRDCs), which are expected to be at earlier stages of evolution. Two samples of protostars selected from IRDC environments are shown, with the source SED construction and ZT model fitting following the same methods as have been used for the SOMA sample. The first, labeled “IRDCs A-H,” is the sample of 28 sources from Liu et al. (2018) and Liu et al. (2020, in preparation), based on ALMA observations of 32 clumps in IRDCs A to H from the sample of Butler & Tan (2009, 2012). The second, labeled “IRDC C,” is a complete census of the protostellar sources in IRDC C carried out by Moser et al. (2020), based on sources identified in the region by Herschel 70 μm emission from the Hi-GAL point source catalog (Molinari et al. 2016). After allowing for a few poorly resolved sources that are treated as a single protostar in the SED modeling, a total of 35 protostars have been analyzed by Moser et al. (2020). The IRDC sources include protostars with intrinsic bolometric luminosities down to about $100 L_{\odot}$,

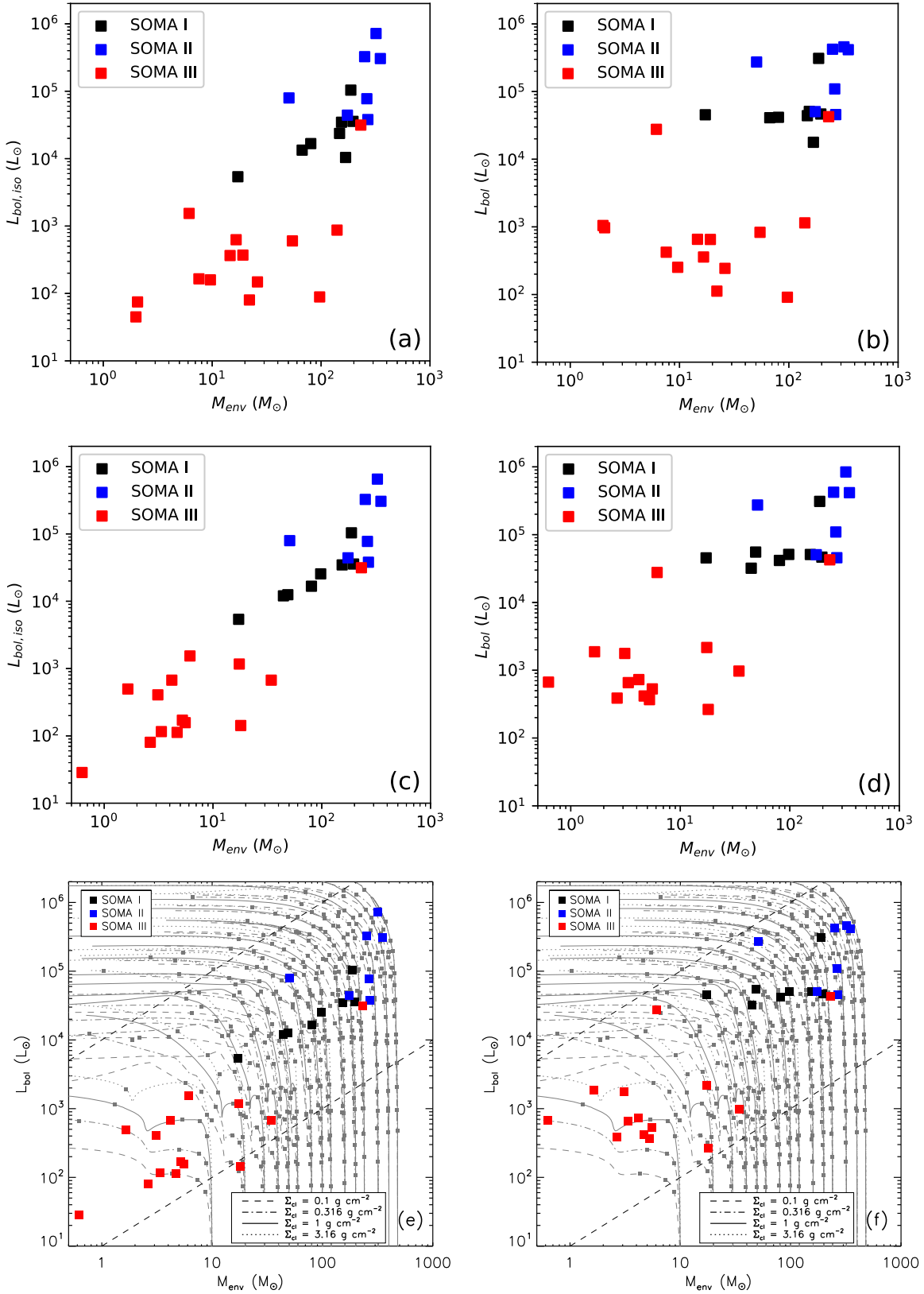


Figure 13. Panel (a): Average (geometric mean) isotropic bolometric luminosity vs. envelope mass returned by the best five (see text) ZT models for each SOMA source from Papers I, II, and III (this work), as labeled. Panel (b): Same as panel (a), but now with true bolometric luminosities plotted vs. envelope mass. Panel (c): Same as panel (a), but now using the average of the best five or fewer models with $R_c \lesssim 2R_{\text{ap}}$ and $\chi^2 < \chi^2_{\text{min}} + 5$. Panel (d): Same as panel (c), but now with true bolometric luminosities plotted vs. envelope mass. Panel (e): Same as panel (c), but now also showing the ZT18 protostar models (gray squares), which are a collection of different evolutionary tracks (gray lines) for different initial core masses and clump mass surface densities (see legend). The two dashed black lines indicate $L_{\text{bol}}/M_{\text{env}} = 10$ and $10^4 L_{\odot}/M_{\odot}$, respectively. Panel (f): Same as panel (e), but now with true bolometric luminosities plotted vs. envelope mass.

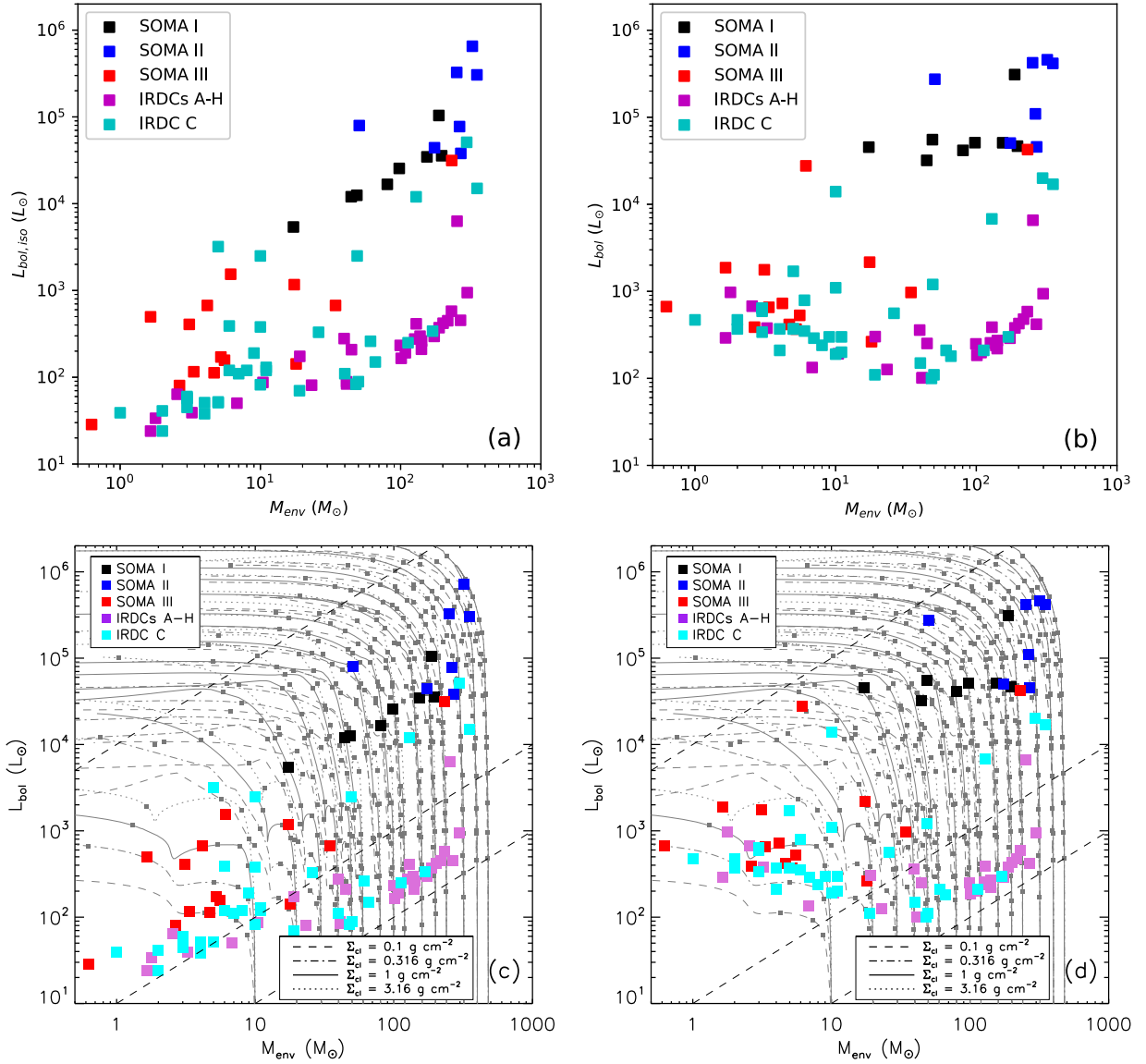


Figure 14. Protostellar evolutionary stages probed by the SOMA sample and IRDC protostar samples: IRDC A-H (Liu et al. 2018 Liu et al. 2020, in preparation), and IRDC C (Moser et al. 2020). The format of the figures is otherwise the same as Figures 13 panels (c)–(f), but with the average (geometric mean) results of the valid models of IRDC sources added. The three dashed black lines in panels c and d indicate $L_{\text{bol}}/M_{\text{env}} = 1, 10$ and $10^4 L_{\odot}/M_{\odot}$.

including within relatively massive core envelopes, so that the sampled values of $L_{\text{bol}}/M_{\text{env}}$ now extend down to $\sim 1 L_{\odot}/M_{\odot}$.

Various biases in the input catalog for the SOMA survey likely account for the lack of sources at the final evolutionary stages of high L_{bol} and low M_{env} . For example, these sources will have relatively weak MIR to FIR emission, which was used as a consideration to target SOMA protostars. Such sources may also be embedded within ultracompact H II regions, which we have tended to avoid for an analysis so far, even if they are within our fields of view: here the challenge is to isolate emission from any remaining protostellar core from the thermal emission from hot dust in the large-scale H II region. Finally, this later phase of evolution may be relatively short, so objects here may be intrinsically rare. Future studies will attempt to identify such sources.

Finally, we note that a future goal is to extend complete surveys of high- and IM protostars across their full range of evolutionary stages and across larger regions so that the

samples can be used for demographic analyses that will inform about topics such as the duration of formation timescales. Previous work in this area, e.g., Davies et al. (2011), which covered large regions of the Galactic plane, focused only on high-mass protostars and have been relatively restricted in their coverage of earlier evolutionary stages.

5.2. The SED Shapes

In Figure 15 we show the bolometric luminosity SEDs of the 14 protostars of this paper, together with the sample of 15 generally higher luminosity sources from Papers I and II. Here the νF_{ν} SEDs have been scaled by $4\pi d^2$ so that the height of the curves gives an indication of the luminosity of the sources assuming isotropic emission. The ordering of the vertical height of these distributions is largely consistent with the rank ordering of the predicted isotropic luminosity of the protostars from the best-fit ZT models (the legend in Figure 15 lists the

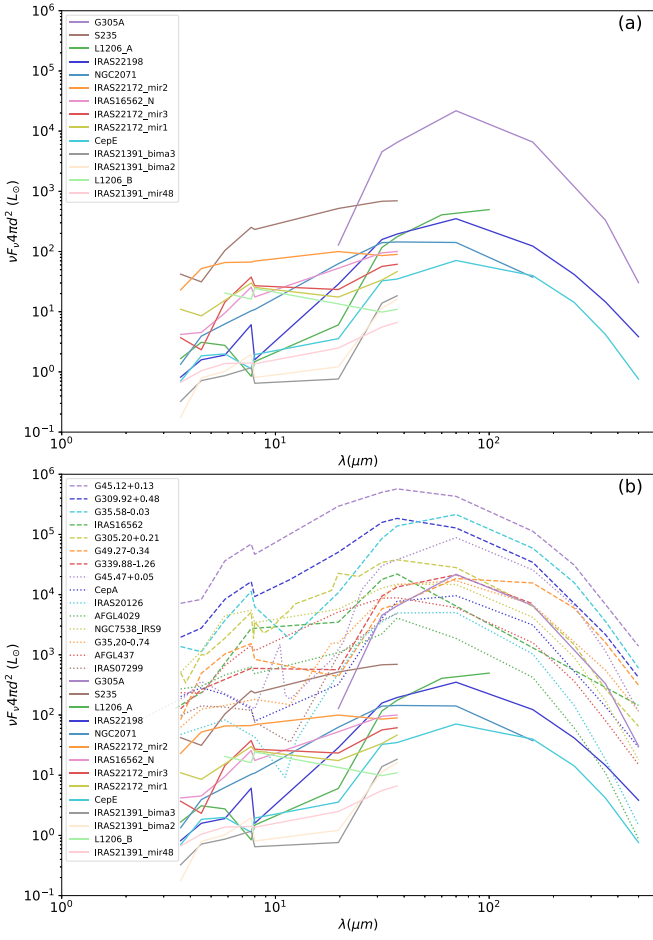


Figure 15. (a) *Top panel:* Bolometric luminosity weighted SEDs of the 14 SOMA protostars analyzed in this paper. The ordering of the legend is from high to low ZT best-fit model isotropic luminosity (top to bottom). (b) *Bottom panel:* Same as panel (a), but now with the addition of dashed lines that denote the sample of 15 sources from Papers I and II.

sources in order of decreasing ZT best-fit model isotropic luminosity).

We define a 19–37 μm spectral index via

$$\alpha_{19-37} = \frac{\nu_{37\mu\text{m}} F_{\nu,37\mu\text{m}} - \nu_{19\mu\text{m}} F_{\nu,19\mu\text{m}}}{\lambda_{37\mu\text{m}} - \lambda_{19\mu\text{m}}}. \quad (1)$$

In general, we expect that this index may vary systematically with protostellar source properties. Figure 16 shows the dependence of α_{19-37} of the SEDs on luminosity, inclination of viewing angle, outflow cavity opening angle, ratio of inclination of viewing angle to outflow cavity opening angle, Σ_{cl} , and m_*/M_c . In all these panels, the results have been averaged over those of the best few or fewer models with core radii smaller than twice the aperture radius and $\chi^2 < \chi^2_{\text{min}} + 5$ (except for G45.12+0.13, see above). We see that the outflow cavity opening angle has a strong effect on the 19–37 μm index, following the expectation that a relatively greater flux of shorter wavelength photons is able to escape from the protostellar core if the outflow cavity opening angle is larger. Also a viewing angle inclination that is relatively small compared to the outflow cavity opening angle will result in a flatter shorter wavelength SED, as also discussed in Paper II.

In Figure 16 we also plot the ZT18 models as gray squares beneath the observations to illustrate the model coverage. Note that the range shown here serves to best show the observations and does not represent the full parameter space of the ZT18 models. We note that while the observed correlations are in general built in the ZT models, the results of Figure 16 show how tight (or loose) the correlations are in practice of the observed SED spectral index in the SOFIA–FORCAST bands with best average protostellar parameters derived from fitting the entire available MIR to FIR SED. This information gives an idea of how much information can be derived from only an observed value of α_{19-37} .

Finally, and along the same lines, another important feature that is revealed by α_{19-37} is the protostellar evolutionary stage, as measured by m_*/M_c (Figure 16(f)). Again, this general trend is expected in the context of the ZT models because the outflow cavity systematically opens up during the course of the evolution and the envelope mass is depleted, resulting in lower overall extinction. There is also generally lower levels of extinction in protostellar cores in lower Σ_{cl} environments, but little correlation is seen here between α_{19-37} and Σ_{cl} (Figure 16(e)), indicating that other factors have a stronger effect.

5.3. Dependence of Massive Star Formation on Environment

Figure 17 shows the distribution of values of M_c (i.e., initial core mass), Σ_{cl} and m_* of the 29 sources of the SOMA sample to date. With no constraint on the model core size, there appears to be an absence of protostars with low M_c in high Σ_{cl} environments. However, this feature is not seen after applying the core size constraint, which we regard as the best method. Thus, the SOMA sample appears to contain protostars that have a range of initial core masses that can be present in the full range of protocluster clump mass surface density environments. However, note that these properties of M_c and Σ_{cl} are not measured directly, but are inferred from the SED fitting.

We next examine if the current protostellar properties depend on protocluster clump environment mass surface density. Figure 18 shows m_* versus Σ_{cl} . Figure 18 panel (a), similar to the results shown in Figure 17 panel (a), appears to show a lack of lower mass sources in high- Σ_{cl} environments. However, this changes when the core size versus SED aperture constraint is applied (Figure 18 panel (b)), so we do not consider this to be a real effect. From the data shown in Figure 18 panel (b), one potential trend that we note is a lack of highest mass ($m_* \gtrsim 25 M_\odot$) protostars in lower mass surface density environments ($\Sigma_{\text{cl}} \lesssim 1 \text{ g cm}^{-2}$). All of the five protostars with $m_* > 25 M_\odot$ (G45.12+0.13, G309.92+0.48, G35.58-0.03, G305.20+0.21, G309.92+0.48, and G35.58-0.03) are inferred to be in $\Sigma_{\text{cl}} > 1 \text{ g cm}^{-2}$ environments. In Figure 18 panel (c), we see that this trend is not a direct result of ZT model parameter space sampling, with the density of models in the grid shown by the blue shading. High m_* protostars forming from cores in low Σ_{cl} environments are present among the ZT models. We note that these models include protostellar outflow feedback, which sets star formation efficiencies close to 50%, but do not include radiative feedback, which would reduce the efficiency (see below).

We further examine how low Σ_{cl} models fail for high m_* sources in Figure 19. Here we exclude G45.12+0.13 because none of the models fit particularly well for this source (see Paper II). We can see that the median χ^2 and the smallest χ^2

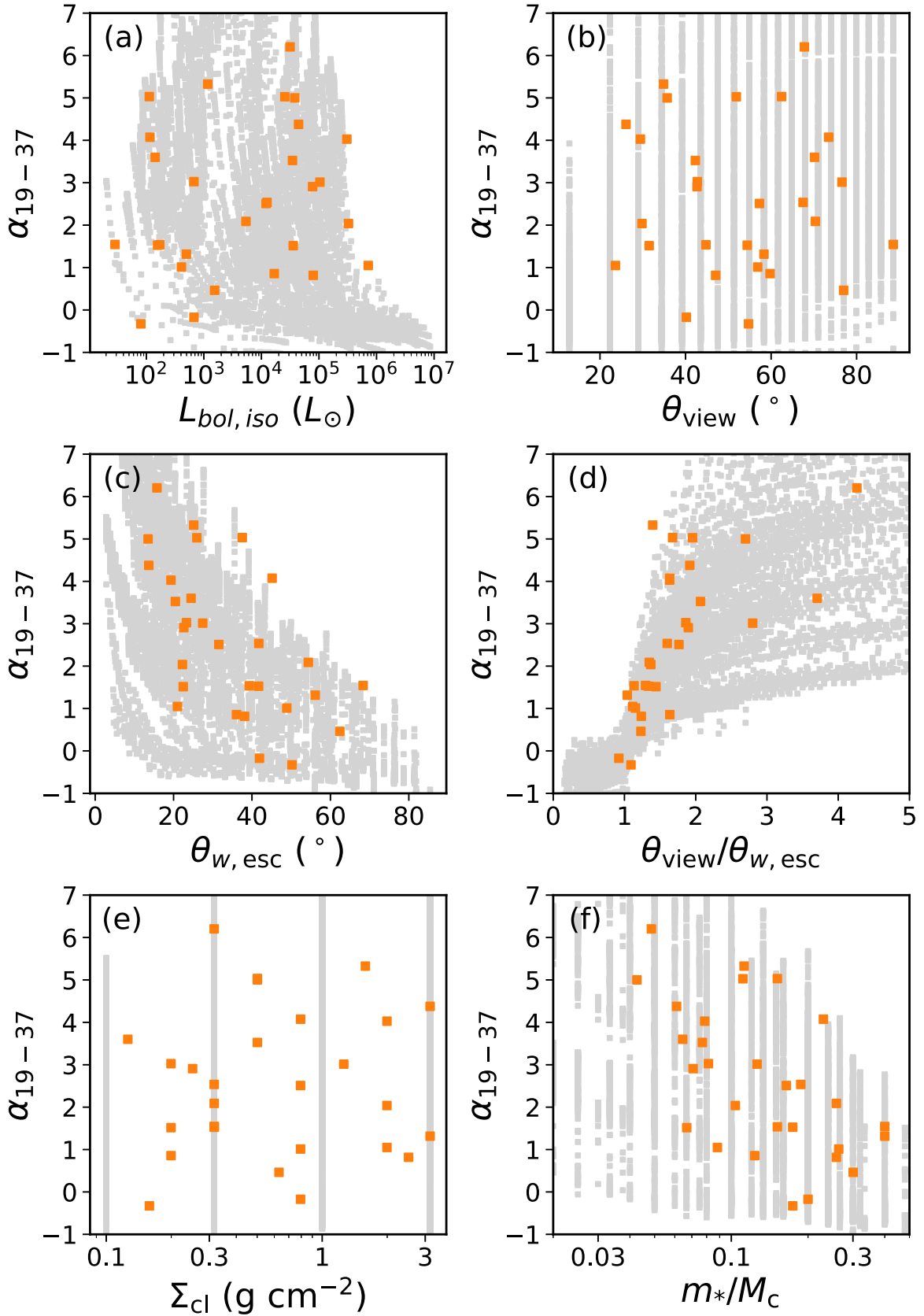


Figure 16. Spectral index, α_{19-37} between 19 μm and 37 μm (see text) vs. the geometric mean isotropic luminosity $L_{bol,iso}$ (a: top left), the arithmetic mean inclination of viewing angle θ_{view} (b: top right), the arithmetic mean opening angle $\theta_{w,esc}$ (c: middle left), the arithmetic mean $\theta_{view}/\theta_{w,esc}$ (d: middle right), the geometric mean clump surface density Σ_{cl} (e: bottom left), and the geometric mean m_*/M_c (f: bottom right) returned by the best five or fewer models with $R_c \lesssim 2R_{ap}$ and $\chi^2 < \chi^2_{min} + 5$. The gray squares represent the ZT18 protostar models. Note that the spectral index of the models is calculated without foreground extinction and thus could be different from observations.

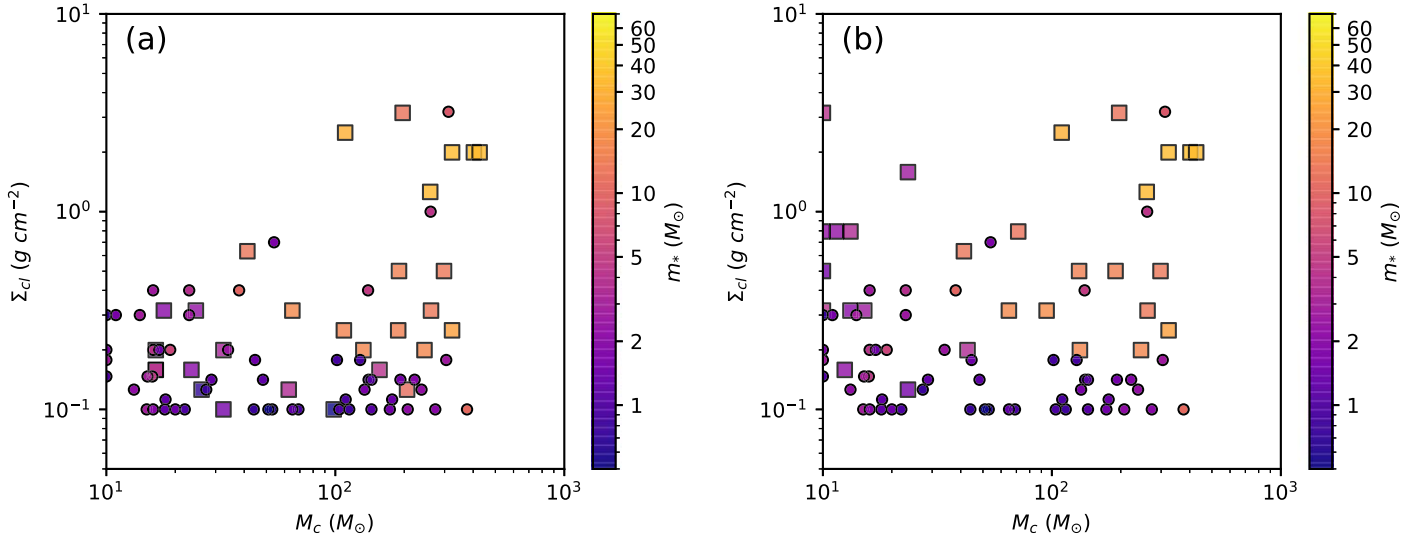


Figure 17. *a) Left:* average clump mass surface density, Σ_{cl} , vs. average initial core mass, M_c , of the SOMA sources (squares) and IRDC sources (circles, Liu et al. 2018 Moser et al. 2020; Liu et al. 2020, in preparation), based on ZT model fits: the average is made for the best five selected models. Panel *b) right:* same as panel (a), but with the average made for the best five or fewer models with $R_c \lesssim 2R_{\text{ap}}$ and $\chi^2 < \chi^2_{\text{min}} + 5$.

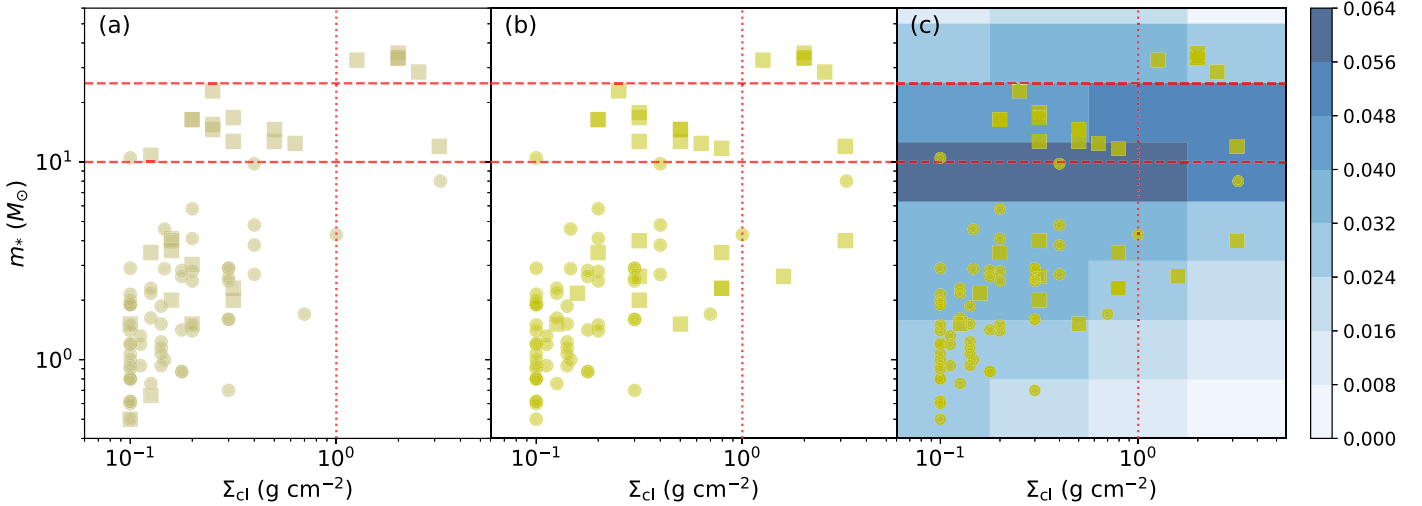


Figure 18. Panel *(a) left:* average protostellar mass, m_* , vs. average clump mass surface density, Σ_{cl} , of SOMA sources (squares) and IRDC sources (circles, Liu et al. 2018 Moser et al. 2020; Liu et al. 2020, in preparation), based on ZT model fits: the average is made for the best five selected models. The dotted and dashed red lines indicate fiducial threshold values of m_* (10 and 25 M_\odot) and Σ_{cl} (1 g cm^{-2} , see text). Panel *(b) middle:* same as panel (a), but with the average made for best five or fewer models with $R_c \lesssim 2R_{\text{ap}}$ and $\chi^2 < \chi^2_{\text{min}} + 5$. Panel *(c) right:* same as panel (b), but now also showing the distribution of models in the ZT model grid (shading indicates the density of models).

achieved generally decrease with Σ_{cl} . Compared with high Σ_{cl} models, low Σ_{cl} models usually have higher fluxes at shorter wavelengths, i.e., $\lesssim 8\mu\text{m}$. These can be higher than the observational upper limits, which leads to a significant penalty in the fitting. Low Σ_{cl} models also tend to have lower fluxes at longer wavelength, i.e., $\gtrsim 20\mu\text{m}$. Therefore they deviate from the shape of the observed SEDs. We also tried to adjust A_V or L_{bol} of the low Σ_{cl} models manually (not shown here), but such changes do not lead to significant improvement in the model SED shape in comparison to the data.

Thus, we conclude that there is tentative evidence from the SOMA sample analyzed so far that the most massive protostars require their cores to be in $\Sigma_{\text{cl}} > 1 \text{ g cm}^{-2}$ environments, but more extended further testing with a larger number of sources is clearly needed to confirm this.

Krumholz & McKee (2008) proposed that a minimum mass surface density of 1 g cm^{-2} is needed for massive star formation, based on protostellar heating suppression of fragmentation of massive cores by a population of surrounding lower mass protostars (these protostars have higher accretion rates and thus luminosities in higher Σ_{cl} environments). While our result appears to confirm this prediction, we caution that the Krumholz & McKee model also predicts that $10 M_\odot$ protostars would not be able to form in $\Sigma_{\text{cl}} \lesssim 0.3 \text{ g cm}^{-2}$ environments, which is inconsistent with the SOMA data. As an alternative, magnetic suppression of fragmentation to allow the existence of massive early-stage cores has been discussed by, e.g., Butler & Tan (2012), with evidence of strong, $\sim 1 \text{ mG}$ B -fields inferred for several cores in the IRDC 18310-4 region (Beuther et al. 2018).

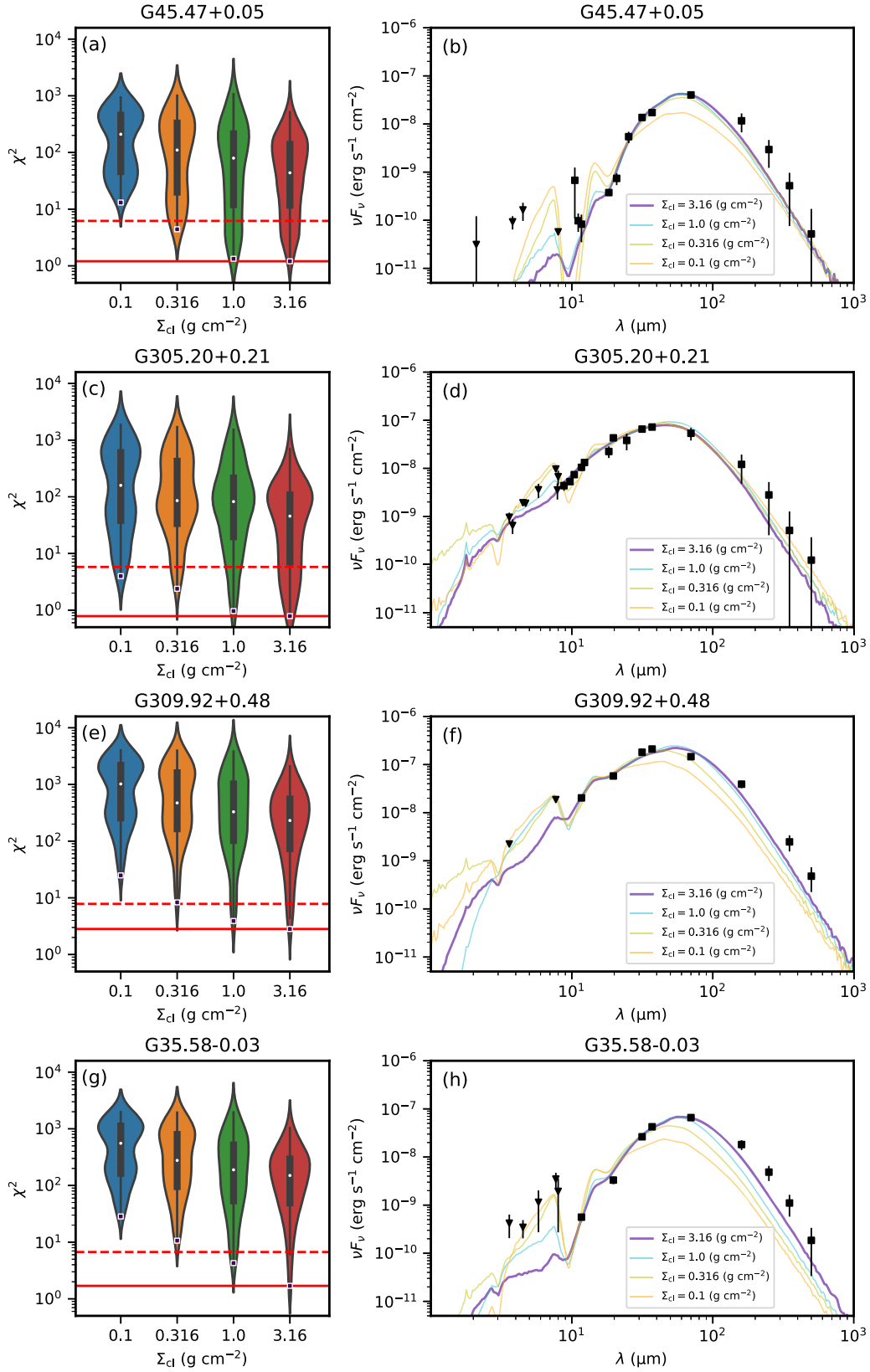


Figure 19. *Left column:* Violin plots of χ^2 vs. Σ_{cl} of all the models for several of the most massive protostars: G45.47+0.05, G305.20+0.21, G309.92+0.48, and G35.58-0.03. For the violin of each Σ_{cl} , the white dot in the center of the violin denotes the median χ^2 . The black lines stretched from the bar denote the lower/upper adjacent values—defined as the furthest observation within 1.5 IQR of the lower/upper end of the bar. The width of the violin represents the probability density of the data value smoothed by a kernel density estimator. The squares at the bottom of each violin denote the smallest χ^2 achieved by that Σ_{cl} . The solid red line denotes χ^2_{min} for the source. The dashed red line denotes $\chi^2_{\text{min}} + 5$. *Right column:* SEDs of the best model of each Σ_{cl} for each source (the thickest line is the overall best model). The black triangles and squares with error bars denote the observations.

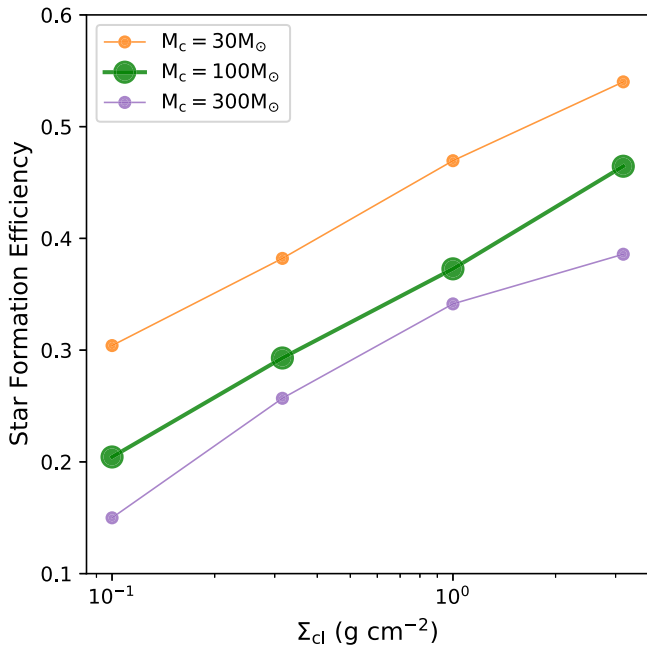


Figure 20. Star formation efficiency as a function of clump mass surface density, Σ_{cl} , from model calculations of Tanaka et al. (2017). Models for initial core masses of $M_c = 30$, 100 and $300 M_\odot$ are shown, as labeled.

The assembly of the highest mass prestellar cores, e.g., via a bottom-up process of merging smaller prestellar cores or by general accumulation of clump gas, is expected to be more efficient in denser regions, and this could provide an explanation, in the context of core accretion models (McKee & Tan 2003), of the trends seen in Figure 18.

When cores initiate star formation, their accretion rates are also expected to be higher in high surface density environments, and this is expected to allow higher protostellar masses to be formed. Tanaka et al. (2017) assessed the expected star formation efficiency from cores due to both radiative and mechanical (i.e., outflow) feedback as a function of Σ_{cl} and found that it can decrease by more than a factor of two for a given initial core as Σ_{cl} decreases from 3.2 to 0.1 g cm^{-2} (see Figure 20). The decrease is greatest for more massive cores because when they start forming stars with $m_* \gtrsim 20 M_\odot$, radiative feedback becomes powerful enough to truncate further accretion. For example, the $\Sigma_{\text{cl}} = 0.1 \text{ g cm}^{-2}$ models shown in Figure 20 reach $m_* \simeq 10 M_\odot$ starting from a $30 M_\odot$ core, $m_* \simeq 20 M_\odot$ starting from a $100 M_\odot$ core, and $m_* \simeq 45 M_\odot$ starting from a $300 M_\odot$ core. However, the equivalent $\Sigma_{\text{cl}} = 1 \text{ g cm}^{-2}$ models reach values of $m_* \simeq 15$, 40, and $100 M_\odot$, respectively. Thus, in the context of these models, it is much more difficult to produce, e.g., $30 M_\odot$ protostars in low- Σ_{cl} environments due to feedback effects, especially because the prestellar core mass function is expected to decline rapidly with increasing mass.

For competitive accretion models (Bonnell et al. 2001; Wang et al. 2010), higher mass surface density environments are also expected to lead to higher accretion rates and thus will probably also allow the formation of higher mass stars. However, the equivalent calculations for the effect of feedback have not yet been carried out for these models.

From an observational analysis of three clouds that are forming massive stars compared to several others that are not,

Kauffmann et al. (2010) proposed a criterion for massive star formation equivalent to $\Sigma_{\text{cl}} \geq 0.054 (M_{\text{cl}}/1000 M_\odot)^{-1/2} \text{ g cm}^{-2}$, which is relatively low compared to the thresholds discussed above. Also, this value is lower than the minimum of the range probed in the ZT18 protostellar model grid of $\Sigma_{\text{cl}} = 0.1 \text{ g cm}^{-2}$. Recently, Retes-Romero et al. (2020) studied 128 IRDCs to investigate if the Kauffmann et al. criterion predicts which of these IRDCs contains massive stars. They found that of the IRDCs satisfying this criterion, only one-third currently contain massive YSOs. This may indicate that a higher, more localized value of Σ_{cl} is needed to form a massive star. For further progress on the general question of massive star formation thresholds, more direct measures of Σ_{cl} , e.g., from dust continuum emission (in contrast to our indirect methods based on model fitting), on scales immediately surrounding the massive protostars and comparison to protostellar properties, e.g., as derived from SED fitting in the SOMA sample, are needed. However, such an analysis, which we defer to a future study, will inevitably be sensitive to how and where the protostellar core boundary is defined, and such sensitivity will also need to be explored.

In summary, our results tentatively indicate that forming the most massive $\gtrsim 25 M_\odot$ protostars requires $\gtrsim 1 \text{ g cm}^{-2}$ proto-cluster clump environments, although this is based on a relatively small number (5) of protostellar sources that are in this mass range. We have a larger number (about 10) of protostars with $10 M_\odot \lesssim m_* \lesssim 25 M_\odot$ that are best fit by models with $\Sigma_{\text{cl}} \lesssim 0.3 \text{ g cm}^{-2}$, so that no particular mass surface density threshold appears to be required in this range to form $10 M_\odot$ protostars. These environmental dependencies on massive star formation need confirmation with larger numbers of sources. Such trends are consistent with several different theoretical expectations from core accretion models, including that due to decreasing star formation efficiency due to self-feedback for massive protostars in lower mass surface density environments.

Finally, we investigate the dependence of $L_{\text{bol,iso}}$ and L_{bol} on Σ_{cl} in Figure 21. When model core size to aperture constraints are applied (panels b and e), no strong correlation is present in the overall distribution. The highest luminosity sources, which have the highest protostellar masses, are preferentially found in high-mass surface density environments. This is not due to the sources having higher current accretion rates because for these high m_* sources, the accretion luminosity is only a relatively minor component of the total luminosity. Thus this trend is simply a reflection of the trends seen in the mass distribution of the sources.

6. Conclusions

We have presented the results of MIR and FIR observations carried out toward 14 protostars in the SOMA survey, most of which are IM protostars. Following our standard methods developed in Papers I and II, we have built their SEDs with additional archival Spitzer, Herschel, and IRAS data and fit them with Zhang & Tan (2018) RT models of massive star formation via the turbulent core accretion paradigm. We have also supplemented the sample with protostars identified in Infrared Dark Clouds (IRDCs) that are expected to be at very early stages in their evolution. By these methods we have extended the range of masses, luminosities, and evolutionary stages of protostellar sources that have been analyzed in a

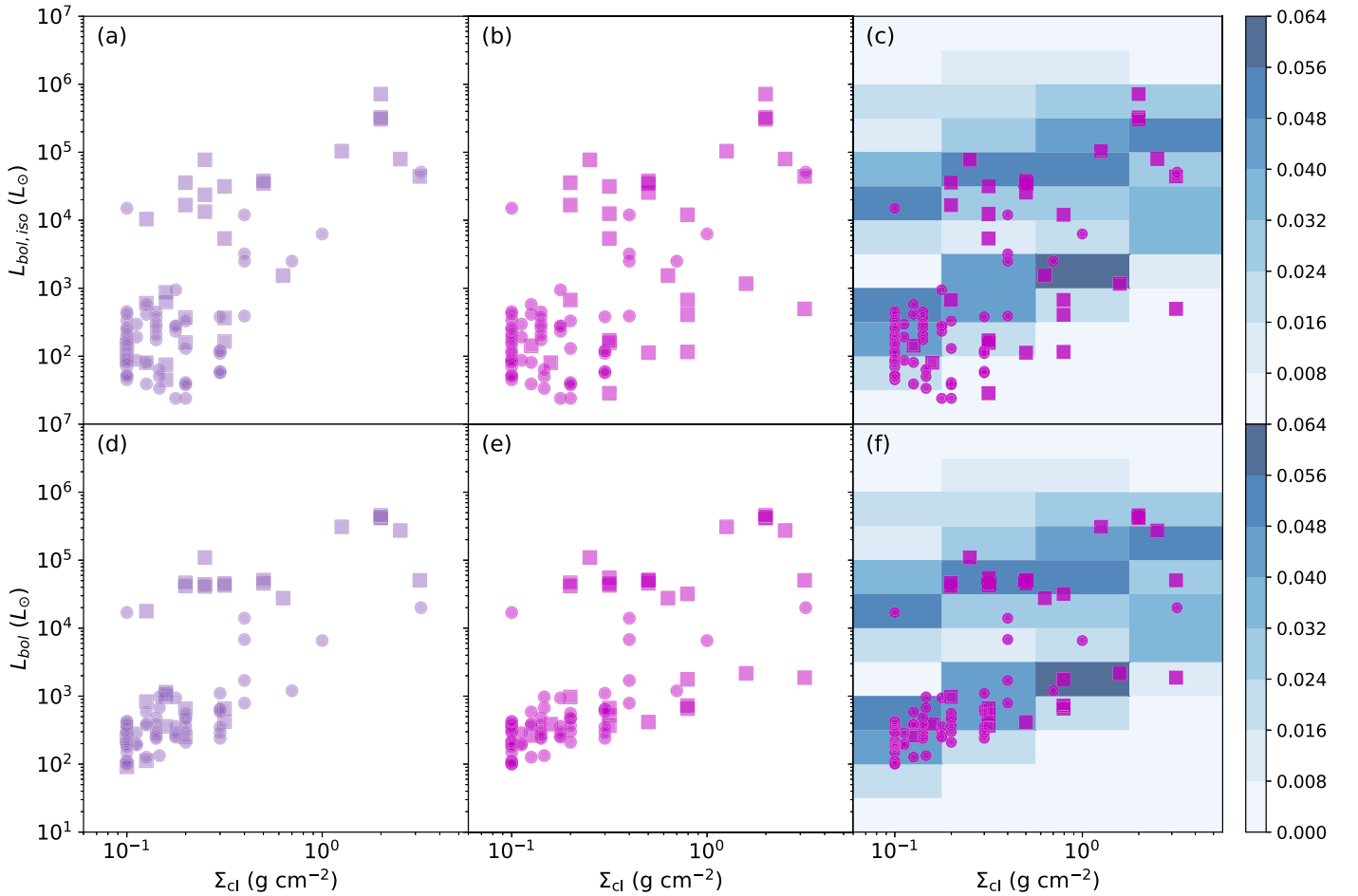


Figure 21. Panel (a) *top left*: average protostellar isotropic bolometric luminosity, $L_{\text{bol,iso}}$, vs. average clump mass surface density, Σ_{cl} , of SOMA sources (squares) and IRDC sources (circles, Liu et al. 2018 Moser et al. 2020; Liu et al. 2020, in preparation), based on ZT model fits: the average is made for the best five selected models. Panel (b) *top middle*: same as panel (a), but with the average made for best five or fewer models with $R_c \lesssim 2R_{\text{ap}}$ and $\chi^2 < \chi^2_{\text{min}} + 5$. Panel (c) *top right*: same as panel (b), but now also showing the distribution of models in the ZT model grid (shading indicates the density of models). Panel (d) *bottom left*: same as panel (a), but now for intrinsic bolometric luminosity, L_{bol} . Panel (e) *bottom middle*: same as panel (b), but now for intrinsic bolometric luminosity, L_{bol} . Panel (f) *bottom right*: same as panel (c), but now for the intrinsic bolometric luminosity, L_{bol} .

uniform manner to test the core accretion theory. Our main results and conclusions are listed below.

1. The IM protostars presented in this paper appear relatively compact at 20–40 μm , compared to the high-mass protostars in Papers I and II, whose 20–40 μm images more clearly show extension along their outflow axes. The protostars presented here are forming in a variety of protocluster environments, as revealed by NIR images. Higher resolution submm images often reveal secondary dense gas cores within 0.1 pc (in projection).
2. The SEDs of the 14 protostars of this paper are generally fit quite well by the ZT models, but there are significant degeneracies among acceptable models. These degeneracies in key model parameters, i.e., initial core mass, M_c , clump mass surface density, Σ_{cl} , and current protostellar mass, m_* , are typically larger than for the higher mass protostars, but this is often a reflection of the more limited wavelength coverage of the IM sources, which are often away from the Galactic plane and thus lack, e.g., longer wavelength Herschel data. For the sources analyzed here, we find that well-fitting models can often have $R_c > R_{\text{ap}}$. Thus we have applied a further


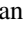




constraint that model core radii should not exceed the aperture radius used to define the SED by more than a factor of two.

3. The SOMA sources analyzed in this paper and Papers I and II span a range of bolometric luminosities of $\sim 10^2 L_{\odot}$ to $\sim 10^6 L_{\odot}$. The isotropic luminosity can be quite different from the intrinsic luminosity, indicating a significant flashlight effect in the sources.
4. The presented SOMA sample spans a range of light-to-mass ratios of $L_{\text{bol}}/M_{\text{env}}$ from $\sim 10 L_{\odot}/M_{\odot}$ to $\sim 10^4 L_{\odot}/M_{\odot}$. The addition of IRDC protostars extends this range down to $\sim 1 L_{\odot}/M_{\odot}$, which is expected to be near the very earliest phases of the star formation process. Relatively late stages of evolution are currently missing from the sample.
5. The SED shape, as measured by the spectral index from 19 to 37 microns, shows trends with outflow opening angle, ratio of viewing angle to outflow opening angle, and evolutionary stage, i.e., m_*/M_c . However, such trends are features that are inherent in the ZT18 models, and independent confirmation, e.g., from high-resolution continuum and line studies of outflows and outflow cavities, is needed.

6. Protostars from low masses up to $\sim 25 M_{\odot}$ are inferred to be forming at all the clump mass surface densities probed by the models, i.e., from 0.1 to 3 g cm^{-2} . However, to form protostars with $> 25 M_{\odot}$ appears to require $\Sigma_{\text{cl}} \gtrsim 1 \text{ g cm}^{-2}$ clump environments. Larger numbers of sources in this mass range are needed to confirm this result. While this finding is consistent with several possible theoretical expectations, we favor one based on internal feedback in the protostellar core, which becomes less effective for the denser cores that are associated with higher Σ_{cl} environments (Tanaka et al. 2017).

We thank the anonymous referee for helping us to improve the paper. M.L. acknowledges funding from the Jefferson Scholars Foundation. M.L. and J.C.T. acknowledge funding from NASA/USRA/SOFIA. J.C.T. acknowledges support from NSF grant AST1411527, VR grant 2017-04522 and ERC project 788829—MSTAR. Y.Z. acknowledges support from JSPS KAKENHI grant JP19K14774. K.E.I.T. acknowledges support from NAOJ ALMA Scientific Research grant No. 2017-05A, and JSPS KAKENHI grant Nos. JP19H05080, JP19K14760. Y.L.Y. acknowledges support from a Virginia Initiative on Cosmic Origins (VICO) postdoctoral fellowship. R.F. acknowledges support from a Chalmers Initiative on Cosmic Origins (CICO) postdoctoral fellowship.

ORCID iDs

Mengyao Liu  <https://orcid.org/0000-0001-6159-2394>
Jonathan C. Tan  <https://orcid.org/0000-0002-3389-9142>
Yichen Zhang  <https://orcid.org/0000-0001-7511-0034>
Jan E. Staff  <https://orcid.org/0000-0001-9040-8525>
Kei E. I. Tanaka  <https://orcid.org/0000-0002-6907-0926>
Viviana Rosero  <https://orcid.org/0000-0001-8596-1756>
Yao-Lun Yang  <https://orcid.org/0000-0001-8227-2816>
Rubén Fedriani  <https://orcid.org/0000-0003-4040-4934>

References

- Andre, P., Ward-Thompson, D., & Barsony, M. 1993, *ApJ*, 406, 122
Anthony-Twarog, B. J. 1982, *AJ*, 87, 1213
Ayala, S., Noriega-Crespo, A., Garnavich, P. M., et al. 2000, *AJ*, 120, 909
Bally, J. 1982, *ApJ*, 261, 558
Beltrán, M. T. 2015, *Ap&SS*, 355, 283
Beltrán, M. T., Estalella, R., Girart, J. M., et al. 2008, *A&A*, 481, 93
Beltrán, M. T., Girart, J. M., Estalella, R., et al. 2002, *ApJ*, 573, 246
Beltrán, M. T., Girart, J. M., & Estalella, R. 2006, *A&A*, 457, 865
Beltrán, M. T., Massi, F., López, R., et al. 2009, *A&A*, 504, 97
Beuther, H., Soler, J. D., Vlemmings, W., et al. 2018, *A&A*, 614, A64
Boley, P. A., Sobolev, A. M., Krushinsky, V. V., et al. 2009, *MNRAS*, 399, 778
Bonnell, I. A., Bate, M. R., Clarke, C. J., & Pringle, J. E. 2001, *MNRAS*, 323, 785
Bontemps, S., Andre, P., Terebey, S., et al. 1996, *A&A*, 311, 858
Burns, R. A., Imai, H., Handa, T., et al. 2015, *MNRAS*, 453, 3163
Butler, M. J., & Tan, J. C. 2009, *ApJ*, 696, 484
Butler, M. J., & Tan, J. C. 2012, *ApJ*, 754, 5
Cabrit, S., & Bertout, C. 1992, *A&A*, 261, 274
Cesaroni, R., Felli, M., & Walmsley, C. M. 1999, *A&AS*, 136, 333
Choudhury, R., Mookerjee, B., & Bhatt, H. C. 2010, *ApJ*, 717, 1067
Codella, C., Bachiller, R., Nisini, B., et al. 2001, *A&A*, 376, 271
Crimier, N., Ceccarelli, C., Alonso-Albi, T., et al. 2010, *A&A*, 516, A102
Davies, B., Hoare, M. G., Lumsden, S. L., et al. 2011, *MNRAS*, 416, 972
De Buizer, J. M., Liu, M., Tan, J. C., et al. 2017, *ApJ*, 843, 33
Dewangan, L. K., & Anandarao, B. G. 2011, *MNRAS*, 414, 1526
Dewangan, L. K., & Ojha, D. K. 2017, *ApJ*, 849, 65
Dewangan, L. K., Ojha, D. K., Luna, A., et al. 2016, *ApJ*, 819, 66
Eisloffel, J. 2000, *A&A*, 354, 236
Evans, N. J., & Blair, G. N. 1981, *ApJ*, 246, 394
Fazio, G. G., Hora, J. L., Allen, L. E., et al. 2004, *ApJS*, 154, 10
Fedriani, R., Caratti o Garatti, A., Purser, S. J. D., et al. 2019, *NatCo*, 10, 3630
Felli, M., Massi, F., Navarrini, A., et al. 2004, *A&A*, 420, 553
Felli, M., Massi, F., Robberto, M., et al. 2006, *A&A*, 453, 911
Felli, M., Palagi, F., & Tofani, G. 1992, *A&A*, 255, 293
Felli, M., Testi, L., Valdetaro, R., et al. 1997, *A&A*, 320, 594
Fontani, F., Cesaroni, R., Testi, L., et al. 2004, *A&A*, 424, 179
Fuente, A., Castro-Carrizo, A., Alonso-Albi, T., et al. 2009, *A&A*, 507, 1475
Fuente, A., Rizzo, J. R., Caselli, P., et al. 2005, *A&A*, 433, 535
Fujisawa, K., Takase, G., Kimura, S., et al. 2014, *PASJ*, 66, 78
Griffin, M. J., Abergel, A., Abreu, A., et al. 2010, *A&A*, 518, L3
Gueth, F., Schilke, P., & McCaughrean, M. J. 2001, *A&A*, 375, 1018
Gusdorf, A., Anderl, S., Lefloch, B., et al. 2017, *A&A*, 602, A8
Hatchell, J., Fuller, G. A., & Richer, J. S. 2007, *A&A*, 472, 187
Herter, T. L., Vacca, W. D., Adams, J. D., et al. 2013, *PASP*, 125, 1393
Hirota, T., Ando, K., Bushimata, T., et al. 2008, *PASJ*, 60, 961
Israel, F. P., & Felli, M. 1978, *A&A*, 63, 325
Kauffmann, J., Pillai, T., Shetty, R., et al. 2010, *ApJ*, 716, 433
Klein, R., Posselt, B., Schreyer, K., et al. 2005, *ApJS*, 161, 361
Krassner, J., Pipher, J. L., Sharpless, S., et al. 1982, *A&A*, 109, 223
Krumholz, M. R., & McKee, C. F. 2008, *Natur*, 451, 1082
Kurtz, S., Hofner, P., & Álvarez, C. V. 2004, *ApJS*, 155, 149
Lawrence, A., Warren, S. J., Almaini, O., et al. 2007, *MNRAS*, 379, 1599
Lefloch, B., Cernicharo, J., Pacheco, S., et al. 2011, *A&A*, 527, L3
Lefloch, B., Eisloffel, J., & Lazareff, B. 1996, *A&A*, 313, L17
Lefloch, B., Gusdorf, A., Codella, C., et al. 2015, *A&A*, 581, A4
Liu, M., Tan, J. C., Cheng, Y., et al. 2018, *ApJ*, 862, 105
Liu, M., Tan, J. C., De Buizer, J. M., et al. 2019, *ApJ*, 874, 16
Matthews, H. I. 1979, *A&A*, 75, 345
McCutcheon, W. H., Dewdney, P. E., Purton, C. R., et al. 1991, *AJ*, 101, 1435
McKee, C. F., & Tan, J. C. 2003, *ApJ*, 585, 850
Molinari, S., Brand, J., Cesaroni, R., et al. 1996, *A&A*, 308, 573
Molinari, S., Pezzuto, S., Cesaroni, R., et al. 2008, *A&A*, 481, 345
Molinari, S., Schisano, E., Elia, D., et al. 2016, *A&A*, 591, A149
Molinari, S., Testi, L., Rodríguez, L. F., et al. 2002, *ApJ*, 570, 758
Moro-Martín, A., Noriega-Crespo, A., Molinari, S., et al. 2001, *ApJ*, 555, 146
Moser, E., Liu, M., Tan, J. C., et al. 2020, *ApJ*, 897, 136
Neri, R., Fuente, A., Ceccarelli, C., et al. 2007, *A&A*, 468, L33
Neugebauer, G., Habing, H. J., van Duinen, R., et al. 1984, *ApJL*, 278, L1
Nisini, B., Massi, F., Vitali, F., et al. 2001, *A&A*, 376, 553
Norris, R. P., Whiteoak, J. B., Caswell, J. L., et al. 1993, *ApJ*, 412, 222
Ospina-Zamudio, J., Lefloch, B., Ceccarelli, C., et al. 2018, *A&A*, 618, A145
Palau, A., Fuente, A., Girart, J. M., et al. 2013, *ApJ*, 762, 120
Palau, A., Sánchez-Monge, Á., Busquet, G., et al. 2010, *A&A*, 510, A5
Palla, F., Brand, J., Cesaroni, R., Comoretto, G., & Felli, M. 1991, *A&A*, 246, 249
Palla, F., Cesaroni, R., Brand, J., et al. 1993, *A&A*, 280, 599
Patel, N. A., Greenhill, L. J., Herrnstein, J., et al. 2000, *ApJ*, 538, 268
Ressler, M. E., & Shure, M. 1991, *AJ*, 102, 1398
Retes-Romero, R., Mayya, Y. D., Luna, A., et al. 2020, *ApJ*, 897, 53
Robitaille, T. P., Whitney, B. A., Indebetouw, R., et al. 2006, *ApJS*, 167, 256
Robitaille, T. P., Whitney, B. A., Indebetouw, R., et al. 2007, *ApJS*, 169, 328
Rosero, V., Tanaka, K. E. I., Tan, J. C., et al. 2019, *ApJ*, 873, 20
Rygl, K. L. J., Brunthaler, A., Reid, M. J., et al. 2010, *A&A*, 511, A2
Saito, H., Saito, M., Sunada, K., et al. 2007, *ApJ*, 659, 459
Sánchez-Monge, Á., Palau, A., Estalella, R., et al. 2008, *A&A*, 485, 497
Sánchez-Monge, Á., Palau, A., Estalella, R., et al. 2010, *ApJL*, 721, L107
Saraceno, P., Ceccarelli, C., Clegg, P., et al. 1996, *A&A*, 315, L293
Sargent, A. I. 1977, *ApJ*, 218, 736
Serabyn, E., Guesten, R., & Mundy, L. 1993, *ApJ*, 404, 247
Seth, A. C., Greenhill, L. J., & Holder, B. P. 2002, *ApJ*, 581, 325
Shepherd, D. S., & Watson, A. M. 2002, *ApJ*, 566, 966
Shimoikura, T., Dobashi, K., Matsumoto, T., et al. 2016, *ApJ*, 832, 205
Skrutskie, M. F., Cutri, R. M., Stiening, R., et al. 2006, *AJ*, 131, 1163
Smith, H. A., & Beck, S. C. 1994, *ApJ*, 420, 643
Snell, R. L., & Bally, J. 1986, *ApJ*, 303, 683
Staff, J. E., Tanaka, K. E. I., & Tan, J. C. 2019, *ApJ*, 882, 123
Stojimirović, I., Snell, R. L., & Narayanan, G. 2008, *ApJ*, 679, 557
Sugitani, K., Fukui, Y., Mizuni, A., et al. 1989, *ApJL*, 342, L87
Sugitani, K., Matsuo, H., Nakano, M., et al. 2000, *AJ*, 119, 323
Takahashi, S., Saigo, K., Ho, P. T. P., et al. 2012, *ApJ*, 752, 10
Tanaka, K. E. I., Tan, J. C., & Zhang, Y. 2017, *ApJ*, 835, 32
Tofani, G., Felli, M., Taylor, G. B., et al. 1995, *A&AS*, 112, 299
Torrelles, J. M., Gómez, J. F., Rodríguez, L. F., et al. 1998, *ApJ*, 505, 756
Trinidad, M. A., Rodríguez, T., & Rodríguez, L. F. 2009, *ApJ*, 706, 244

- Urquhart, J. S., König, C., Giannetti, A., et al. 2018, [MNRAS](#), **473**, 1059
- Valdettaro, R., Palla, F., Brand, J., et al. 2005, [A&A](#), **443**, 535
- van Kempen, T. A., Longmore, S. N., Johnstone, D., et al. 2012, [ApJ](#), **751**, 137
- Velusamy, T., Langer, W. D., Kumar, M. S. N., et al. 2011, [ApJ](#), **741**, 60
- Wang, P., Li, Z.-Y., Abel, T., & Nakamura, F. 2010, [ApJ](#), **709**, 27
- Willing, B., Mundy, L., McMullin, J., et al. 1993, [AJ](#), **106**, 250
- Willing, B. A., Mundy, L. G., Blackwell, J. H., et al. 1989, [ApJ](#), **345**, 257
- Wouterloot, J. G. A., & Walmsley, C. M. 1986, [A&A](#), **168**, 237
- Wu, Y., Wei, Y., Zhao, M., et al. 2004, [A&A](#), **426**, 503
- Young, E. T., Herter, T. L., Güsten, R., et al. 2012, [Proc. SPIE](#), **8444**, 844410
- Zapata, L. A., Ho, P. T. P., Rodríguez, L. F., et al. 2007, [A&A](#), **471**, L59
- Zhang, Y., & Tan, J. C. 2018, [ApJ](#), **853**, 18